Doklady Physics, Vol. 46, No. 1, 2001, pp. 1–3. Translated from Doklady Akademii Nauk, Vol. 376, No. 1, 2001, pp. 33–35.

PHYSICS

Harmonic Conjugation of Generation Processes and Noise-Radiation Processes of Cavitation Cavities (Application of the D-SELF Model)

A. G. Ivanov-Rostovtsev, L. G. Kolotilo, and Yu. F. Tarasyuk

Presented by Academician K.Ya. Kondrat'ev April 18, 2000

Received April 28, 2000

FORMULATION OF THE PROBLEM

It is well known that the cavitation processes in turbulent boundary layers near interfaces of the atmosphere–hydrosphere–lithosphere are characterized by effects related to both vibrational hydrodynamic phenomena (generation of cavitation cavities [1, 2]) and wave acoustic phenomena (noise-radiation during cavitation [3, 4]). As a rule, both effects are investigated independently. Since the above processes can be described by the same parameters, it is of interest to establish the interconnection and interdependence between the processes of both types in terms of parameters describing these phenomena. The present study is devoted to solving this problem.

THE METHOD FOR SOLVING THE PROBLEM

As was shown by authors previously, there exists a possibility of conjugation of harmonic parameters (harmonics) qualitatively characterizing different dynamic effects in complex distributed systems (in mechanical continua, in Earth's crust structures, etc.) on the basis of the D-SELF model. This model was put forward for the first time in [5] and further developed in [6]. In a series of papers [7–9], the different aspects of the applications of the D-SELF model were demonstrated. The present study develops this direction of research.

According to the D-SELF model, harmonic effects are characterized by simultaneous excitation of wave processes and vibration processes while transforming the energy delivered from an external source [8].

It is well known [10] that in a continuum with distributed parameters, various forms of periodic motion and processes can be classified as wave and vibration ones. There exists the problem that the processes of both types in the classical formulation are not related to one another. Traditionally, their interconnection is considered in nonlinear approaches. The principal difficulty in the analysis of waves and vibrations is associated with the absence of a unique generalization including the formalism of both the wave approach (d'Alembert interpretation) and vibration approach (Bernoulli interpretation). The D-SELF model makes it possible to consider the interconnection between the wave and vibration motions in mechanical media on the basis of conjugation parameters for wave and vibration processes [8].

Performing an analysis of spectra of the vibration process (vibration generation) and the wave process (noise-radiation by cavitation cavities) taken as examples, we show their interconnection via the conjugation of their parameters. As a condition of conjugation for two arbitrary parameters ζ and ζ^* with respect to parameter ζ_0, we will consider their invariant interconnection as described by the relation $\sqrt{\xi\xi} \equiv \xi_0$.

LOW-FREQUENCY GENERATION OF CAVITIES

The formation (generation), growth, and collapse of cavitation cavities arising in turbulent boundary layers and cocurrent flows are related to periodic pressure pulsations in the turbulent flow [1, 2]. It is shown in [2] that this periodicity is described by the frequency directly proportional to the flow velocity V and inversely proportional to the characteristic size L of a body (or an obstacle) (Fig. 1):

$$f = \frac{\mathrm{Sh}V}{L} = \frac{V}{kL}, \qquad (1)$$

where Sh is the Strouhal number and $k = \frac{1}{\mathrm{Sh}}$.

The given process has a hydrodynamic nature. Pulsations of the liquid mass with frequency f represent a flow response to a disturbance produced by a body (obstacle in a fluid).

Russian Geographical Society,
Laboratory for Problems of Modeling of Complex Systems, St. Petersburg, Russia

1028-3358/01/4601-0001$21.00

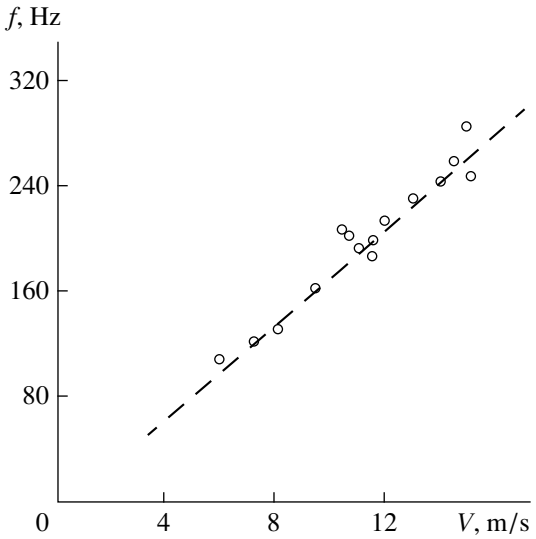

Fig. 1. Frequency f for the collapse of cavitation cavities as a function of the flow velocity V [2].

It should be noted that the frequency f and the flow velocity V are variables in (1). It is appropriate to consider the Strouhal number as a reciprocal quantity for the self-similarity coefficient k [11]. The physical meaning of the coefficient k lies in the fact that, in a flow, an attached mass in the form of a cavitation cavity is formed beyond a body of size L. After separation, this cavity generates pulsations of frequency f. It is worth mentioning that the quantity k varies between 2 and 6 [11].

CAVITY NOISE RADIATION

The cavitation noise measured near collapsing cavities has a characteristic maximum depending on flow velocity V and body size L [3]. We now analyze the frequency of the maximum as a function of the parameters of a body and flow. The effect under consideration is related to the pressure pulsations of the compressible fluid as a result of the action of the fluid flowing around an obstacle with characteristic dimensions L. In this case, the body with a characteristic size L, which is situated in the flow, generates noise radiation with frequency f. This noise radiation propagates through a fluid with a velocity of sound c in the form of a wave having wavelength λ:

$$f^* = c\lambda. \tag{2}$$

It was indicated previously [3] that with increasing frequency, the maximum of the noise radiation of cavitation cavities shifted towards the lowest frequencies. This implies that the wavelength λ of the noise radiation rises with increasing flow velocity. We introduce the normalized velocity $\mathrm{M} = \frac{V}{c}$, where M is the Mach number. In this case,

$$\lambda \sim \mathrm{M}. \tag{3}$$

In addition, as was emphasized in [1, 3], the value of the maximum was determined by the size kL of the cavitation cavity; i.e.,

$$\lambda \sim kL. \tag{4}$$

In view of (3) and (4), the wavelength is determined by the characteristic size kL and depends on the flow velocity V and the Mach number M:

$$\lambda = kL\mathrm{M}. \tag{5}$$

As a result, the noise-radiation frequency and the parameters of the cavity and the flow are interrelated by the dependence

$$f^* = \frac{c}{kL\mathrm{M}}. \tag{6}$$

Relationship (6) exhibits a process having an acoustical nature. The pressure pulsations with frequency f are a response of the compressible liquid to a disturbance produced by a body.

INTERPRETATION OF THE RESULTS AND DISCUSSION

We write out relationship (6) in the form

$$f^* = \frac{V^*}{kL}, \tag{7}$$

where $V^* = \frac{c}{\mathrm{M}}$ is the quantity having the dimension of a velocity with its numerical value considerably exceeding the velocity of sound.

It is interesting that relationships (1) and (6) possess a certain symmetry that can be represented by the relationships

$$\sqrt{VV^*} = C, \quad \sqrt{ff^*} = f_0,$$

where f_0 is the characteristic frequency conjugating frequencies f and f^*.

The symmetry of frequencies f and f^* can be represented in logarithmic form:

$$\log\frac{f}{f_0} = -\log\frac{f^*}{f_0}. \tag{8}$$

Relation (8) represents the interconnection between frequencies f and f^* that characterize two physical processes, namely, acoustic and hydrodynamic processes. The interconnection is realized via parameters characterizing fluid flow (flow velocity V and body size L).

Dependence (8) is shown graphically in Fig. 2. As is seen, frequencies f and f^* are conjugate (i.e., symmetric in logarithmic form) with respect to the frequency f_0 defined by the relation

$$f_0 = \frac{c}{kL}. \tag{9}$$

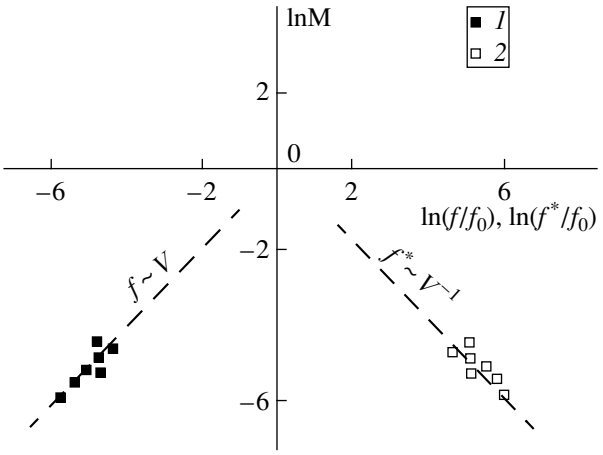

Fig. 2. (*1*) Reduced frequency for generation of cavitation cavities (empirical data) and (*2*) their noise-radiation as a function of relative flow velocity M in the case of hydrodynamic cavitation. The calculation is performed according to formula (8).

The symmetry illustrated by Fig. 2 is characteristic not only of frequencies f and f^* but also of the wavelengths of both processes, i.e., of their spatial characteristics. Thus, relation (8) characterizes the space-time symmetry of dynamic processes having a hydrodynamic and acoustic nature. Similar symmetry was considered in the D-SELF model describing a regulation inherent in self-organized systems [6].

From the standpoint of the D-SELF model, the processes considered above are an effect of self-regulation in the form of a response of a fluid transforming the energy transferred to it from a source that generates noise-radiating cavitation cavities. The energy transformation occurs in the form of the generation of harmonically conjugate processes: a vibrational hydrodynamic process with frequency f and a wave acoustical process with frequency f^*.

The D-SELF model describes the generation of nonlinear processes. Therefore, it is necessary to indicate that along with the generation of frequencies f and f^*, processes with harmonics of frequency f_0 are also excited. In this case, two sets of harmonics arise: harmonics generating cavitation cavities (subharmonics with frequency f_0) and harmonics of noise radiation (subharmonics of frequency f_0). It is important to emphasize that the excited subharmonics with frequencies f_i and f_i^* are conjugate with one another with respect to frequency f_0:

$$\sqrt{f_i f_i^*} = f_0,$$

where i is the ordering number of the ith subharmonic or superharmonic.

Thus, when generating noise-radiating cavitation cavities, conjugation effects will be characteristic of both subharmonics and superharmonics. In this case, it is correct to speak of harmonic conjugation of these effects.

REFERENCES

1. K. K. Shal'nev, Izv. Akad. Nauk SSSR, Otd. Tekh. Nauk **8** (1), 72 (1956).
2. V. I. Il'ichev, Dokl. Akad. Nauk SSSR **136**, 1047 (1961) [Sov. Phys.–Dokl. **6**, 118 (1961)].
3. V. I. Il'ichev and V. P. Lesunovskiĭ, Akust. Zh. **9**, 32 (1963) [Sov. Phys. Acoust. **9**, 25 (1963)].
4. A. G. Ivanov-Rostovtsev and L. G. Kolotilo, Dokl. Akad. Nauk **367**, 677 (1999).
5. A. G. Ivanov-Rostovtsev and L. G. Kolotilo, in *Problems of Investigating the Universe*, Vol. 14: *Problems of Space and Time in Modern Natural Science* (Nauka, Leningrad, 1990), pp. 228–231.
6. A. G. Ivanov-Rostovtsev and L. G. Kolotilo, Izv. Ross. Geogr. Obshch., Suppl. **131** (2), 1 (1999).
7. A. G. Ivanov-Rostovtsev and L. G. Kolotilo, Dokl. Akad. Nauk SSSR **319**, 1132 (1991) [Sov. Phys.–Dokl. **36**, 590 (1991)].
8. A. G. Ivanov-Rostovtsev and L. G. Kolotilo, Dokl. Akad. Nauk **331**, 32 (1993) [Phys.–Dokl. **38**, 280 (1993)].
9. V. A. Smirnov, A. G. Ivanov-Rostovtsev, and L. G. Kolotilo, Dokl. Akad. Nauk SSSR **323**, 314 (1992).
10. M. B. Vinogradova, O. V. Rudenko, and A.O. Sukhorukov, *Theory of Waves* (Nauka, Moscow, 1976).
11. G. M. Degtyarev, A. G. Ivanov-Rostovtsev, L. G. Kolotilo, and O. A. Lyubchenko, Dokl. Akad. Nauk SSSR **313**, 837 (1990).

Translated by Yu. Vishnyakov

Doklady Physics, Vol. 46, No. 1, 2001, pp. 12–16. Translated from Doklady Akademii Nauk, Vol. 376, No. 3, 2001, pp. 318–323.

PHYSICS

A Mechanism of Melting of Microscopic Ice Particles: Numerical Experiment

S. V. Shevkunov

Presented by Academician V.V. Osiko June 2, 2000

Received May 23, 2000

INTRODUCTION

Molecular and atomic clusters attract considerable interest; this can be explained by their intermediate position between molecules, as such, and macroscopic particle ensembles, as well as their position in the hierarchy of systems described by methods of statistical mechanics. Gibbs statistical mechanics also remains valid for systems with a limited number of particles. For the rigorous derivation of an equilibrium distribution function, two conditions should be fulfilled: the size of a thermostat in equilibrium with a molecular system should be macroscopic and the energy of the interaction between the system and the thermostat should be infinitely small compared to the system internal energy. The thermodynamic limit for the number of particles $N \longrightarrow \infty$ in the system in itself is not required [1]. The mechanism responsible for the formation of the collective behavior of particles, which, in the macroscopic limit, leads to phase transitions, is of fundamental interest. In small molecular systems, liquid-crystal transitions are of particular importance in application, since they occur at rather low temperatures, when molecular clusters, within a relatively wide range of external conditions, are stable with respect to decomposition. Strictly speaking, phase transitions accompanied by discontinuities in functional dependences of thermodynamic potentials are possible only in the limit of an infinite number of particles. Phase transitions represent the most complex problem in modern classical statistical equilibrium thermodynamics. In addition, there exists no theory capable of explaining, in the general form, the origin of phase transitions and linking the mechanism of particle interaction with the position of the boundaries separating different phase states in the phase diagram. According to present-day concepts of general statistical theory [2], phase transitions are related to the zeros of the grand statistical sum:

$$\Xi(\lambda, V, T) = \sum_N Q(N, V, T)\lambda^N, \qquad (1)$$

where $Q(N, V, T)$ is the statistical sum of the canonical statistical ensemble, V is the volume, T is temperature, $\lambda = \exp\left(\frac{\mu}{k_B T}\right)$ is the absolute activity, and μ is the chemical potential. In systems with a finite number of particles, the series (1) transforms into a polynomial in powers of λ with positive coefficients which has no real roots. In the macroscopic limit, the number of roots increases and they are aligned along a certain curve. In the case when this curve intersects the real axis of values of λ, the intersection point forms a singularity which we interpret as a phase transition. The limiting distribution law for roots on this curve at the point of its intersection with the real axis probably determines the kind of phase transition. At least, there are no reasons to expect other singularities of functional relation (1) which, after taking the logarithm, would lead to discontinuities of the free energy [3] or its derivatives in the region of finite real λ.

For finite N, the proximity of roots to the real axis affects the statistical behavior of the system in the form of formally continuous but relatively abrupt changes in its properties under temperature variation. In this case, the entropy jumps degenerate into S-shaped dependences and singularities of thermal coefficients are transformed into intense but finite maxima. Strictly speaking, these structural changes in molecular clusters are not phase transitions. However, with increasing N, the anomalies become so clearly pronounced that they are termed melting, evaporation, etc. by analogy with macroscopic systems.

Variations in N give rise to displacement of the polynomial roots in (1) not only towards the real axis but also along it. This implies that the points of structural transitions in clusters depend on their sizes. This dependence was discovered already in the first numerical studies of very simple clusters consisting of noble-gas atoms [4–10]. In [7], it was first shown that in an extremely small system consisting of as little as 16 particles, separation into a liquid core and gas residing in equilibrium with this core was clearly observed. The universal property is a shift of the melting and evaporation points for clusters to lower temperatures. The shift

St. Petersburg State Technical University,
ul. Politekhnicheskaya 29, St. Petersburg, 195251 Russia

1028-3358/01/4601-0012$21.00

magnitude is determined by the character of interparticle interactions. For example, the melting of a cluster consisting of 16 argon atoms occurs at a temperature lower by a factor of three than that of the corresponding macroscopic crystal lattice and the gas-liquid transition is shifted downwards along the absolute-temperature scale by a factor of two. In an ionic system, the shift of structural transition points in clusters is far less significant and is accounted for by the screening effect [11].

THE ROLE OF WATER CLUSTERS IN THE PROBLEM OF OZONE DECOMPOSITION

Water clusters are of special interest. The unique properties of water underlie most of the physicochemical processes in the atmosphere. The freezing point of water is approximately in the middle of the range of usual temperature variations near the Earth's surface, and the equilibrium conditions for the vapor and liquid phase are close to the natural conditions in the atmosphere. This provides the inclusion of phase transitions occurring in water into a sequence of local and seasonal variations of atmospheric conditions. The latent heat of phase transitions serves as an energy accumulator smoothing these vibrations and enhancing natural convection. In the stratosphere, at altitudes on the order of several tens of kilometers, specific conditions are realized for the existence of clusters of water molecules. It should be expected that the characteristic temperatures of 180 to 220 K at these altitudes correspond to a boundary between the solid-crystal and quasi-liquid states of water clusters. Relatively small seasonal temperature variations can give rise to changes in the cluster phase states and affect the behavior of physicochemical processes on the cluster surface. The most important phenomenon of such kind is the process of decomposing the natural ozone layer in the stratosphere. The ozone is decomposed in the reaction of oxidizing free chlorine, which is, in turn, a product of decomposing chlorine-containing CCl_2F_2 and CCl_3F Freons, as well as foam-forming compounds of the CH_3CF_2Cl type. The interaction of chlorine and its oxide with NO_2 and CH_4 gases results in the binding of active chlorine in the form of such compounds as HCl and $ClONO_2$, which are chemically inert with respect to ozone. At this stage, the ozone decomposition cycle would be completed, but atomic chlorine can be liberated from these compounds in the reactions

$$HCl + HOCl \longrightarrow Cl_2 + H_2O, \quad (2)$$

$$HCl + ClONO_2 \longrightarrow Cl_2 + HNO. \quad (3)$$

In the gaseous phase, the chlorine is liberated extremely slowly. However, the ice surface acts as a catalyzer, accelerating reactions (2) and (3) and again producing the active chlorine. In the circumpolar regions at altitudes up to 100 km, the formation of specific stratospheric clouds containing ice microparticles is observed [12]. The appearance of these clouds is correlated with intensifying the process of ozone decomposition and formation of so-called ozone holes. Chemically passive HCl is adsorbed on the surface of ice microparticles, and in the period of seasonal warming with the income of the arctic spring, it becomes a source for the materials of reactions (2) and (3). The cause of this enhanced temperature effect may be the melting of water clusters on the adsorbing surface of microparticles. The single-crystal ice surface has a complex microrelief, depending on the history of its formation. This relief represents clusters of water molecules irregularly adhering to one another. Since the melting temperature for clusters depends on their size, the elevation of temperature results, in the first turn, in the melting of smaller-size clusters, whereas the larger-size clusters can remain in the solid-crystalline state. According to present-day concepts [13], acceleration of reactions (2) and (3) occurs due to the formation of intermediate annular cluster HCl structures with water molecules which are extracted from the surface of ice microparticles. The probability of detachment of a water molecule from the ice surface and, consequently, its catalytic effect are determined by the mobility of the molecules, which, in turn, is related to the phase state of that microscopic surface area on which the chemical reactions take place. The melting of clusters must lead to an increase in the active surface and to acceleration of free-chlorine production. Thus, the melting of small clusters is one of the key components in the chain of reactions causing ozone decomposition.

RESULTS OF NUMERICAL EXPERIMENTS

In this paper, we study the melting of clusters consisting of 40 and 10 water molecules. The melting was identified according to the behavior of the internal energy, heat capacity, and electric susceptibility. The heat capacity was calculated via energy-interaction fluctuations, U, [3]:

$$C_V = \frac{\langle U^2\rangle - \langle U\rangle^2}{k_B T^2}. \quad (4)$$

Formula (4) yields the nonideal component of heat capacity, which differs in a trivial term $\frac{6}{2}Nk_B$ from the total heat capacity for rigid molecules with six degrees of freedom. The diagonal elements in the tensor of static electric susceptibility were calculated on the basis of fluctuations of the dipole moment **P**:

$$\alpha_{xx} = \frac{\langle P_x^2\rangle - \langle P_x\rangle^2}{k_B T} + \alpha_w, \quad (5)$$

where $\alpha_w = 1.44 \times 10^{-3}$ nm^3 is the isotropic polarizability of the water molecules.

The calculations were performed by the Monte Carlo method for the canonical statistical ensemble [3]. We used the standard Metropolis scheme. One step of

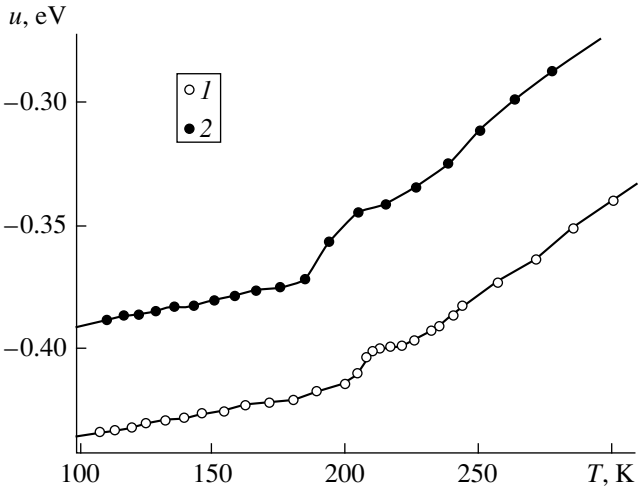

Fig. 1. Internal energy (without kinetic component $\frac{6}{2}k_BT$) estimated for one molecule: (*1*) $(H_2O)_{40}$ and (*2*) $(H_2O)_{10}$.

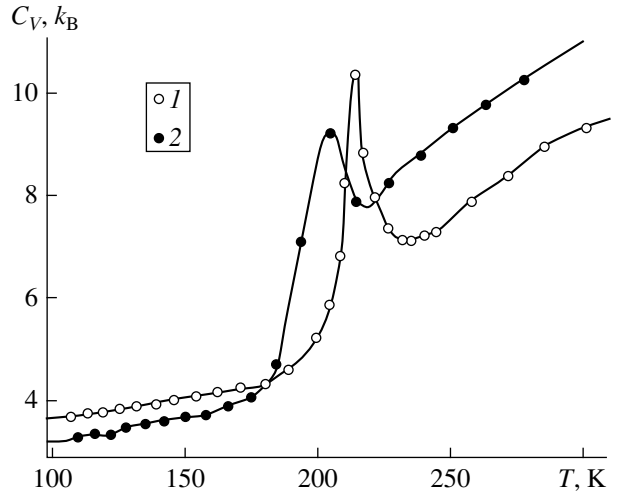

Fig. 2. Specific heat (without the kinetic component $\frac{6}{2}k_B$) estimated for one molecule at a constant volume: (*1*) $(H_2O)_{40}$ and (*2*) $(H_2O)_{10}$.

the procedure consisted in a spatial shift and rotation of a molecule around three Cartesian axes. The fraction of new configurations taken was 50–60%. The iteration-step length and the rotation angle ranged from 0.01 to 0.05 nm and 20° to 30°, respectively, depending on the calculation conditions. One Markovian chain consisted of 100×10^6 steps, the first 10×10^6 steps allotting for thermalization. To avoid evaporation, the system was placed into a spherical cavity with a radius of 1.2 nm. The interaction of the molecules is described by the Raman–Stillenger ST2 pair five-center intermolecular potential. The potential explicitly simulates the exchange, dispersion, and Coulomb interactions, as well as directed hydrogen bonds. In this model, unpaired interactions are taken into account implicitly. Priority was taken for the ST2 potential, since it belongs to the most successful intermolecular potentials developed for water. Unlike, for example, the SPC model, this potential explicitly takes into account the tetrahedral structure of the interactions in the first coordination layer of the molecules. Strictly speaking, the domain of applicability of the arbitrary modeling intermolecular potential is limited by the particular temperature range, so that the range under investigation lies on the boundary of the applicability of the ST2 model. Nevertheless, we deliberately use this model, since the goal of the present study is to reproduce the basic features related to the melting of clusters containing narrow-directed hydrogen bonds rather than a precise calculation of the water thermodynamic characteristics.

In the vicinity of the melting point 273 K of the macroscopic phase, there is no evidence in the temperature curves for the cluster equilibrium characteristics of any qualitative changes in the system which resemble melting. The melting temperature of a cluster consisting of 40 molecules is shifted downward to 210 K. At this point, a change in the slope on the internal energy curve and a small jump (approximately 0.02 eV, i.e., $\sim k_BT$ accounted for one molecule) occurs, Fig. 1. At this point, a maximum on the temperature dependence of the heat capacity against the background of its general accelerated drop (approximately by a factor of two) is formed while cooling the system, Fig. 2. The melting does not occur strictly jump-wise but is extended in a temperature scale ranging in an interval of approximately 10 K. According to the behavior of calorimetric characteristics, the melting of the cluster consisting of 10 molecules occurs at approximately 200 K and is more strongly extended in the temperature scale (Figs. 1, 2). In the vicinity of the melting point from the side of lower temperatures, the heat capacity differs by 25% from its low-temperature limit of $3k_B$, which corresponds to harmonic vibrations in the crystal lattice, thus demonstrating the degree of anharmonicity of thermal vibrations in the crystal. In [14], the melting of clusters $(H_2O)_6$ and $(H_2O)_8$ was investigated by a method of molecular dynamics. The behavior of the Lindemann factor testified to the fact that the melting of clusters composed of six and eight particles corresponded to temperatures of 60 and 170 K, respectively. Our results are in agreement with both the data of [14] and the general regularity of increasing the melting temperature with the cluster size.

In macroscopic molecular systems, crystallization is associated with the formation of long-range molecular ordering and a drastic decrease in the diffusion coefficient. The long-range ordering cannot be realized in these clusters by virtue of their spatial boundedness, and the diffusion motion for the distances on the order of the cluster size is difficult to distinguish from the thermal motion. In spite of this fact, the numerical experiment shows that the cluster cooling is accompa-

nied by drastic qualitative changes which affect the temperature dependences of their equilibrium characteristics. In the systems with pair interactions, the internal energy is expressed as an integral of binary correlation functions. Therefore, any strong changes in energy inevitably imply certain drastic changes in the correlation functions. However, when melting, the relative change in relevant quantities turns out to be too small to be noted in a simple visual analysis of the correlation functions. For example, the oxygen–oxygen $g_{OO}(r)$ correlation-function curves (Fig. 3), while cooling, exhibit a gradual rise in oscillations, which indicates the continuous amplification of the correlations in the spatial positions of molecule centers of mass. However, the positions of the maxima remain, in fact, invariable: no new maxima are formed and the qualitative steps in the increase in the correlations remain virtually indistinguishable. More thorough analysis is based on calculating orientational correlation functions. For binary orientational correlation functions, the qualitative changes associated with melting are identified much more reliably. Above the melting point, a monotonous reduction of the orientational correlations is observed on the dependence of the mean angle between the dipole moments of the molecules on the distance between them along the symmetry axis of one of the molecules. After melting, the situation changes qualitatively. The monotonous dependence becomes oscillating. The strongest orientational correlations are observed for intermolecular distances corresponding to maxima of $g_{OO}(r)$ in Fig. 3, i.e., in coordination layers. In spacings between layers, the correlations are even reduced with cooling. The oscillation amplitude in the orientational correlations begins to rise at the melting point and continuously increases with further lowering of the temperature. Thus, the distinctive feature of the crystallization in bounded systems with a strong anisotropic intermolecular interaction is the appearance of a spatial nonuniformity in the orientational correlations of the particles. We expect that in macroscopic systems of the same type, the orientational correlations under the crystallization would also undergo strong changes along with other structural characteristics. However, the specific nature of a small molecular system consists in the fact that the change in the orientational correlations turns out to be the most well-pronounced event that allows us to judge the character of the structural changes. It is worth noting that the changes in the cluster structure in the process of crystallization do not reduce to a simple amplification of the orientational correlations. The essence of the changes is the spatial redistribution of these correlations in accordance with already existing correlations in the positions of molecule centers of mass. The melting is a process of violating the dependence between orientational and translational correlations in the system.

In systems with strongly different energy scales for the isotropic and anisotropic components of interparticle interactions, in principle, two different phase transitions of translational and orientational ordering are possible. Alloys based on iron, nickel, or cobalt may be used as an example. In these alloys, with a rise in temperature, the destruction of ferromagnetic properties and melting occur at different temperatures. The destruction temperatures for the long-range translational and orientational orders are also separated in liquid crystals. In most materials, particularly in water, both forms of the long-range molecular order are destroyed simultaneously while melting. This behavior is most typical of real substances and can be explained by the fact that for the existence of two different phase-transition orderings, the anisotropic component must be significantly weaker than the isotropic component of the interaction. However, in the case of an overly weak anisotropic interaction, the transition to an orientational ordered phase will occur at an overly low temperature, when the effects associated with quantum-mechanical uncertainty in the particle positions become significant. Then, the behavior of the system changes qualitatively.

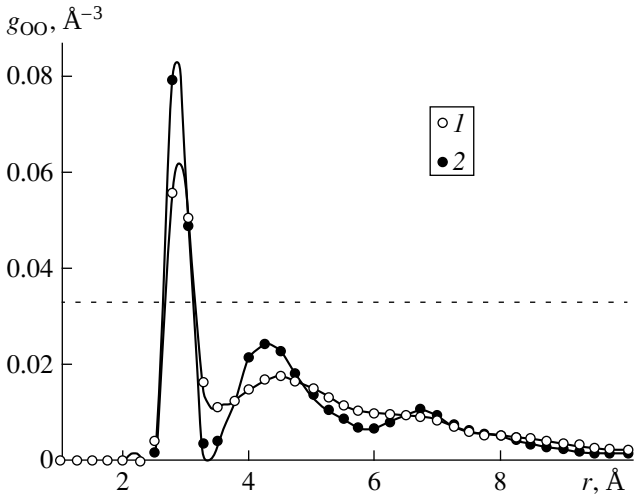

Fig. 3. Oxygen–oxygen correlation function for the $(H_2O)_{40}$ cluster normalized to the number (with one less) of molecules: (*1*) T = 300 and (*2*) 162 K. The dashed line is the total density of water under normal conditions.

Theoretically, it is possible to expect that the points of the translational and orientational ordering can be separated in the temperature scale due to the extreme smallness of the system. With decreasing the cluster size, the average number of neighboring particles in the nearest coordination layer also decreases. If the orientational ordering is more sensitive to the number of closest neighbors, the appearance of the orientational order may be shifted towards low temperatures. It is this effect that we observed in the cluster consisting of 10 molecules. The polarizability is sensitive to the orientational ordering. The qualitative changes in the orientational order are accompanied by the intensified fluctuation rotations of molecules and, by virtue of (5), by the rise in polarizability. If for the cluster consisting of 40 molecules, the maxima of the polarizability and

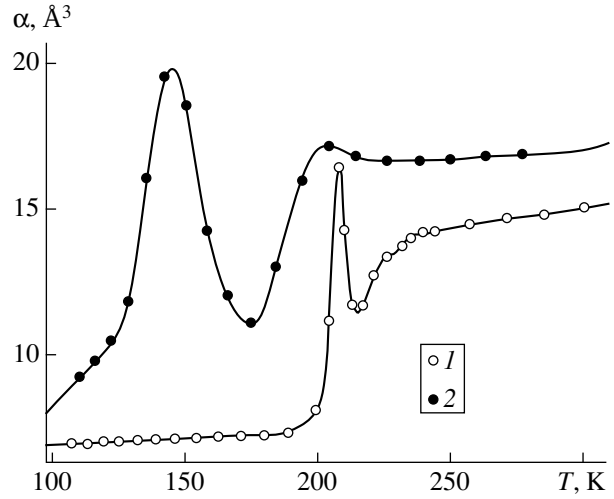

Fig. 4. Cluster polarizability estimated for one molecule: (*1*) $(H_2O)_{40}$ and (*2*) $(H_2O)_{10}$.

thermal capacity coincide in temperature scale, then for a cluster composed of 10 molecules, we have obtained a strong polarizability maximum at a much lower temperature of 150 K (Fig. 4). Here, the rare but strong fluctuations of the dipole moment associated with correlated rotations as a whole of groups composed of two to four molecules are observed. The distribution function for the cluster moment squared has a bimodal shape. The rotations do not need to overcome activation barriers, as is the case for larger clusters. Therefore, they do not contribute to the heat capacity (Fig. 2). It is evident that an increase in the cluster size of up to 40 molecules eliminates such barrier-free paths in the system configuration space and that the orientational order is stabilized at higher temperature. In [15], the melting point of $(H_2O)_8$ was evaluated as, approximately, 150 K by the molecular-dynamics method, according to the behavior of the Lindemann factor. The melting of the $(H_2O)_{12}$ cluster corresponded to the same temperature with an accuracy to an error inherent in this method, and the $(H_2O)_{24}$ cluster was melted at approximately 170 K. The estimates of [15] for clusters consisting of 8 and 12 molecules contradict the data of [14] for a cluster consisting of 8 molecules (the melting temperature is 170 K) and correspond to the maximum of electric susceptibility for the cluster modeled by us and consisting of 10 molecules, which is shown in Fig. 4. At these temperatures, we failed to observe the extremum of the heat capacity. We consider that the phase transition in these extremely small clusters is significantly extended in the temperature scale. Then, by virtue of the effects discussed above, different characteristics may attain their extrema at essentially different temperatures. This is a likely source of the discrepancies observed in the positions of the melting points determined in various ways.

ACKNOWLEDGMENTS

This work was supported by INTAS, grant no. 99-01162.

REFERENCES

1. C. Kittel, *Thermal Physics* (Wiley, New York, 1973; Nauka, Moscow, 1977).
2. L. D. Landau and E. M. Lifshitz, *Statistical Physics* (Nauka, Moscow, 1976; Pergamon, Oxford, 1980).
3. T. L. Hill, *Statistical Mechanics. Principles and Selected Applications* (McGraw-Hill, New York, 1956).
4. C. L. Brian and J. J. Burton, Nature **243** (128), 100 (1973).
5. R. D. Etters and J. Kaelberer, Phys. Rev. A **11**, 1068 (1975).
6. P. N. Vorontsov-Vel'yaminov and V. A. Pavlov, Teplofiz. Vys. Temp. **13**, 302 (1975).
7. V. A. Pavlov and P. N. Vorontsov-Vel'yaminov, Teplofiz. Vys. Temp. **15**, 1165 (1977).
8. E. N. Brodskaya and A. I. Rusanov, Kolloidn. Zh. **39**, 636 (1977); **39**, 646 (1977).
9. J. Jellinek, T. L. Beck, and R. S. Berry, J. Chem. Phys. **84**, 2783 (1986).
10. T. L. Beck and R. S. Berry, J. Chem. Phys. **88**, 3910 (1988).
11. S. V. Shevkunov and P. N. Vorontsov-Vel'yaminov, Teplofiz. Vys. Temp. **20**, 1025 (1982).
12. S. Solomon, R. R. Garcia, F. S. Rowland, and D. J. Wuebbles, Nature **755**, 321 (1986).
13. S. Ch. Xu, J. Chem. Phys. **111**, 2242 (1999).
14. J. Rodriguez, D. Laria, E. J. Marceca, and D. A. Estrin, J. Chem. Phys. **110**, 9039 (1999).
15. M. Masella, J. Chem. Phys. **111**, 5081 (1999).

Translated by Yu. Vishnyakov

Doklady Physics, Vol. 46, No. 1, 2001, pp. 17–20. Translated from Doklady Akademii Nauk, Vol. 376, No. 1, 2001, pp. 36–39.

TECHNICAL PHYSICS

Propagation of Sound in a Thin Cylindrical Rod Immersed in a Fluid

S. L. Bazhenov, A. K. Rogozinskiĭ, and Corresponding Member of the RAS A. A. Berlin

Received July 11, 2000

The velocity of a longitudinal acoustic wave in a thin elastic rod decreases if the rod is immersed in a fluid [1]. The reduction in the velocity of sound is explained by the fact that a boundary layer of fluid vibrates along with the rod metal. The thickness of this layer depends on the frequency of rod vibrations and also on the density and viscosity of the fluid. For a sound frequency of 100 kHz, the thickness of the fluid boundary layer is 10 to 50 μm for moderately viscous fluids similar to oil [1]. If the mass of the boundary layer in the fluid is comparable with the mass of the rod, the reduction in the velocity of sound is substantial. In macroscopic samples with a thickness larger than 1 mm, no effect is observed.

The boundary-layer thickness of the fluid depends on its viscosity. This made it possible to use the effect of decreasing the velocity of sound for determining the viscosity of the fluid. This method is rather rapid, which makes it possible to measure up to 3000 experimental points per second. As a sensor, a thin aluminum strip was used [1]. However, it is more convenient from the engineering standpoint to use a fiber instead of a strip. Therefore, the goal of this paper is to investigate the effect of fluid on the propagation of sound in a thin fiber.

As a sensor, we used nichrome fibers (wires) with an operating length of 210 mm and a diameter of 100 and 150 μm. The fiber immersed in the bath with the fluid was placed in a thermostatically controlled chamber. After the desired temperature had been attained, an ultrasonic pulse with a frequency of 250 kHz was transmitted through the fiber and the time of the pulse propagation through the sample was determined. The ultrasound velocity was calculated by dividing the sample length by the signal-passage time.

We consider the propagation of a longitudinal acoustic wave in an elastic cylindrical rod immersed in an unbounded Newtonian fluid (Fig. 1). The presence of the fluid was taken into account by adding to the wave equation a term describing the fiber–fluid interaction:

$$\pi R^2 \rho_0 \frac{\partial^2 u}{\partial t^2} = \pi R^2 E \frac{\partial^2 u}{\partial Y^2} + 2\pi R\tau. \quad (1)$$

Here, u is the displacement of the fiber from the equilibrium position, Y is the direction of the fiber axis, ρ_0 is the density, R is the radius, πR^2 is the cross section, E is the fiber elastic modulus, and τ is the stress induced by the interaction of the fiber with the fluid.

For finding shear stress τ, we solve the problem of the motion of the fluid contacting the fiber. Let an unbounded cylindrical rod of radius R be in contact with an incompressible viscous fluid being, as a whole, quiescent, and let this rod undergo longitudinal harmonic vibrations with an angular frequency ω along its Y-axis. We assume that the fluid is Newtonian, the viscosity is proportional to the velocity gradient, and the motion of the fluid in the cylindrical coordinate system can be described by the equation

$$\rho \frac{\partial v}{\partial t} = \eta\left(\frac{\partial^2 v}{\partial r^2} + \frac{1}{r}\frac{\partial v}{\partial r}\right), \quad (2)$$

where v is the velocity of the fluid along the fiber vibration axis Y, ρ is the density, and η is the viscosity of the fluid.

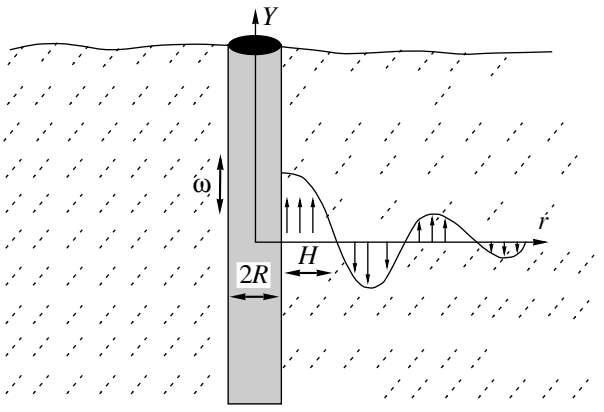

Fig. 1. Schematic diagram for computation. Y is the fiber axis, R is the fiber radius, and ω is the angular frequency of vibrations.

Semenov Institute of Chemical Physics, Russian Academy of Sciences, ul. Kosygina 4, Moscow, 117977 Russia

1028-3358/01/4601-0017$21.00

We seek the time-periodic solution to Eq. (2) in the form

$$v(r, t) = s(r)\exp(i\omega t),$$

where i is the imaginary unit. Substituting $v(r, t)$ into (2) and performing the change of variables $x = \sqrt{\frac{\omega\rho}{\eta}}r$, we obtain

$$\frac{\partial^2 s}{\partial x^2} + \frac{1}{x}\frac{\partial s}{\partial x} - is = 0. \quad (3)$$

Equation (2) is the Bessel equation of the argument $xi\sqrt{i}$ [2, 3]. The solution to this equation, which damps at infinity, is known as the Bessel function of the second kind of the argument $xi\sqrt{i}$ [2] or the Russel function [3, 4]:

$$s = s_0(\mathrm{ker}x + i\mathrm{kei}x). \quad (4)$$

The functions ker and kei are, respectively, the real and imaginary parts of the Russel function. They are calculated in the form of a series [2, 3], and tables describing them can be found in [4]. These functions oscillate with decreasing amplitude with an increase in x (i.e., the distance to the fiber axis).

Note that the wave $v(r, t)$ excited in the fluid is the shear wave, and it propagates along the direction perpendicular to the fiber axis. Once the problem of wave propagation in the fluid has been solved, we can return to the problem of sound propagation in the fiber. The fiber–fluid interaction stress is $\tau = \eta\frac{\partial s}{\partial r}$ for $r = R$. Differentiating (4), we arrive at

$$\tau = s_0\sqrt{\eta\omega\rho}(\mathrm{ker}'x_0 + i\mathrm{kei}'x_0)\exp(i\omega t). \quad (5)$$

Here, $x_0 = \sqrt{\frac{\omega\rho}{\eta}}R$, $\mathrm{ker}'x = \frac{d\mathrm{ker}x}{dx}$, and $\mathrm{kei}'x = \frac{d\mathrm{kei}x}{dx}$. It is easy to show that $\sqrt{\frac{\omega\rho}{\eta}} = \frac{2\pi}{\lambda_r}$, where λ_r is the length of the wave excited in the fluid [1]. Thus, $x_0 = 2\pi R/\lambda_r$ is the dimensionless parameter describing the ratio between the fiber diameter and the wavelength of the transverse wave in the fluid.

The solution to Eq. (1) for the longitudinal vibrations of the fiber is found in the form

$$u = u_0\exp[i(\omega t - ky)],$$

where k is the wave number. In this case, the velocity $v = \frac{\partial u}{\partial t}$ of a rod element is determined by the relationship

$$v = i\omega u_0\exp[i(\omega t - ky)]. \quad (6)$$

Equalizing the velocity of the fluid $s_0(\mathrm{ker}x + i\mathrm{kei}x)\times\exp(i\omega t)$ to that (6) of the fiber at the boundary $x = x_0$, we find

$$i\omega u_0 = s_0(\mathrm{ker}x_0 + i\mathrm{kei}x_0). \quad (7)$$

The substitution of Eqs. (5) and (7) into (1) yields

$$\rho_0 R\omega^2 = ERk^2 - \frac{2i\omega\sqrt{\eta\omega\rho}(\mathrm{ker}'x_0 + i\mathrm{kei}'x_0)}{\mathrm{ker}x_0 + i\mathrm{kei}x_0}. \quad (8)$$

Thus, we obtain the wave number k:

$$k^2 = \frac{\omega^2}{c_0^2}(1 + \alpha + i\beta), \quad (9)$$

where

$$\alpha = \sqrt{\frac{2\rho\eta}{\rho_0^2 R^2\pi f}}\frac{\mathrm{ker}'x_0\mathrm{kei}x_0 - \mathrm{kei}'x_0\mathrm{ker}x_0}{\mathrm{ker}^2x_0 + \mathrm{kei}^2x_0},$$
$$\beta = i\sqrt{\frac{2\rho\eta}{\rho_0^2 R^2\pi f}}\frac{\mathrm{ker}'x_0\mathrm{ker}x_0 + \mathrm{kei}'x_0\mathrm{kei}x_0}{\mathrm{ker}^2x_0 + \mathrm{kei}^2x_0}, \quad (10)$$

and $f = \frac{\omega}{2\pi}$ is the frequency of sound. On the basis of (9), we determine the velocity of sound as a ratio of the angular frequency to the wave-number modulus:

$$c = \frac{c_0}{\sqrt[4]{(1 + \alpha)^2 + \beta^2}}. \quad (11)$$

The asymptotic behavior of the ker and kei functions for $x \gg 1$ is described by the relationships [1]

$$\mathrm{ker}x \simeq \sqrt{\frac{\pi}{2x}}\exp\left(-\frac{x}{\sqrt{2}}\right)\cos\left(\frac{x}{\sqrt{2}} + \frac{\pi}{8}\right),$$

$$\mathrm{kei}x \simeq -\sqrt{\frac{\pi}{2x}}\exp\left(-\frac{x}{\sqrt{2}}\right)\sin\left(\frac{x}{\sqrt{2}} + \frac{\pi}{8}\right),$$

$$\mathrm{ker}'x \simeq -\sqrt{\frac{\pi}{2x}}\exp\left(-\frac{x}{\sqrt{2}}\right)\cos\left(\frac{x}{\sqrt{2}} - \frac{\pi}{8}\right),$$

$$\mathrm{kei}'x \simeq \sqrt{\frac{\pi}{2x}}\exp\left(-\frac{x}{\sqrt{2}}\right)\sin\left(\frac{x}{\sqrt{2}} - \frac{\pi}{8}\right).$$

For $x \gg 1$, the coefficients $\alpha = \beta = \gamma$, where

$$\gamma = \sqrt{\frac{\rho\eta}{\rho_0^2 R^2\pi f}}. \quad (12)$$

Expanding (11) into a series and restricting ourselves to linear terms of the expansion, we obtain

$$c \simeq c_0\left(1 - \frac{1}{2R\rho_0}\sqrt{\frac{\rho\eta}{\pi f}}\right), \quad (13)$$

where c_0 is the velocity of sound in the fiber in the absence of fluid. The imaginary part of wave number k (9) determines the damping of the longitudinal wave in the fiber:

$$u = u_0 \exp(-\beta z) \approx \exp\left(-\sqrt{\frac{\pi f \rho \eta}{R^2 \rho_0^2 c_0^2}} y\right). \qquad (14)$$

Note that the effect of fluid on the velocity of sound in a cylindrical fiber is similar to that in a thin strip [4]. The asymptotic formulas (at $\frac{R}{\lambda_r} \gg 1$) describing the effect of fluid on the velocity and damping of sound coincide in the case when the fiber diameter is equal to one-half the strip thickness.

In Fig. 2, we display the experimental data for the velocity of sound as a function of the temperature of the nichrome wire immersed in glycerin or an oil. In a pure metal (curves *1*, *2*), the velocity of sound decreases linearly with increasing temperature. The immersion of the fiber in the fluid leads to a reduction in the velocity of sound. The magnitude of this effect decreases with elevation of the temperature and reduction in the fiber diameter. This effect manifests itself more drastically in viscous glycerin than in oil. Such a behavior agrees completely with formula (13).

Above, we have solved the problem of the effect of a fluid on the propagation velocity of an acoustic wave. However, the solution of the inverse problem, namely, determining the viscosity of fluid according to the known reduction in the velocity of sound after the immersion of the fiber in a fluid, is of greater importance. This problem can be solved on the basis of formula (13):

$$\eta \approx \frac{\pi f \rho_0^2}{\rho} \frac{(c_0 - c)^2}{c_0^2}. \qquad (15)$$

In Fig. 3, we demonstrate the correlation between the viscosity determined from Eq. (15) and the tabular values for the viscosities of glycerin and spindle oil at various temperatures [10]. The difference between the calculated and tabular values does not exceed 25%. The only exception is the region of low viscosities (<0.1 Pa s) in which formula (15) overestimates the viscosity. The reason for this fact remains unclear.

The difference between the calculated and experimental data in the case of high viscosity of the fluid can be caused by the inaccuracies in formulas (13) and (15). The effect of the fluid is characterized by the reduction in the velocity of sound $\Delta c = c_0 - c$. The inaccuracy of formula (13) can be estimated by the ratio $\frac{\Delta c_2}{\Delta c_1}$, where Δc_2 is determined from (13), while Δc_1 is found by numerical calculation from exact formula (11). In

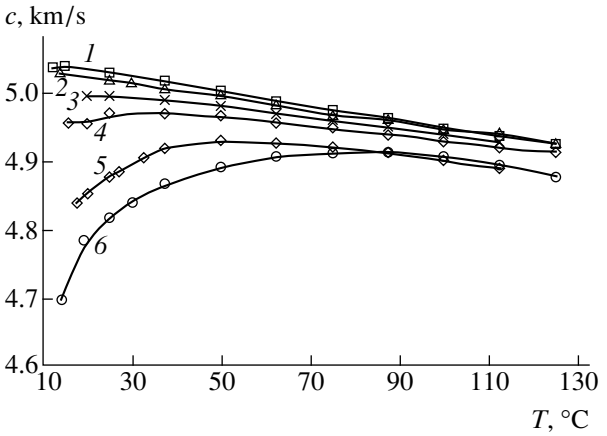

Fig. 2. Ultrasound velocity c as a function of temperature T. The nichrome-wire diameter is (*1*, *3*, *5*) 0.15 mm and (*2*, *4*, *6*) 0.10 mm. Tests were performed (*1*, *2*) in air, (*3*, *4*) in spindle oil, and (*5*, *6*) in glycerin.

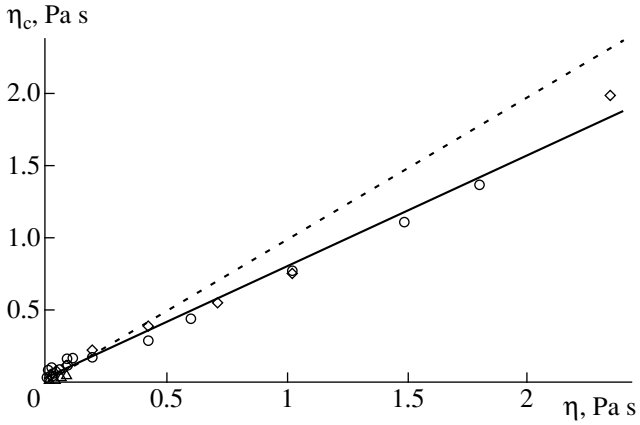

Fig. 3. Correlation between the calculated viscosity η_c of a fluid and the tabular value of viscosity η. Notation is the same as in Fig. 2.

Fig. 4, we display the ratio $F = \frac{\Delta c_2}{\Delta c_1}$ as a function of the parameter $x_0 = \sqrt{\frac{\omega \rho}{\eta}} R$. For all x_0, this ratio is smaller than unity. Consequently, in actual conditions, the effect is slightly higher than that predicted by formula (13). This implies that the calculation of viscosity by formula (15) results in overestimating the viscosity for small x_0. Under the conditions of the experiment, x_0 varied from 1.5 (a fiber 0.1 mm in diameter in glycerin at 14°C) to 30. The minimum value of F for $x_0 = 1.5$ was 0.9. It is easy to show that, for this value of F, formula (15) leads to a relative error of ~20% in the measured viscosity. The inaccuracy in formula (15) can be ignored if the error in measuring the viscosity does not exceed 5%. Based on Fig. 4, we can show that this condition is fulfilled for $x_0 > 4$. Note also that, with allow-

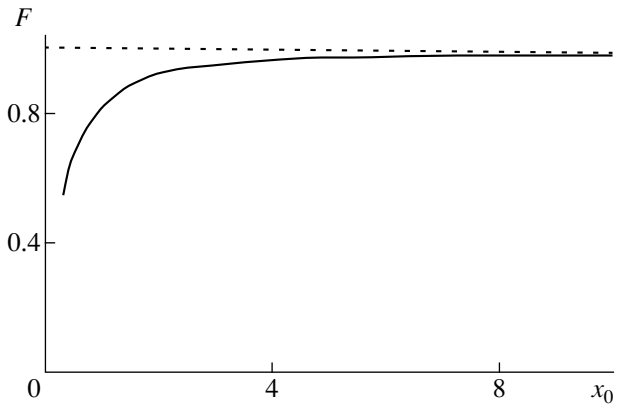

Fig. 4. Ratio $F = \frac{\Delta c_2}{\Delta c_1}$ as a function of dimensionless parameter $x_0 = \sqrt{\frac{\omega\rho}{\eta}}R$. Δc_2 was determined from formula (13), and Δc_1 is the result of a computer calculation according to exact formula (11). Δc is the reduction in the ultrasound velocity after immersion of the fiber in a fluid.

ance for (13), the parameter x_0 is associated with the reduction in velocity Δc by the relation

$$x_0 = \frac{0.71\rho}{\rho_0}\frac{c_0}{\Delta c}. \quad (16)$$

According to (16), parameter x_0 is inverse to the relative value of the effect of reduction in velocity Δc, from where x_0 can be directly estimated using the value of the reduction in the velocity of sound.

Thus, the presence of fluid leads to a decrease in the velocity of an acoustic wave in a fiber after it has been immersed in fluid. The problem is reduced to a plane one if the dimensionless parameter x_0, equal approximately to the ratio between the fiber diameter and the wavelength of the transverse wave in the fluid, exceeds 4. In this case, we can use approximate relations (13)–(15) to determine the effect of the fluid. Otherwise, it is necessary to take into account the fiber curvature using relationships (10) and (11).

REFERENCES

1. A. K. Rogozinskiĭ, S. L. Bazhenov, and A. A. Berlin, Dokl. Akad. Nauk **362**, 481 (1998) [Dokl. Phys. **43**, 616 (1998)].
2. H. B. Dwight, *Tables of Integrals and Other Mathematical Data* (Macmillan, London, 1961; Nauka, Moscow, 1973).
3. G. N. Watson, *Treatise on the Theory of Bessel Functions* (Cambridge Univ. Press, Cambridge, 1945; Inostrannaya Literatura, Moscow, 1949).
4. G. N. Watson, *Treatise on the Theory of Bessel Functions* (Cambridge Univ. Press, Cambridge, 1945; Inostrannaya Literatura, Moscow, 1949), Part 2.
5. *Handbook of Chemistry and Physics* (Chemical Rubber, Cleveland, 1955).

Translated by V. Bukhanov

Doklady Physics, Vol. 46, No. 1, 2001, pp. 21–25. Translated from Doklady Akademii Nauk, Vol. 376, No. 2, 2001, pp. 186–190.

TECHNICAL PHYSICS

R-Function Method for Simulating Thermal Processes in the Case of Radiating Complex-Shaped Bodies

V. F. Kravchenko*, Corresponding Member of the RAS V. I. Pustovoĭt, V. L. Rvachev***, and N. D. Sizova*****

Received June 26, 2000

INTRODUCTION

Problems on evaluating the temperature field for a radiating body are of great practical importance in studies of aircraft components. In such problems, a boundary condition is typically represented in the form of a functional relation (a functional) connecting the heat flow at an arbitrary point on the wall of the object under investigation with the temperature field at its other points. The heat transfer by radiation for such objects subjected to heating by solar radiation is presently being investigated. The temperature field of the body under study is found from its known radiation capacity. The results of the investigation of the heat-transfer process, as applied to regions having the shape of hollow cylinders, polygons, and cubic boxes, are presented in [1]. In this new approach, the functional relation in a boundary condition is assumed to be represented in the form of three-dimensional harmonics inside the body. This makes it possible to reduce the heat-conductivity problem to a system of differential equations in these harmonics and to linearize this system by an iterative procedure. However, this approach is hard to implement for more complicated geometric objects, since a function allowing for the geometry factor that enters into the functional relation for the boundary condition cannot always be constructed. In this paper, we pioneer the use of the *R*-function method [2] for finding the temperature field of a radiating body having an arbitrary geometric shape.

* *Institute of Radio Engineering and Electronics, Russian Academy of Sciences, ul. Mokhovaya 18, Moscow, 103907 Russia*

** *Research Technological Center of Unique Instrumentation, Russian Academy of Sciences, ul. Butlerova 15, Moscow, 117342 Russia*

*** *Institute of Mechanical Engineering Problems, National Academy of Sciences of Ukraine, ul. Dm. Pozharskogo 2/10, Kharkov, 310046 Ukraine*

FORMULATION OF THE PROBLEM

We represent the system of heat-conductivity equations for a heat-radiating body $\Omega \in R^3$ with a boundary S, which is placed into an external field, in the following form:

$$k\nabla^2 T(x,t) + \bar{q}(x) = c\frac{\partial T(x,t)}{\partial t}, \quad x \in (x_1, x_2, x_3), \tag{1}$$

$$T = T_0 \text{ for } t = 0, \quad t \in [0, \tau], \tag{2}$$

$$\frac{\partial T}{\partial n} = 0 \text{ at the } S. \tag{3}$$

In (1), c is the specific-heat coefficient, k is the heat-conductivity coefficient, and $\bar{q}(x)$ is the heat-source function for the body Ω. Equations (2) and (3) describe the initial and boundary conditions, respectively. The function $\bar{q}(x)$ in the interior of the region Ω is represented by the relation

$$\bar{q}(x) = \bar{q}^*(x) + q(x), \tag{4}$$

where

$$q(x) = \begin{cases} \lim\limits_{dn \to 0} \dfrac{q_i + q_l - q_n}{dn} & \text{within the volume } Sdn \\ 0 & \text{within the rest of the space;} \end{cases}$$

q_i is the incoming heat flow from all external points of the body surface, q_u is the outgoing heat flow, and q_l is the total heat flow which is assumed to be known *a priori*. Thus, the surface sources are concentrated inside of this layer with elementary thickness dn along the boundary S of the body Ω. The outgoing heat flow q_u for the dissipated radiation in vacuum is written in the form of the following functional expression:

$$q_u(x) = F(x) + r(x)\int_S q_u(x')\chi(x,x')dS'. \tag{5}$$

Here, $F(x) = \sigma\varepsilon(x)T^4(x)$ is the function describing the direct radiation from the boundary S (i.e., wall) of the

1028-3358/01/4601-0021$21.00 © 2001 MAIK “Nauka/Interperiodica”

body Ω; $r(x)$ is the function describing the wall reflectivity, which is independent of both the wavelength and the direction of the incident wave; $\chi(x, x')$ is the function responsible for the geometry of the region; σ is the radiation (or the Stefan–Boltzmann) constant; and $\varepsilon(T)$ is the degree of the body's blackness. Equation (5) is an integral equation with respect to the unknown function $q_u(x)$. The solution to this equation allows us to study the formulated problem (1)–(3). The methods for solving the integral equations in form (5) are presented in [3].

ALGORITHM FOR SOLVING PROBLEM (1)–(3)

We apply a difference scheme of the following form in the variable t to the system of equations (1)–(3) (see [3]):

$$\frac{\partial T}{\partial t} = \frac{T_k - T_{k-1}}{h}. \tag{6}$$

Here, h is the partition step for the time interval $[0, \tau]$; T_i, T_{i-1} are the magnitudes of the temperature field at the ith and $(i-1)$th time steps, respectively, $i = 1, 2, \ldots, p$; and the initial approximation for $i = 1$ is equal to T_0. Then, at each ith step of the t-variable variation, we have p time-independent nonlinear boundary value problems:

$$k\nabla^2 T_i(x) - \frac{c}{h}T_i(x) + \bar{q}(x) = \frac{c}{h}T_{i-1}(x), \quad x \in (x_1, x_2, x_3), \tag{7}$$

$$\frac{\partial T_i}{\partial n} = 0 \quad \text{at the } S. \tag{8}$$

Problem (7), (8) is linearized by the iteration method [4]. Assuming the value $T_i = 0$ to be the initial approximation for $s = 1$, we arrive at elliptic linear boundary value problems for the $(s+1)$th iteration at each time layer:

$$k\nabla^2 T_i^{(s+1)}(x) - \frac{c}{h}T_i^{(s+1)}(x) + \bar{q}(x) = \frac{c}{h}T_{i-1}^{(s+1)}(x), \quad x \in (x_1, x_2, x_3), \tag{9}$$

$$\frac{\partial T_i^{(s+1)}}{\partial n} = 0 \quad \text{at the } S. \tag{10}$$

We represent the solution to problem (9), (10) for each time layer and for every linearization step using the R-function method [2]:

$$T_i^{(s+1)} = P_0(x) - \omega D_1 P_0(x) + \omega^2 P_1(x), \tag{11}$$

where $P_0(x)$, $P_1(x)$ are indeterminate components of the form

$$P_0(x) = \sum_{k=1}^{N} c_k \varphi_k(x), \quad P_1(x) = \sum_{k=1}^{M} F_k \psi_k(x).$$

Here, $\varphi_k(x)$, $\psi_k(x)$ are approximating functions for which classical polynomials, polynomials with local supports, or special functions can be chosen; $\omega(x)$ is the function describing the boundary S of the region; D_1 is a differential operator of a special form; and c_k are unknown coefficients determined by a numerical method. Expression (11) exactly satisfies boundary condition (10) without restrictions of generality for the geometry of the region, since it provides a unified analytic equation for the boundary S. The source functions q are determined by solving an integral equation [5] of the form

$$q_i - q_u = \int_S q_i(P)\chi(P, P')dS' - r(P)\int_S q_u(p)\chi(P, P')dS' = (1 - r(P))\int_S q_i(P)\chi(P, P')dS' - \varepsilon\sigma T^4, \tag{12}$$

where P, P' are arbitrary points on the surface S; q_u is the solution to Eq. (5) on the surface S' (internal with respect to S), in which surface heat sources are concentrated; and $dn = dS'$ is the thickness of the surface layer. Let $V_m(x)$ be an orthonormal system of functions of a closed set determined at system surface S. We also assume that the source-determining functions from (5) and (11) can be represented in the form of the series

$$F(x) = \sum_M f_M V_M(x), \quad q_u(x) = \sum_M q_M V_M(x), \quad r(x) = \sum_M r_M V_M(x), \quad \varepsilon(x) = \sum_M \varepsilon_M V_M(x). \tag{13}$$

The coefficients in relations (13) are determined by the Fourier method. Unlike [1], we represent the geometry factor $\chi(x)$ not in series form, but by a unified analytic expression employing function $\omega(x)$ and using the R-function theory [2]. This allows us to consider the temperature fields for regions of virtually arbitrary shape. Substituting the expansion coefficients from (13) into (5), we have

$$\sum_M q_M V_M = \sum_M f_M V_M + \omega(x)\sum_{P,Q} q_P r_Q V_P V_Q. \tag{14}$$

We express f_i in terms of the values of $T(x)$ in the form of a series:

$$f_i = \sigma\sum_{MN} \varepsilon_M T_i^4 \lambda_{MN}. \tag{15}$$

Upon rearrangement, we obtain a system of linear algebraic equations from which unknown values of q_l are found:

$$f_M = \sum_l \alpha_{lM} q_l, \tag{16}$$

where

$$\alpha_{lM} = \delta_{lM} - \omega(x) \sum_{P,Q} r_P \lambda_{PQ}, \quad \lambda_{PQ} = \int_S V_P V_Q dS,$$

and δ_{lM} is the Kronecker delta.

NUMERICAL EXAMPLE

We now consider the boundary value problem

$$c\frac{\partial T}{\partial t} = K\Delta T + \bar{q}^* + \frac{\omega(x)}{s}\left[\varepsilon_1 \int_S q_u dS' - (\varepsilon_1 + \varepsilon_2)\sigma T^4\right], \tag{17}$$

$$T(x, t) = T_0(x), \quad t = 0, \tag{18}$$

$$\left.\frac{\partial T}{\partial \nu}\right|_S = 0. \tag{19}$$

Here, S is the boundary of the region Ω consisting of internal S_1 and external S_2 surfaces. Infinitely long cylinders with quadratic (Fig. 1) and hexagonal (Fig. 2) cross sections were considered in the study. In Eqs. (17)–(19), s is the thickness of the surface layer containing heat sources, ε_1 and ε_2 are the radiation capacities for internal and external boundaries, and the function $\bar{q}^*$ includes heat sources. We introduce the following dimensionless variables: $\xi = \frac{x_1}{2L}$, $\zeta = \frac{x_2}{2L}$ are the dimensionless abscissa and ordinate, respectively; L is the geometric parameter for the region Ω; $\theta = \frac{T}{T^*}$ is the dimensionless temperature (T^* is the reference temperature); $\varsigma = \frac{t}{t^*}$ is the dimensionless time (i.e. time normalized to time $t^* = \frac{4L^2 c}{K}$); $\bar{\varphi}^* = \frac{\bar{q}}{q^*}$ are the dimensionless heat sources with respect to the reference source $q^* = \frac{KT^*}{4L^2}$; $\varphi_u = \frac{q_u}{\sigma T^{*4}}$ is the dimensionless outgoing heat flow; $\eta_1 = \varepsilon_1 \frac{4\sigma T^{*3} L^2}{Ks}$ and $\eta_2 = \varepsilon_2 \frac{4\sigma T^{*3} L^2}{Ks}$ are, respectively, the coefficients of internal and external heat exchange through radiation at the reference temperature T^*; and, finally, $\varepsilon_1 \frac{4\sigma T^{*4}}{s}$ and

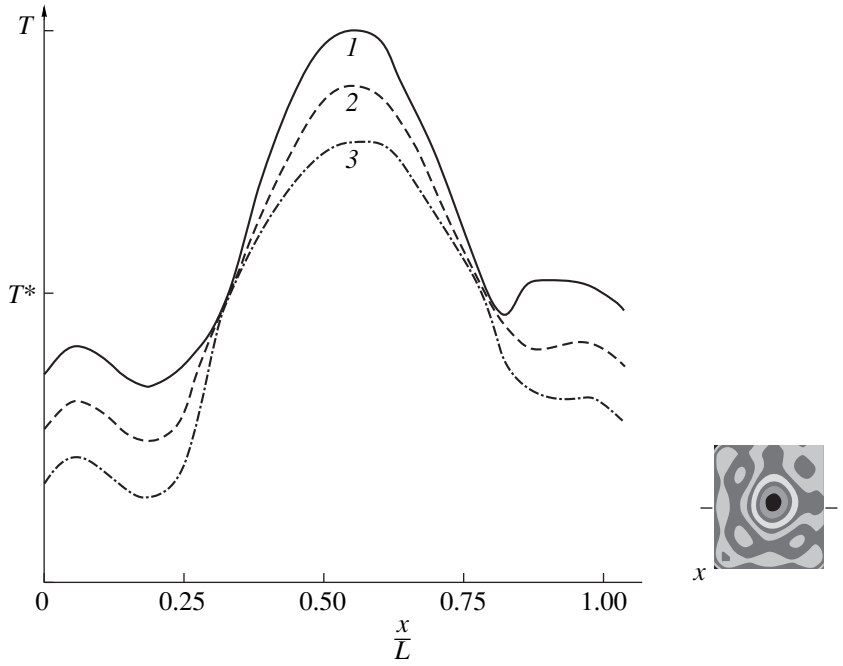

Fig. 1. Temperature-field distribution in the section $x_2 = 0$ for a rectangular region.

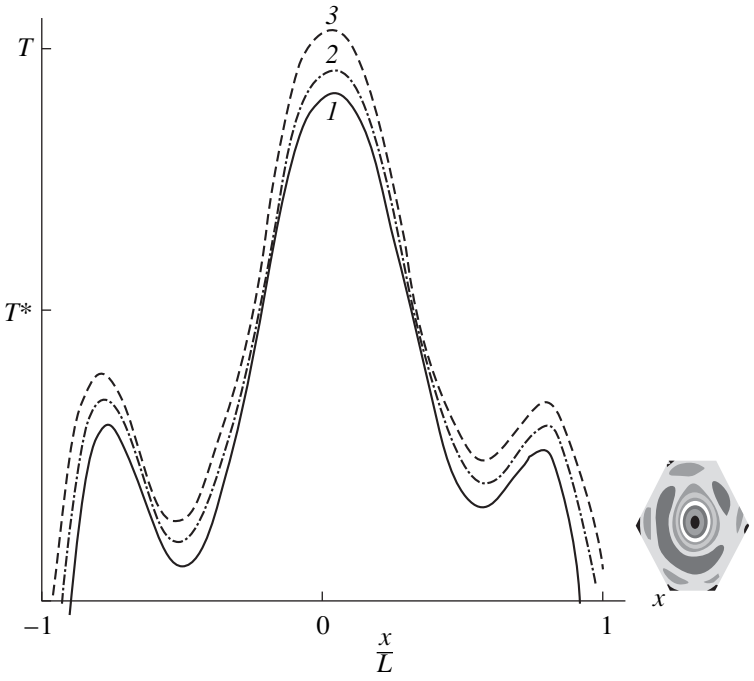

Fig. 2. Temperature-field distribution in the section $x_2 = 0$ for a hexagon.

ε_2 are the three-dimensional heat sources corresponding to the outgoing-radiation flow from the internal and external boundaries of the body, respectively. In terms of dimensionless variables, system of Eqs. (17)–(19) takes the form

$$c\frac{\partial\theta}{\partial\varsigma} = K\Delta\theta + \bar{\varphi}^* + \eta_1\omega(x)\left[\varepsilon_1\int_S \varphi_u dS' - \theta^4\right] - \eta_2\theta^4, \tag{20}$$

$$\theta = \theta_0, \quad \varsigma = 0, \tag{21}$$

$$\left.\frac{\partial\theta}{\partial\nu}\right|_S = 0. \tag{22}$$

Let $\theta(\varsigma, x) = U(x)T(\varsigma)$. We define the orthonormal system of functions V_n as a solution to the problem of determining the eigenvalues $\bar{\omega}^2$ and eigenfunctions U for the other problem:

$$\nabla^2 U + \bar{\omega}^2 U = 0, \quad \left.\frac{\partial U}{\partial\nu}\right|_S = 0. \tag{23}$$

According to [2], the structure of the solution to problem (23) is represented by expression (11) in the form

$$U = \Phi_1 - \omega D_1\Phi_1, \tag{24}$$

where $\Phi_1 = \sum_n^N C_n V_n$ and the coefficients C_i are found from the minimum condition for the functional [6] which corresponds to boundary value problem (23). Equation (20) will be written as a nonlinear differential equation of the first order:

$$\frac{dT_n}{dt} + \sum_h \gamma_{nh}T_h = \beta, \tag{25}$$

with the initial condition

$$T_n(0) = T_n^{(0)}, \quad t = 0, \tag{26}$$

where the coefficients γ_{nh} and β contain physical parameters of the problem and nonlinear relations for the source functions at the internal and external sides of the boundary S. While linearizing Eq. (25), we choose the initial condition as the first approximation. Numerical analysis revealed the number of iterations for problem (25), (26) to be 10 to 12, depending on the geometric shape and parameters of the object; the number of eigenvalues in relation (24) was equal to 6. As the convergence criterion for the solutions to problem (25), (26), the inequality

$$|T_i - T_{i-1}| \le \varepsilon \tag{27}$$

was used, where ε is the given accuracy value. The following physical parameters of the problem were chosen: radiation capacity $\varepsilon_1 = 0.3, 0.6, 0.9$; $T^* = 300$ K; $\eta_2 = 70$; $\eta_1 = 30, 60, 90$. Figures 1 and 2 show temperature distributions in cross section $x_2 = 0$ for rectangular

and hexagonal regions in the case of $\eta_2 = 70$, $\eta_1 = 30$, 60, 90 (curves *1*, *2*, and *3*, respectively).

The reliability of the results was confirmed by comparing them with those of [1] in the case of a rectangular region in one of the cross sections. Note that the coincidence is observed in the central part of the section. At its ends, there are oscillations explained, apparently, by the nature of the approximation method (trigonometric polynomials) used in the numerical analysis. The wave character of the temperature-field distribution at the section ends in Fig. 2 is caused by the presence of corner points in the hexagonal region.

Thus, in this paper, the application of the R-function method to the investigation of radiation processes for complex-shaped bodies is proposed. The examples of numerical analysis presented show the efficiency of this new approach.

REFERENCES

1. K. Arduini, S. Sgubini, and C. Uliviei, Acta Astronaut. **8**, 749 (1981).
2. V. L. Rvachev, *Theory of R-functions and Its Certain Applications* (Naukova Dumka, Kiev, 1982).
3. A. A. Samarskiĭ, *Introduction to Numerical Methods* (Nauka, Moscow, 1977).
4. A. A. Berezovskiĭ, *Nonlinear Boundary Value Problems of Heat-Radiating Bodies* (Naukova Dumka, Kiev, 1968).
5. L. V. Kantorovich and V. I. Krylov, *Approximate Methods of Higher Analysis* (Nauka, Moscow, 1977; Wiley, New York, 1964).
6. S. G. Mikhlin, *Variational Methods in Mathematical Physics* (Nauka, Moscow, 1970; Pergamon, Oxford, 1964).

Translated by V. Tsarev

Doklady Physics, Vol. 46, No. 1, 2001, pp. 26–29. Translated from Doklady Akademii Nauk, Vol. 376, No. 3, 2001, pp. 324–327.

TECHNICAL PHYSICS

Size-Dependent Dispersion Hardening: Effect of a Medium

G. G. Kochegarov

Presented by Academician F.A. Kuznetsov April 24, 2000

Received May 10, 2000

The changes in mechanical properties of solids during their adsorption interaction with molecules of a medium (the so-called Rehbinder effect) are observed practically irrespective of the choice of materials and the type of mechanical action on them (metals, solids with covalent, ionic, and molecular bonds, and polymers) [1].

The dispersion of solids depends mainly on two phenomena proceeding during the fracture of materials: an increase in the area of the interphase surfaces and distortion of the crystalline structure (especially on fractured surfaces) caused by plastic deformation under external loading [2]. In an ideal crystal, stable cracks cannot form, because microcrack stabilization is provided by plastic deformation [3]. This type of deformation is developed in front of the crack tip in a narrow region whose parameters are determined by the nature of the solid, the state of its lattice, the conditions of fracturing, and the character of the interaction between the solid and the ambient medium [2].

The dispersion of a solid is accompanied by surface destruction caused by the development of plastic deformations in the region of stress localization on the structural defects (observed even for such brittle material as quartz) [2]. As a result, the surfaces of the dispersed particles are amorphized and a spectrum of the defects is formed (i.e., violation of the long-range order of the material caused by irreversible deformation occurs). This is accompanied by a break of the chemical bonds and their disordered closure, changes in the valence angles and coordination numbers of the atoms, transition of these atoms into nonequilibrium states, fractionation of the coherent-scattering regions (D), and an increase in microdistortions η and coherent-scattering misorientation angle, etc., which, in turn, causes changes in the mechanical properties of the material [4].

Two-hour dispersion of quartz in a planetary mill with agate-lined drums and agate balls caused the formation of specific surfaces in quartz powders dispersed in water and in air equal to 28 and 6.6 $m^2\ g^{-1}$, respectively. The microdistortions and dimensions of the coherent-scattering regions were measured along the $\langle 101 \rangle$ and $\langle 202 \rangle$ crystallographic directions with an accuracy of ±10%. The Fourier coefficients were computed using modified codes. The methods of powder dispersion and determination of the parameters of the substructures in various minerals are described in detail in [5–7].

The adsorption-active media used in the dispersion of solids change the mechanical properties of these solids [6, 8]. The thickness of the amorphized layer of quartz particles dispersed in ambient air exceeds (by an order of magnitude and even more) the thickness of the amorphized layer formed by quartz dispersion in an adsorption-active medium [4–9]. Indeed, as is seen from Fig. 1, the amorphized-layer of quartz particles dispersed in a 5%-hydrofluoric-acid solution is dissolved and attains a plateau level with the parameters of the initial-material substructure (D = 220 nm, $\eta = 4.5 \times 10^{-6}$)

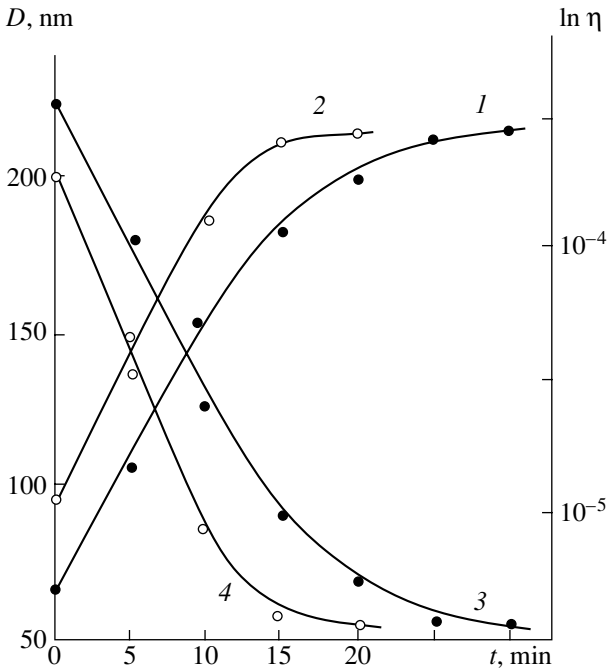

Fig. 1. Kinetics of the parameters of (*1*, *2*) coherent-scattering region D and (*3*, *4*) microdistortions η during dissolution of quartz dispersed (*1*, *3*) in air and (*2*, *4*) in water.

Joint Institute of Geology, Geophysics, and Mineralogy, Siberian Division, Russian Academy of Sciences, Novosibirsk, 630090 Russia

1028-3358/01/4601-0026$21.00

within a shorter period of time (curves *2*, *4*) than air-dispersed quartz (curves *1*, *3*). This indicates that plastic deformation under quartz dispersion occurs mainly during material fracture in the surface layers on the sites of highest stress concentration (crack tips), whose values, according to the theory of elasticity, rapidly decrease in the region of shear localization. Dissolution of the amorphized layer reveals that the particles have crystalline cores. A decrease in the thickness of the amorphized layer of water-dispersed particles was also observed for other minerals [2]. This is consistent with the fact that the thickness of the amorphized layer of water-dispersed quartz is constant and equals $h \approx 2$ nm within a wide dispersion range, whereas in air-dispersed quartz, this thickness attains a value of $h \approx$ 15 nm and even higher values [9].

The size-dependent dispersion hardening, i.e., the increase in specific energy necessary for fracture with a decrease of the linear dimension d of the particles (evaluated from the formation of a plateau on dispersion-kinetics curves), was considered in detail in [9]. It was indicated there that explaining size-dependent dispersion hardening in terms of the lower probability of finding a "dangerous" crack in a particle with a decrease in its dimension is not quite adequate. Indeed, during dispersion, each particle is repeatedly subjected to almost critical stresses, giving rise to the formation and development of new defects which make considerable change in the density of these defects unlikely. Thus, the mechanism of size-dependent dispersion hardening remains unclear. Well-known experimental data on the strength of glass balls of various diameters were represented in the coordinates of a theoretically derived equation for particle strength P. It was shown that ball strength increased with a decrease in particle diameter and approached a constant value at a diameter equal to ~40 μm [9] (Fig. 2, curve *1*). However, numerous publications show that material strength can also increase with a decrease in specimen diameter in considerably smaller dimensions (several microns) [10]. This makes it necessary to analyze the mechanism of size-dependent dispersion hardening and the effect of adsorption-active medium on this mechanism with due regard for the recent data on the nature of fracture in solids [2].

Modern concepts on the changes in defect structure of solids due to plastic deformation indicate that the evolution of defects with an increase in their density is accompanied by specific collective effects, such that it becomes possible to establish the coherent relation between the components of the defect spectrum and the formation of the structural elements of a higher level [11]. Thus, upon attainment of the critical density of dislocations, they form small-angle walls, which, in turn, decrease the energy of the dislocation structure. Dislocation walls provide fractionation of the initial coherent-scattering regions, with the D value corresponding to the spacing between the dislocation walls [12].

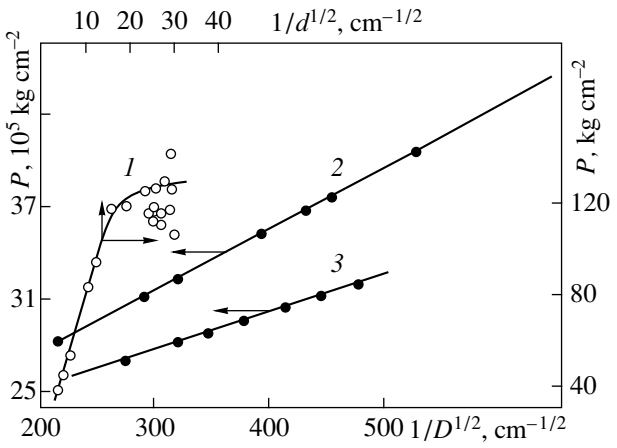

Fig. 2. Increase in the strength (*1*) of glass balls (according to [9]) and quartz particles dispersed (*2*) in air and (*3*) in water with a decrease in their diameter in the coordinates of Eq. (4).

Plastic deformation occurring at the tip of a propagating crack provides material hardening along the crack sides because of a higher dislocation density in the region of plastic-shear localization. We believe that this process leads to an increase in particle strength [4]. Dislocation pileups in the glide plane can be considered as a large effective dislocation with Burgers vector nb (where n is the number of dislocations in the region of shear decelerated by an obstacle and b is the unit Burgers vector). Then, the total elastic stress field becomes n-fold more intense than the field formed of a single dislocation. Therefore, the dislocation pileup is characterized by large crystal regions (with high stress concentrations) in which microcracks can become open [8], whereas the considerable stresses around dislocation pileups determine the character of strain hardening, because they strongly affect the dislocation motion in the neighboring glide planes [13]. Material hardening with an increase in plastic strain caused by a higher dislocation density is described by the equation of shear stress $\tau = \frac{Ga}{2D}$ [14], where G is the shear modulus and a is the interatomic distance along the shear direction. According to this equation, τ is inversely proportional to the linear dimension of the coherent-scattering region.

The effect of an adsorption-active medium on shear in a solid can be estimated from the following consideration. Dislocation nucleation results in relaxation of the elastic energy in the region of shear localization. The shear equal to the magnitude of the Burgers vector b proceeds along the circumference $2\pi r$ of radius r, which, in turn, gives rise to elastic strain $\frac{b}{2\pi r}$ and stress $\frac{Gb}{2\pi r}$, which can be evaluated from the Hooke's law

valid for small shear deformations $\frac{Gb}{2\pi r}$. For a three-dimensional problem, the dislocation energy at the average stress value is determined as

$$\int_V \frac{Gb^2}{8\pi^2} dV = \frac{Gb^2}{8\pi^2} \int_0^l \int_r^R \frac{dS}{r^2} = \frac{Gb^2 l}{4\pi} \ln \frac{R}{r}, \quad (1)$$

where l is the dislocation length, R is the radius of the outer boundary of the ring ($R \approx 10^4 b$ is the average spacing between dislocations), and $r \approx b$ (determined by the applicability limit of the elasticity theory).

Nucleation of dislocations is associated with formation of a cavity with surface energy σ. It is assumed that a dislocation has a cylindrical shape. The energy of the cavity formation equals $2\pi r l \sigma$, whereas the energy of stress relaxation during the cavity formation is determined by Eq. (1). Therefore, the total change in energy during crack nucleation equals

$$\Delta W = 2\pi r l \sigma + \frac{Gb^2 l}{4\pi} \ln \frac{R}{r}$$

and is minimal at the equilibrium dislocation cavity $\frac{\partial(\Delta W)}{\partial r} = 0$ and $2\pi l \sigma - \frac{Gb^2 l}{4\pi r} = 0$, whence the equilibrium radius is

$$r = \frac{Gb^2}{8\pi^2 \sigma}. \quad (2)$$

A Franck–Read source starts generating dislocations under the effect of an applied stress at the moment when shear stress satisfies the condition $\tau = \frac{Gb}{l}$, where l is the length of an element which is a source of dislocations [13]. Substituting into this formula the value of b from (2), we see that the shear stress is proportional to $\sigma^{1/2}$ ($\tau \sim \sigma^{1/2}$). In other words, in an adsorption-active medium, dislocations are generated under lower stresses than in inert media. At the same time, the plastic deformation proceeds more intensely because of the reduced level of stresses necessary for attaining the critical dislocation concentration ($n = 10^2$–10^3 [8]) in the region of the damped shear.

Considering the criterion of microcrack nucleation during quartz amorphization, we managed to derive formulas relating the critical crack dimension l_c and the shear stress [9]: $l_c = \frac{\tau^2 \lambda^2 f}{2\sigma G}$ and $\tau^2 = \frac{2\sigma G l_c}{\lambda^2 f}$ (where λ is the region of incomplete-shear localization and f is the numerical coefficient on the order of 1.5).

According to [8], the size of the shear-localization region is maximal if it spreads over the entire cross section of a single crystal (or all the grains of a polycrystal); i.e., $\lambda_{max} = L$, where L is the diameter of a single crystal or a grain. This conclusion is consistent with experimental data. In our case, we can assume that λ_{max} is equal to D, i.e., to the size of the coherent-scattering region (a fragment of the particle substructure). Then, $\tau^2 = \frac{2\sigma G l}{f D^2}$, which is similar to the above relationship for τ from [14], and

$$l_c = \frac{\tau^2 D^2 f}{2\sigma G}. \quad (3)$$

Proceeding from the Griffith criterion for strength of a solid with a nucleated crack, $P = \alpha \sqrt{\frac{E\sigma}{l_c}}$ (where the coefficient α is close to unity and E is Young's modulus) [15], and formula (3) (obtained for the length l_c of the nucleated crack) and assuming that $P \approx \tau$ and $E \approx G$, we obtain $P\tau = \frac{\kappa_1 G \sigma}{D}$. Thus, the strength of small particles is determined as $P = \kappa \sqrt{\frac{\sigma G}{D}}$ (where $\kappa = \sqrt[4]{\frac{2\alpha}{f\varphi}}$ is close to unity and φ is the coefficient taking into account the slope of the plane of maximum stresses to the direction of the applied force [9]). With due regard for the formula describing the strength P_0 of bulky particles, we obtain a relationship taking into account the effect of particle size on particle strength (via the parameter D) and the surface energy:

$$P = P_0 + \sqrt{\frac{\sigma G}{D}}. \quad (4)$$

Strictly speaking, the Griffith criterion is applicable only to materials with perfect brittleness, but, as a microcrack is nucleated in the region of incomplete shear, this criterion should also be applicable to materials which undergo plastic shear prior to fracture [8].

The above estimate by Eq. (4) for strength of dispersed quartz particles, which is based on the analysis of saturation attained by the experimental kinetic curves $D(t)$ for an average-size particle, is shown in Fig. 2 (curves *2*, *3*). This estimate shows that hardening also occurs for particles with linear dimensions of 0.65 μm (dispersion in air, curve *2*) and 0.15 μm (dispersion in water, curve *3*), which is consistent with the kinetics of quartz dispersion and shows that particle hardening becomes noticeable when the kinetic curve attains its plateau at diameter $d \approx 2$ μm (dispersion in water) and $d \approx 6$ μm (dispersion in air). The above mechanism of size-dependent hardening allows us to estimate the parameter of the most hardened particles from the experimental data for the hardened amorphized layer $d = 2h$ (where h is the thickness of the amorphized layer) [9], which is equal to $d_a \approx 30$–40 nm for dispersion in air and $d_w \approx 4$ nm for dispersion in water.

According to (4), reduction of the surface energy σ of a solid in an adsorption-active medium decelerates the process of dispersion hardening, because the thickness of the amorphized layer of the particles is less than the reduction of the surface energy during dispersion in air. It is seen from Fig. 2 that both absolute hardening and the rate of its increase for water-dispersed quartz particles are lower than the corresponding values for air-dispersed quartz particles, which is seen from the kinetics of the material dispersion. Dispersion in an adsorption-active medium is more efficient than in air.

Thus, size-dependent dispersion hardening is caused by hardening of the surface layer of particles due to plastic deformation of the material at the tip of a propagating crack, which plays the role of a strong stress concentrator. Upon attainment of the linear particle dimension $d \gg h$ during dispersion of solids, the crack starts propagating mainly in the unhardened region of the particle (i.e., in its crystalline core). If d becomes comparable to h, the contribution of the hardened layer to the mechanical properties of the particles becomes noticeable and the specific energy necessary for change of the mechanical properties increases. In the limiting case $d = 2h$, particle strength becomes maximal. The degree of particle hardness can be estimated from parameter D, which describes the dimensions of the coherent-scattering region. The thicknesses of the amorphized layer of the particles during material dispersion in air, h_a, and in an adsorption-active medium, h_m, are different (usually, $h_a \gg h_m$), and the maximum dimensions of most hardened particles are also different, $d_a \gg d_m$.

The above mechanism of size-dependent dispersion hardening is consistent with the concepts of possible material hardening by two different methods: by designing defect-free materials and by plastic deformation of materials. Bulky materials used in technology are hardened mainly using the second method.

ACKNOWLEDGMENTS

The author is grateful to E.G. Shchukin for discussions on the possible plastic deformation of brittle solids (in particular, quartz) during fracture and the effect of adsorption-active media on this process.

REFERENCES

1. P. A. Rehbinder and E. D. Shchukin, Prog. Surf. Sci. **3** (2), 97 (1972).
2. G. G. Kochegarov, Izv. Sib. Otd. Akad. Nauk SSSR, Ser. Khim. Nauk, Issue 1, No. 2, 65 (1986).
3. Yu. M. Plishkin, Prikl. Mekh. Tekh. Fiz., No. 2, 95 (1962).
4. G. G. Kochegarov, Izv. Akad. Nauk SSSR, Neorg. Mater. **24**, 73 (1988).
5. G. G. Kochegarov, L. P. Pantyukova, and T. S. Yusupov, Izv. Sib. Otd. Akad. Nauk SSSR, Ser. Khim. Nauk, Issue 3, No. 7, 67 (1979).
6. G. G. Kochegarov, Kolloidn. Zh. **43**, 29 (1981).
7. G. G. Kochegarov, Izv. Sib. Otd. Akad. Nauk SSSR, Ser. Khim. Nauk, Issue 5, No. 12, 65 (1978).
8. V. I. Likhtman, E. D. Shchukin, and P. A. Rehbinder, *Physicochemical Mechanics of Metals* (Akad. Nauk SSSR, Moscow, 1962).
9. G. S. Khodakov, *Physics of Grinding* (Nauka, Moscow, 1972).
10. G. M. Bartenev, *Mechanical Properties and Heat Treatment of Glass* (Gosstroĭizdat, Moscow, 1960).
11. *Physical Mesomechanics and Computer Designing of Materials*, Ed. by V. E. Panin, V. E. Egorushkin, P. V. Makarov, *et al.* (Nauka, Novosibirsk, 1995), Vol. 1.
12. M. A. Krivoglaz, *Diffraction of X-rays and Neutrons by Fluctuation Nonuniformities in Nonideal Crystals* (Naukova Dumka, Kiev, 1983).
13. A. H. Cottrell, *Theoretical Structural Metallurgy* (Arnold, London, 1955; GNTI, Moscow, 1961).
14. O. V. Bogorodskiĭ and Ya. S. Umanskiĭ, Izv. Akad. Nauk SSSR, Ser. Fiz. **20**, 614 (1956).
15. A. A. Griffith, Philos. Trans. R. Soc. London, Ser. A **221**, 163 (1920).

Translated by L. Man

Doklady Physics, Vol. 46, No. 1, 2001, pp. 30–33. Translated from Doklady Akademii Nauk, Vol. 376, No. 2, 2001, pp. 191–194.

ENERGETICS

Heat Exchange in the Vicinity of a Critical Point

Academician I. I. Novikov

Received July 31, 2000

A critical point (CP) corresponds to singularities in properties of a substance and, therefore, to values specifying similarity criteria for heat and mass transfer, which substantially affects the character and intensity of heat and mass exchange in a critical region. The most general approach to studying the critical state was developed by J. Gibbs [1], who formulated basic equations for a CP. Unfortunately, these equations turned out to be little-known, so that this paper is likely to be one of the first attempts to describe the critical state and, in particular, the special features of the processes of heat and mass transfer in this state on the basis of Gibbs equations.

In the case of a simple single-component substance, for example, a pure liquid or gas, the Gibbs equations for a CP are of the form

$$D = \begin{vmatrix} E_{SS} & E_{SV} \\ E_{VS} & E_{VV} \end{vmatrix} = 0, \quad \begin{vmatrix} E_{SS} & E_{SV} \\ D_S & D_V \end{vmatrix} = 0. \qquad (1)$$

Here, $E(S, V)$ is the internal energy, S is entropy, and V is volume; the subscripts denote corresponding partial derivatives.

The first equation of set (1) determines a spinodal for each of the phases (i.e., according to Gibbs, the stability boundary at which $\left(\frac{\partial p}{\partial V}\right)_T = 0$); the second equation relates directly to a CP. Following L. Landau (see [2], Sect. 152), we consider the quadratic form $E_{SS}\delta S^2 + 2E_{SV}\delta S\delta V + E_{VV}\delta V^2$ (this form is also the second variation $\delta_2 E$) at the CP. According to the Landau assumption, $\delta_2 E = 0$ at the CP, which is valid because it follows directly from Eqs. (1). Indeed, upon differentiating the first equation and opening the second one, we obtain

$$D_V + D_S\frac{dS}{dV} = 0, \quad D_V E_{SS} - D_S E_{SV} = 0.$$

From here, it follows that $\frac{dS}{dV} = -\frac{E_{SV}}{E_{SS}}$ $\left[\text{with } \frac{E_{SV}}{E_{SS}} = -\left(\frac{\partial p}{\partial T}\right)_S = -\left(\frac{\partial p}{\partial T}\right)_V\right]$ and, correspondingly, $\delta S = -\frac{E_{SV}}{E_{SS}}\delta V$. Substituting this into $\delta_2 E$, we find that at the CP,

$$\delta_2 E = 0. \qquad (2)$$

At all other points, $\delta_2 E \neq 0$ and, as can be seen from the well-known equilibrium stability condition,

$$\frac{1}{2}[E_{SS}\delta S^2 + 2E_{SV}\delta S\delta V + E_{VV}\delta V^2]$$
$$+ \text{higher-order terms} > 0. \qquad (3)$$

Here, $\delta_2 E$ is positive [the higher-order terms in (3) can be denoted as $\delta_3 E/3!$, $\delta_4 E/4!$, etc.].

The CP parameters (p_{cr}, T_{cr}, V_{cr}) are determined unambiguously by the two equations in (1) and the equation of state; i.e., the CP is unique. Only at this point, $\delta_2 E = 0$, while the magnitude of the derivative $\frac{dS}{dV}$ at the spinodal is equal to $\left(\frac{\partial p}{\partial T}\right)_V = \frac{dp}{dT}$ at the CP, i.e., coincides with the value of $\frac{dS}{dV}$ at the phase-equilibrium line. This implies that the spinodals of both phases and the line of equilibrium have a common tangent at this point, while the equation of the spinodal is similar, in particular, to the equation for $V - V_{cr}$ at the phase-equilibrium line.

It is important to establish the character of Eq. (2), i.e., to clarify whether this equation is a simple equality or an identity. According to the quadratic-form theory, a nonnegative quadratic form of two variables is characterized by a single zero eigenvalue of the square matrix composed of quadratic-form elements. The eigenvalues are calculated according to the characteristic equation, which has the following form with allowance for the first equation of set (1):

$$\lambda^2 - \lambda(E_{SS} + E_{VV}) = 0.$$

(Here, E_{SS}, E_{SV}, and E_{VV} are reduced to the dimension-

Baikov Institute of Metallurgy and Materials Research, Russian Academy of Sciences, Leninskiĭ pr. 49, Moscow, 117333 Russia

1028-3358/01/4601-0030$21.00

less form). The solution to this equation is

$$\lambda_1 = 0, \quad \lambda_2 = E_{SS} + E_{VV}.$$

The equality $\lambda_1 = 0$ implies that one of the eigenvalues is zero at the spinodal of each phase. The quadratic form is zero in such a state, when, in addition to the first eigenvalue, the second one is also zero, i.e., when $\lambda_1 = 0$ and $\lambda_2 = 0$. However, if all the eigenvalues (in this case two of them) are zero, the quadratic form vanishes identically (this is also seen from the equality $\lambda_2 = 0$; i.e., $E_{SS} + E_{VV} = 0$, which is zero only for $E_{SS} = 0$ and $E_{VV} = 0$ due to the positiveness of E_{SS} and E_{VV}). It follows from this fact that the equality $\delta_2 E = 0$ is identically fulfilled at the CP (which, as was already noted, is unique); i.e., $\delta_2 E \equiv 0$. Thus, at the critical point, all the eigenvalues and all the coefficients in the quadratic form vanish; i.e., it degenerates. However, in this case according to (3), it must also be that $\delta_3 E = 0$ and $\delta_4 E > 0$ for the stability of the critical state:

$$\delta_2 E \equiv 0, \quad \delta_3 E = 0, \quad \delta_4 E > 0. \tag{4}$$

These are the most general characteristic conditions determining the CP. From the equalities $E_{SS} = 0$ and $E_{VV} = 0$ at the CP (where $E_{SS} = \frac{C_V}{T}$, and $\sqrt{E_{VV}^{1/2}} = a$ is the sound velocity), it follows

$$C_V \longrightarrow \infty, \quad a = 0. \tag{5}$$

Fundamental results (4) and (5) are the direct consequence of Gibbs equations (1) and are entirely corroborated by recent precise experiments.

Furthermore, it follows from (4) that $T = \frac{\partial E}{\partial S}$ and $p = -\frac{\partial E}{\partial V}$ are expressed either by the term T_{cr} or p_{cr} and by the sum of products $(V - V_{cr})$ and $(S - S_{cr})$ of the third degree and higher. Owing to this, at the phase-equilibrium line, where S can be considered as a function having the form $S = S_{cr} + \frac{\partial S}{\partial V_{cr}}(V - V_{cr})$ in the vicinity of the CP, we can write out

$$T_{cr} - T \sim (V - V_{cr})^3; \quad p_{cr} - p \sim (V - V_{cr})^3.$$

At the CP, the derivative is $\frac{dp}{dT} = \left(\frac{\partial p}{\partial T}\right)_V$; therefore, $\frac{(\partial p/\partial V)_T}{dT/dV} = 0$. Since $\frac{dT}{dV} \sim (V - V_{cr})^2$, $\left(\frac{\partial p}{\partial V}\right)_T$ cannot be a degree of $V - V_{cr}$ lower than three, but for retaining the sign "minus" everywhere, $\left(\frac{\partial p}{\partial V}\right)_T$ must be expressed by an even degree of $V - V_{cr}$. Consequently, at the critical isobar, the CP corresponds to the derivative $\left(\frac{\partial p}{\partial V}\right)_T \sim (V - V_{cr})^4$ with $T_{cr} - T \sim (V - V_{cr})^3$. Using these values, it is possible to determine the heat capacity C_p. According to the thermodynamic relation, $\left(\frac{\partial C_p}{\partial p}\right)_T = -T\left(\frac{\partial^2 V}{\partial T^2}\right)_p$. We multiply both sides by $\left(\frac{\partial p}{\partial V}\right)_T$ equal to $(T_{cr} - T)^{4/3}$, as was shown above. In this case, the left-hand side is $\left(\frac{\partial C_p}{\partial V}\right)_T$; the right-hand side is proportional to $(T_{cr} - T)^{1/3}$ with allowance for $\left(\frac{\partial^2 V}{\partial T^2}\right)_p \sim (T_{cr} - T)^{1/3 - 2}$ and $\left(\frac{\partial p}{\partial V}\right)_T \sim (T_{cr} - T)^{4/3}$. Thus, $\left(\frac{\partial C_p}{\partial V}\right)_T \sim (T_{cr} - T)^{-1/3} \sim \frac{1}{V - V_{cr}}$; i.e., $C_p = a\ln(V - V_{cr}) + f(T)$. Replacing $V - V_{cr}$ by $(T_{cr} - T)^{1/3}$, we find that the singular component C_p varies in the critical isobar as

$$C \sim \ln|T_{cr} - T|. \tag{6}$$

It is easy to verify that the difference $C_p - C_V$ equal to $-T\left(\frac{\partial V}{\partial T}\right)^2\left(\frac{\partial p}{\partial V}\right)_T$ has no singularity, so that the singular component of heat capacity C_V varies according to the same law as C_p (for this reason, the subscript "p" for C in (6) is omitted), the values of the singular parts of C_p and C_V being identical at the CP. In a similar manner, C_V varies in the isochore [because the sum of C_V of each phase in the equilibrium line $V(T)$ leads, with an accuracy to a finite-jump, to the doubled value of C_V in the two-phase region for the line $V = V_{cr}$].

With the known expression for C_V, it is easy to determine the velocity of sound; at the critical isobar, it equals

$$a \sim [\ln|T_{cr} - T|]^{-1/2}. \tag{7}$$

We now consider how $\delta_2 E$ changes when passing from the spinodal to the nearby state. Let this passage occur along the isobar; then, $\delta S = S_p - S_s$, $\delta V = V_p - V_s$ and the quantity E_{SS} at the point under consideration attains $E_{SS}^{(s)} + \left(\frac{\partial E_{SS}}{\partial V}\right)^{(s)}(V_p - V_s) + \left(\frac{\partial E_{SS}}{\partial S}\right)^{(s)}(S_p - S_s)$. In the same way, we express E_{SV} and E_{VV} (furthermore, the subscript "p" is omitted). After obvious transformations (with allowance for the equalities $E_{SS}E_{VV} - E_{SV}^2 = 0$ and $\frac{E_{SV}}{E_{SS}} = -\left(\frac{\partial p}{\partial T}\right)_V$ at the spinodal), substituting these values in $\delta_2 E$ and ignoring the higher-order terms, we

obtain $E_{SS}\left[\left(\frac{\partial S}{\partial V}\right)_p - \left(\frac{\partial p}{\partial T}\right)_S^{(s)}\right]^2 \delta V^2$. According to the thermodynamic relation, we have $\left(\frac{\partial S}{\partial V}\right)_p = \left(\frac{\partial p}{\partial T}\right)_S$. On the other hand, $\left(\frac{\partial p}{\partial T}\right)_S = \left(\frac{\partial p}{\partial T}\right)_S^{(s)} + \left(\frac{\partial^2 p}{\partial T^2}\right)_S^{(s)}(T - T_s)$. Since $\left(\frac{\partial S}{\partial V}\right)_p = \left(\frac{\partial p}{\partial T}\right)_V + \left(\frac{\partial S}{\partial V}\right)_V \left(\frac{\partial p}{\partial T}\right)_p$ and the difference $\left(\frac{\partial p}{\partial T}\right)_V - \left(\frac{\partial p}{\partial T}\right)_S^{(s)}$ is small compared to the other term in square brackets, the difference is equal to $C_V \Delta T/T\Delta V$. Correspondingly, the variation $\delta_2 E$ amounts to $\frac{C_V^2}{C_V T}(T - T_s)^2$. In the case of passing along the critical isobar, the variation $\delta_2 E$ is equal to $\left(\frac{C_V}{T}\right)(T - T_{cr})^2$. As is well known, the quantity $\frac{1}{2}\delta_2 E$ determines the minimum work, $L_{min} = \Delta E - T_0 \Delta S + p_0 \Delta V$. Accordingly, the variation $\Delta\Phi$ of the Gibbs energy is expressed in the same manner as the variation $\delta_2 E$; i.e., for the isobaric variation of the state near the spinodal, we have for the specific minimal work

$$\Delta l_{min} \sim (T - T_s)^2. \quad (8)$$

This thermodynamic relation makes it possible to estimate the temperature dependence for each term composing Φ.

The state near the spinodals of each phase and, especially, near the critical point is characterized by the presence of new-phase nuclei in the initial phase. A nucleus of critical size (with a radius r_{crit}) is in the state of unstable equilibrium with respect to the original phase: the minimum work for the formation of such a nucleus satisfies the equation $l_{min} - \sigma \cdot 4\pi r_{crit}^2 = \frac{2\sigma}{r_{crit}}$, where σ is the surface tension. According to the above proportionality of l_{min} and $\Delta\Phi$ to the temperature difference $T - T_s$ squared, we conclude that the right-hand side can be reduced to the form $(T - T_s)^\vartheta (T - T_s)^\nu \sim (T - T_s)^2$, where ϑ and ν are the so-called critical superscripts in the expressions $\sigma \sim (T - T_s)^\vartheta$ and $r_{crit} \sim (T - T_s)^{-\nu}$. In the left-hand side of the original equation, the value $\sigma \times 4\pi r_{crit}^2 \sim (T - T_s)^\vartheta (T - T_s)^{-2\nu}$ represents the contribution to the constant or regular part of the Gibbs energy and is independent of the difference $T - T_s$. Near the CP, the temperatures T_{cr} and T_s virtually coincide, so that from the obtained relationships

$$(T - T_{cr})^\vartheta (T - T_{cr})^\nu \sim (T - T_{cr})^2$$

and $(T - T_{cr})^\vartheta (T - T_{cr})^{-2\nu} \sim (T - T_{cr})^0$,

we find $\vartheta = \frac{4}{3}$ and $\nu = \frac{2}{3}$. As $T \longrightarrow T_{cr}$, the value $r_{crit} \longrightarrow \infty$, which testifies to the scaling invariance for states of a substance in the neighborhood of the CP.

By virtue of the unstable equilibrium, a critical-size nucleus can be considered as a periodically arising density pulsation of the initial phase. It is clear that the wave number $k = \frac{2\pi}{\Lambda}$ is associated with the critical-nucleus radius and that the fundamental wavelength Λ is such that $k = \frac{\pi}{2r_{crit}}$. From this condition, it follows that the fundamental frequency $\omega \sim \frac{1}{\Lambda}$ (i.e., the "soft mode") is proportional to $\frac{1}{r_{crit}}$; i.e., $\omega \sim (T_{cr} - T)^\nu$. In the vicinity of the CP, the quantity $\frac{1}{\omega}$ can serve as a measure of time. On the other hand, the only quantity having a dimension of length is the critical-nucleus size r_{crit}. Based on this fact, we can establish an expression for the thermal diffusivity and viscosity in the vicinity of the CP. Substituting the expressions $\frac{1}{\omega} \sim (T_{cr} - T)^{-\nu}$ instead of time t into the general heat-conductivity equation $\frac{\partial T}{\partial t} = \kappa \Delta T$ and $r_{crit} \sim (T_{cr} - T)^{-\nu}$ instead of the coordinate x_i, we obtain $(T_{cr} - T)^\nu \sim \frac{\kappa}{(T_{cr} - T)^{-2\nu}}$; i.e., $\kappa \sim (T_{cr} - T)^{-\nu}$, where $\nu = \frac{2}{3}$. Thus, the thermal diffusivity increases at the CP to infinity. The same statement is also true for the heat conductivity; with allowance for (6),

$$\lambda \sim (T_{cr} - T)^{-2/3} \ln(T_{cr} - T). \quad (9)$$

The viscous dissipation is determined by the equation

$$\dot{E}_{mekh} = \frac{\eta}{2}\int\left(\frac{\partial w_i}{\partial x_j} + \frac{\partial w_j}{\partial x_i}\right)^2 dV,$$

where $\dot{E}_{mekh}$ is referred to the entire liquid, $\Phi = \frac{\partial \phi}{\partial V}$, and w is the velocity. Bearing in mind that $\dot{E}_{mekh} = \Delta\int \phi\, dV$, we find similarly to the previous case that $(T_{cr} - T)^2 (T_{cr} - T)^\nu \sim \frac{\eta}{(T_{cr} - T)^{-2\nu}}$; i.e., $\eta \sim (T_{cr} - T)^{4/3}$.

Hence, it follows that the shear viscosity has no singular component.

We now estimate the diffusivity D at the CP. As is known, $D = \alpha\rho\frac{\partial\mu}{\partial c}$ (α is the finite kinetic coefficient, μ is the chemical potential, c is the concentration, and ρ is the density). In the critical state of a binary mixture (a solution), $\frac{\partial\mu}{\partial c} = 0$ and, therefore, $D = 0$.

The state of a substance near the CP is sometimes considered to be a gas of liquid droplets. Such a representation is not correct: if it were valid, the heat conductivity and viscosity would be proportional to one another, as this takes place in a low-density gas. In fact, λ and η vary near the CP according to quite different laws; λ tends to infinity, while η remains finite.

Substituting the found values of C_p, a, λ, and η into the expressions corresponding to the criteria expressed via the Reynolds, Prandtl, Grashof, and Mach numbers, we conclude that, in the CP region, the Reynolds number Re conserves a finite value, whereas the Prandtl number Pr tends to zero and the Grashof and Mach numbers Gr and M become infinite:

$$\begin{gathered}\mathrm{Pr} \sim (T_{\mathrm{cr}} - T)^{2/3}, \quad \mathrm{Gr} \sim (T_{\mathrm{cr}} - T)^{-2/3}, \\ \mathrm{Ma} \sim (\ln|T_{\mathrm{cr}} - T|)^{1/2}.\end{gathered} \tag{10}$$

Thus, the heat exchange in the fluid flow near a critical point is characterized by a Prandtl number tending to zero. This implies that the thickness of the thermal boundary layer δ_T is substantially larger than that of the hydrodynamic boundary layer δ:

$$\frac{\delta_T}{\delta} \sim (T_{\mathrm{cr}} - T)^{-1/3}.$$

The free convection at a temperature T of a fluid close to T_{cr} and to that of a solid, which is much lower than T, is characterized by a higher value of the Grashof number and, therefore, is turbulent; in this case, the convection in itself is unstable.

REFERENCES

1. J. W. Gibbs, *Thermodynamics. Statistical Mechanics*, in *The Collected Works of J. Willard Gibbs* (Yale Univ. Press, New Haven, 1948; Nauka, Moscow, 1982).
2. L. D. Landau and E. M. Lifshitz, *Statistical Physics* (Nauka, Moscow, 1976; Pergamon, Oxford, 1980), Part 1.

Translated by V. Bukhanov

Doklady Physics, Vol. 46, No. 1, 2001, pp. 34–36. Translated from Doklady Akademii Nauk, Vol. 376, No. 3, 2001, pp. 328–330.

ENERGETICS

Explosive Regime of the Development of Instability Leading to Vapor-Film Collapse on a Heated Solid Hemispherical Surface

V. V. Glazkov*, V. G. Zhilin, Yu. A. Zeĭgarnik**, Yu. P. Ivochkin**, O. A. Sinkevich*, and V. P. Tsoĭ*****

Presented by A.I. Leont'ev March 28, 2000

Received April 27, 2000

We investigated the local processes proceeding in the case of changing the boiling regime on a heated cylindrical rod with a hemispherical end immersed in water (T = 285 K) at a depth equal to the radius of the hemisphere. The rod was heated in ambient air up to temperature $T \le 1000$ K.

Vapor-film escape was observed visually using a microscope and two video cameras installed below and aside from the hemisphere immersed in the liquid. The pressure arising in the liquid and the vapor-film thickness were measured using fiber-optical sensors [1]. In our experiments, we used metallic rods made of steel, pure copper, and copper covered by PSr62 silver solder.

After immersing the hemisphere in a liquid, free-convection flow formed near the heated surface. Then, wave formations appeared on the vapor–fluid interface. The amplitude and characteristic length of the surface waves were on the order of magnitude of a vapor-film thickness.

The process of vapor-film escape and passing to bubble boiling proceeded following two different scenarios. According to one of them, the wave perturbances having the form of isolated solitons or wave trains were enhanced with time and enveloped the entire hemisphere immersed in the water. Afterwards, a vapor-film explosion occurred and the nucleate-boiling regime was established. In a number of cases, the explosive boiling of the film was accompanied by the formation of a jet flow directed from the lower end of the hemisphere into the fluid. The explosive escape of the vapor film accompanied by the formation of the jet flow can be repeated (up to 30 times) in intervals of 0.3 to 1 s. In the other regime, the wave perturbances, once arisen, attenuated gradually and passed relatively smoothly to the nucleate-boiling regime. Smooth passage to nucleate boiling was observed only at the first immersion in water for a new hemisphere or for that freshly cleaned from oxides. In repeated experiments with surfaces having the oxide film, the vapor escaped explosively. In Figs. 1–3, we show photographs of a vapor film before explosion and with various types of its escape. The experiments were carried out under normal pressure, and the temperatures of the cooling water and heated surface were 293 and 795 K, respectively. The characteristic values of the vapor–fluid jet velocity (Fig. 3) attained 0.3 m/s.

Vibrations of the vapor-film surface were detected both at the second boiling crisis with quiet vapor-film escape and with vapor explosion. The characteristic longitudinal dimension of the wave structures attained

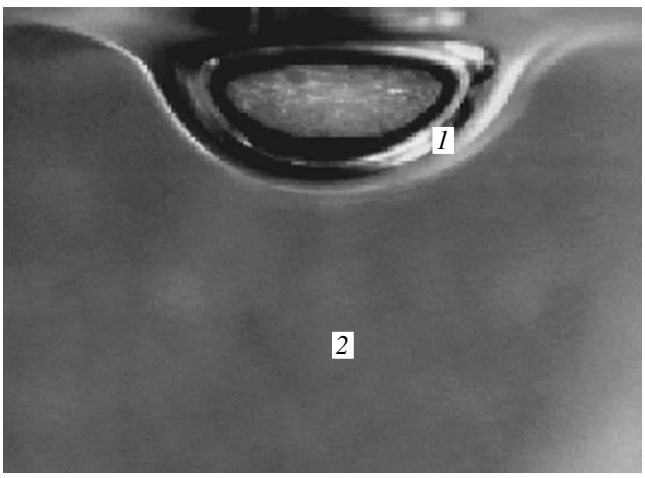

Fig. 1. Heated hemisphere immersed in water. The photograph corresponds to the last exposure of the film-boiling regime: (*1*) hemispherical solid surface with the vapor film and (*2*) water.

* *Moscow Power Institute, ul. Krasnokazarmennaya 17, Moscow, 111250 Russia*

** *Joint Institute for High Temperatures, Russian Academy of Sciences, ul. Izhorskaya 13/19, Moscow, 127412 Russia*

*** *Élektrogorsk Research Center, Élektrogorsk, Moscow oblast, Russia*

1028-3358/01/4601-0034$21.00

a value on the order of the vapor-film thickness (about 200 μm); i.e., they can be assigned to capillary waves. We can assume that the waves are maintained by the recoil pressure exerted by the vapor evaporated from their surface. In this case, it is necessary for the build-up of vibrations that the recoil-pressure growth be delayed with respect to the wave-amplitude growth.

This phenomenon can be explained in at least two ways. First, in the case of boiling with strong liquid underheating, a significant fraction of the growing heat flow at the stage of the wave-crest's approaching the surface is spent not for evaporation, but is transferred into the bulk of the liquid by the thermal-conduction mechanism. At the same time, at the stage of removing it from the surface, the near-surface layer is already heated and the arriving heat is spent only to evaporation. As a result, the recoil momentum at the stage of the wave's approaching the surface is lower than at the stage of removing; i.e., the wave is enhanced. The estimates show that this effect is relatively weak for capillary waves strongly attenuating owing to viscosity. This fact does not exclude the efficient character of this process for isolated solitons running along the vapor-film surface, since their damping decrement is much lower.

Second, we can assume that, for strongly nonequilibrium processes (in the experiments, the temperature gradient is higher than 10^7 K/m), overheating of the fluid manifests itself at the free surface. It is known that in flow problems, the free surface behaves as a solid wall; i.e., the evaporation from this surface can be hampered. Furthermore, for strongly nonequilibrium processes, the phonon-distribution function is substantially asymmetric in the fluid, which can also affect the evaporation probability from the surface. This fact is likely also confirmed by experiments involving overheated water with a free surface, for which temperatures $T^* = 563$ K were attained under normal conditions, provided that the characteristic heating time did not exceed a critical value τ_{cr}. According to the experiments performed [2], for water, $\tau_{cr} = 50$ μs; for other fluids, τ_{cr} is considerably higher and attains about 1 ms.

Within the framework of this hypothesis, we can formulate the following statement. When the amplitude of capillary waves increases to the extent that the fluid temperature at the wave crest attains the temperature of the maximum accessible overheating for this fluid, boiling occurs almost instantaneously. If the recoil momentum attained at the boiling is sufficiently high, it initiates a large-amplitude wave that, in turn, boils explosively, etc.

In order to estimate the recoil momentum experienced by the large-amplitude capillary wave during explosive boiling over a highly heat-conducting surface, we assume that the wave amplitude grows linearly with time t, having the characteristic rate $u_f/2$; i.e., $A = u_f t/2$, where $u_f = (\sigma/\rho_l\delta_0)^{1/2}$ is the velocity of a capillary wave with wavelength $l = 2\delta_0\pi$, δ_0 is the thickness of the unperturbed vapor film, σ is the surface-tension coefficient, and ρ_l is the density of the liquid. In this case, the conductive heat flow $q(t)$ to the wave surface, which is spent for overheating the fluid, increases according to the law $q(t) = \dfrac{q_0(t/\tau_0)}{1 - t/\tau_0}$, $\tau_0 = \dfrac{2\delta_0}{u_f}$, $q_0 = \dfrac{\lambda_s(T_w - \langle T_s\rangle)}{\delta_0}$, where $\langle T_s\rangle$ is the mean temperature of the fluid surface in the process of heating and λ_s is the thermal conductivity of the fluid. The temperature distribution in the fluid at the moment τ^*, when the fluid temperature on the wave surface attains the ultimate possible temperature of overheating and explosive boil-

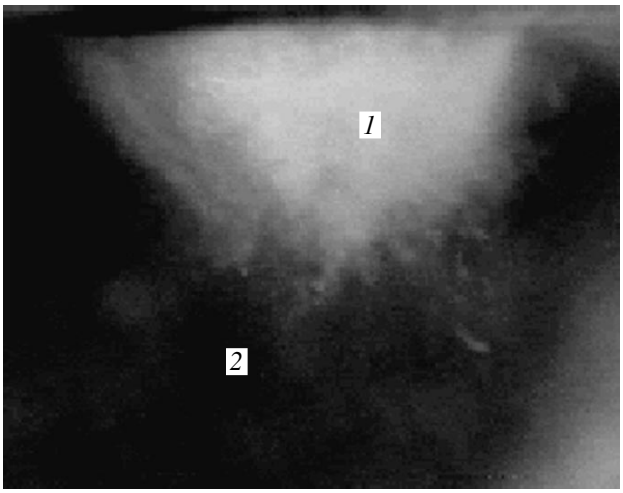

Fig. 2. Onset of the explosive vapor-film escape from the copper hemispherical surface freshly cleaned from oxides in the absence of generation of jet flows: (*1*) vapor and (*2*) water.

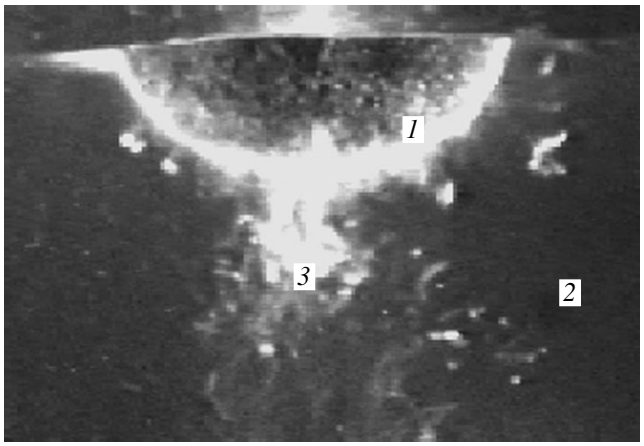

Fig. 3. Explosive escape of the vapor film from the hemispherical oxidized-copper surface, which is accompanied by the formation of a vapor-fluid jet: (*1*) vapor, (*2*) water, and (*3*) vapor–water jet.

ing begins, can be obtained in the one-dimensional approximation using the Green's functions. For the temperature on the surface, we have

$$T^* - T_s = \frac{2q_0\tau^*}{\rho_l C_l\sqrt{\pi a_l \tau^*}} \times\left(\frac{1}{\sqrt{(1-\varepsilon)\varepsilon}}\arctan\left(\sqrt{\frac{\varepsilon}{1-\varepsilon}}\right)-1\right), \quad (1)$$

where $\varepsilon = \frac{\tau^*}{\tau_0}$ and a_l and C_l are the thermal diffusivity and the heat capacity of the liquid. For the total heat transferred per unit area of the fluid surface, the integration yields

$$Q = q_0\tau_0[-\ln(1-\varepsilon)-\varepsilon]. \quad (2)$$

For the heat-flow density on the order of $q_0 = 10^5$–10^7 W/m^2, we have $\varepsilon \longrightarrow 1$, and the fluid is overheated only in the immediate vicinity of the surface. In this case, expression (1) acquires the asymptotic form

$$T^* - T_s = \frac{\sqrt{\pi}q_0\tau_0}{\rho_l C_l\sqrt{a_l\tau_0}}\left(\frac{1}{\sqrt{1-\varepsilon}}\right). \quad (3)$$

For $q_0 = 10^5$ W/m^2, $\delta_0 = 200$ μm, and $u_f = 0.5$ m/s, the minimum value δ_{min} of approaching the heating surface by the fluid amounts to hundredths of a micron, even though the surface temperature $T_w \approx 770$ K corresponding to the parameters indicated above is much higher than the temperature T^* of the ultimate overheating of the fluid. This immediate approach of the fluid to the heated surface is experimentally indistinguishable from a contact. The momentum Π transferred to a unit area of the surface in the case of explosive boiling of an overheated layer is on the order of $\Pi \sim \frac{Qc_s}{4r}$, where c_s is the velocity of sound in vapor and r is the evaporation heat. The condition for recoiling the fluid contained in the wave crest after the explosion with a momentum sufficient for generating a high-amplitude wave can be approximately written out in the form

$$\Pi \geq \rho_l u_f \delta_0 = \frac{\Pi}{\rho_l \delta_0 u_f} = \frac{c_s C_l\sqrt{a_l}\tau_0^{3/2}(T^* - T_s)}{8\sqrt{\pi}\delta_0^2 r}\sqrt{1-\varepsilon}\left[\ln\left(\frac{1}{1-\varepsilon}\right)-\varepsilon\right] \geq 1. \quad (4)$$

Condition (4) for water at atmospheric pressure is fulfilled within the range $q_0 = 2\times10^5$ W/m^2 to $q_0 = 3\times10^6$ W/m^2. Thus, no strong recoiling of the fluid from a wall which is capable of generating other interphase contacts arises either at exceptionally high or low temperature differences. With increasing saturation pressure, the difference $T^* - T_s$ decreases, tending to zero at the critical point. For $T^* - T_s < 50$ K ($P_s \sim 70$ bar), the strong-recoiling condition holds, without doubt, for none of the heat flows.

The density q of the heat flow from the surface in the case of a shock distortion of the film shape is $q \approx (3–4)q_0$. As estimates show, the dynamic action per unit area of the heater surface attains only few tens of pascals. However, its inhomogeneous distribution over the heated surface can lead to its fragmentation [3] if this surface is liquid-metallic. As follows from evident geometric considerations, the expansion rate for the region with an inhomogeneous film relief amounts to $\left(\frac{1}{4}-\frac{1}{8}\right)u_f$, which agrees with experimental data.

The cyclic character of initiation of interphase contacts in the case of film boiling with a frequency of contacts of about 1 kHz was experimentally discovered in water [4]. We may assume that synchronization of the explosive boiling of capillary-wave crests occurs at a wavy surface. As a result, an acoustic signal outgoing from the generation region represents not shot noise but pulse packets following with a frequency of $\nu \approx \frac{1}{\tau_0} \approx \left(\frac{u_f}{2\delta_0}\right) \sim 1.25$ kHz. This phenomenon was actually observed in experiment [4] and is indirect evidence that the explosive-boiling process is coherent.

ACKNOWLEDGMENTS

This work was supported by the Russian Foundation for Basic Research, project no. 99-02-17965.

REFERENCES

1. V. G. Zhilin, Yu. P. Ivochkin, A. A. Oksman, *et al.*, Teplofiz. Vys. Temp. **34**, 811 (1996).
2. V. P. Skripov, *Metastable Liquid* (Nauka, Moscow, 1972).
3. V. V. Glazkov and O. A. Sinkevich, Teploénergetika, No. 3, 27 (1998).
4. O. Dwyer, *Boiling Liquid-Metal Heat Transfer* (American Nuclear Society, Hinsdale, 1976; Mir, Moscow, 1980).

Translated by V. Bukhanov

Doklady Physics, Vol. 46, No. 1, 2001, pp. 37–40. Translated from Doklady Akademii Nauk, Vol. 376, No. 1, 2001, pp. 40–43.

MECHANICS

Symmetric Stability of Steady Axisymmetric and Geostrophic Motion in a Compressible Stratified Medium

P. N. Svirkunov

Presented by Academician G.S. Golitsyn July 7, 2000

Received April 6, 2000

We studied the stability of symmetric (i.e., independent of one of the coordinates) steady motion, axisymmetric and geostrophic. This motion is of considerable interest because it qualitatively describes the basic structures of atmospheric motion, such as zonal flows, vortices, and states of geostrophic balance. Since the first publication by Fjortoft [1], this problem has been studied (see, for example, [2–4]) with the aim to generalize its formulation and extend the range of possible application. It is worth noting that almost all studies were made in the approximation of incompressibility, which limits the use of the results to small- or moderate-scale atmospheric processes. Our study was undertaken to overcome the shortcomings of this approximation and to formulate the criteria of symmetric stability of compressible media described by an arbitrary equation of state. We consider here the general case of axisymmetric motion, including zonal flows, on the basis of the direct Lyapunov method (a variational approach).

1. We now write out a set of equations for the adiabatic axisymmetric motion of an ideal fluid in a system of cylindrical coordinates (r, z, φ) rotating about the z-axis with angular velocity Ω:

$$\frac{du}{dt} - \frac{1}{r^3}M^2 = -\frac{1}{\rho}\frac{\partial p}{\partial r} - \frac{\partial \varphi_{gr}}{\partial r}, \quad \frac{dw}{dt} = -\frac{1}{\rho}\frac{\partial p}{\partial z} - \frac{\partial \varphi_{gr}}{\partial z},$$
$$\frac{dM}{dt} = 0, \quad \frac{d\sigma}{dt} = 0, \quad \frac{dp}{dt} + \rho c^2\left(\frac{1}{r}\frac{\partial ru}{\partial r} + \frac{dw}{dz}\right). \tag{1}$$

Here u, w, and v_φ are the radial, vertical, and circular velocity components, respectively; $M = rv_\varphi + \Omega r^2$ is the absolute angular momentum; p and ρ are the pressure and density, respectively; φ_{gr} is the gravitational potential; σ is the specific entropy (per unit mass); and

$$\frac{d}{dt} = \frac{\partial}{\partial t} + u\frac{\partial}{\partial r} + w\frac{\partial}{\partial z}.$$

The last equation of set (1) is used instead of the conventional continuity equation and can be obtained from it with due regard for the given equation of state $\rho = \rho(p, \sigma)$ and the adiabaticity condition. The density is determined from the equation of state. The motion is considered in a certain finite region bounded by surfaces of revolution (coaxial with the z-axis) where the normal velocity component vanishes.

The state of the system is defined by the set of variables (u, w, M, p, σ). The variables corresponding to the steady state are marked with bars. It is also assumed that the Jacobian $\frac{\partial(\bar{M}, \bar{\sigma})}{\partial(r, z)}$ has a nonzero value. Set (1) yields the steady-state equations

$$\frac{1}{r^3}\bar{M}^2 = \frac{1}{\bar{\rho}}\frac{\partial \bar{p}}{\partial r} + \frac{\partial \varphi_{gr}}{\partial r}, \quad \frac{\partial \varphi_{gr}}{\partial z} = -\frac{1}{\bar{\rho}}\frac{\partial \bar{p}}{\partial z}. \tag{2}$$

Theorem 1. *If the conditions*

$$\frac{\partial \bar{\sigma}}{\partial z}\frac{\partial \varphi_{gr}}{\partial z} > 0 \quad and \quad \overline{M}\bar{\Omega}_p\frac{\partial \varphi_{gr}}{\partial z} > 0 \tag{3}$$

are satisfied, the steady-state motion described by Eq. (2) *is stable in the Lyapunov sense for axisymmetric disturbances, with* Ω_p *being an absolute potential vortex.*

Proof. We write out the Bernoulli function for steady motion as

$$H = \frac{1}{2r^2}\bar{N} + \varphi_{gr} + h(\bar{p}, \bar{\sigma}). \tag{4}$$

Hereafter, $N = M^2$ and $h(p, \sigma)$ is the specific enthalpy (per unit mass) related to the specific internal energy as $h = \varepsilon + \frac{1}{\rho}p$. Using the thermodynamic equation $dh = Td\sigma + \frac{1}{\rho}dp$ (where T is temperature), we can write Eqs. (2) in the form

$$\nabla H = \frac{1}{2r^2}\nabla \bar{N} + \bar{T}\nabla\bar{\sigma}, \quad \nabla = \left(\frac{\partial}{\partial r}, \frac{\partial}{\partial z}\right). \tag{5}$$

TAĬFUN Research and Production Association, Obninsk, Kalyzhskaya oblast, Russia

1028-3358/01/4601-0037$21.00

We now denote by $H(\sigma, N)$ the function obtained from H by expressing the coordinates r and z in terms of N and σ and solving the equations

$$N = \bar{N}(r, z), \quad \sigma = \bar{\sigma}(r, z). \tag{6}$$

Then, using (5), we can show that the function $H(\sigma, N)$ satisfies the relationships

$$\frac{\partial H}{\partial N} = \frac{1}{2r^2}, \quad \frac{\partial H}{\partial \sigma} = \bar{T} \quad \text{for } N = \bar{N} \text{ and } \sigma = \bar{\sigma}. \tag{7}$$

We define the Lyapunov functional by the relation

$$L(u, w, N, \rho, \sigma) = \int_V dV\left[\frac{1}{2}\rho(u^2 + w^2) + \frac{1}{2r^2}\rho N + \rho\varphi_{gr} + \rho h - p - \rho H(\sigma, N)\right].$$

Integration is performed over the entire flow region. The functional remains constant for the solutions to system (1). Indeed, the last term in the integrand is the density for the Lagrange invariant, whereas the sum of all the remaining terms is the total-energy density (in the fixed coordinate system).

We now consider the variations in L in the vicinity of the steady state. Expanding $L(\delta u, \delta w, \bar{N} + \delta N, \bar{p} + \delta p, \bar{\sigma} + \delta\sigma)$ into a power series in deviations (δ indicates the deviation of the variable from its steady value) and using (4) and (7), we find that the first variation goes to zero.

According to the general theory [5], in this case, a steady state is stable in the Lyapunov sense in the norm equivalent to $\delta^2 L$ if the second variation $\delta^2 L$ is positive.

The second variation for a steady state is reduced to the form

$$\delta^2 L = \frac{1}{2}\int_V dV\bar{\rho}(\delta u^2 + \delta w^2) + \frac{1}{2}\int_V dV\left[\frac{1}{\bar{\rho}c^2}\delta p^2 - \bar{\rho}H''_{NN}\delta N^2 - 2\bar{\rho}H''_{\sigma N}\delta\sigma\delta N + \bar{\rho}\left(\left(\frac{\partial T}{\partial \sigma}\right)_p - H''_{\sigma\sigma}\right)\delta\sigma^2\right]. \tag{8}$$

The sufficient condition for positiveness of $\delta^2 L$ is

$$H''_{NN} < 0, \quad H''_{NN}\left(\left(\frac{\partial T}{\partial \sigma}\right)_p - H''_{\sigma\sigma}\right) + H''^2_{\sigma N} < 0. \tag{9}$$

The second derivatives in (9), obtained by differentiating Eq. (7) with due regard for Eq. (6), are

$$H''_{NN} = -\frac{1}{r^3}\left(\frac{\partial r}{\partial N}\right)_\sigma,$$

$$H''_{\sigma N} = -\frac{1}{r^3}\left(\frac{\partial r}{\partial \sigma}\right)_N = \left(\frac{\partial T}{\partial p}\right)_\sigma\left(\frac{\partial \bar{p}}{\partial N}\right)_\sigma,$$

$$\left(\frac{\partial T}{\partial p}\right)_\sigma - H''_{\sigma\sigma} = -\left(\frac{\partial T}{\partial p}\right)_\sigma\left(\frac{\partial \bar{p}}{\partial \sigma}\right)_N.$$

Then, we transform inequalities (9) to the form

$$\left(\frac{\partial r}{\partial N}\right)_\sigma > 0, \quad \left(\frac{\partial T}{\partial p}\right)_\sigma \frac{\partial(r, \bar{p})}{\partial(\sigma, N)} > 0. \tag{10}$$

The first inequality, generalizing the well-known Rayleigh criterion, shows that on the isentropic surfaces, the squared absolute angular momentum is an increasing function of r. The second inequality depends on the thermodynamic characteristics of the medium. It is well known from electrodynamics that

$$\left(\frac{\partial T}{\partial p}\right)_\sigma = \frac{1}{c_p}T\left(\frac{\partial v}{\partial T}\right)_p,$$

where c_p is the specific thermal capacity at constant pressure and v is the specific volume.

For most materials, $\left(\frac{\partial v}{\partial T}\right)_p > 0$. Limiting our consideration to this case and taking the derivatives with respect to r and z in (10), with (2) taken into account, we can show that inequalities (10) can be written in the following equivalent form:

$$\left(\frac{\partial \bar{\sigma}}{\partial z}\right)_r \frac{\partial \varphi_{gr}}{\partial z} > 0, \quad \frac{\partial(\bar{N}, \bar{\sigma})}{\partial(r, z)}\frac{\partial \varphi_{gr}}{\partial z} > 0. \tag{11}$$

In the case of axisymmetric flow, the potential vortex Ω_p has the form

$$\Omega_p = \frac{1}{\rho r}\frac{\partial(M, \sigma)}{\partial(r, z)}, \tag{12}$$

such that, with due regard for equality $\bar{N} = \bar{M}^2$, inequalities (11) are identical to (3).

As an example, we consider the case of a zonal flow. Strictly speaking, the potential of a rotating planet is not spherically symmetric; however, with a sufficient accuracy, it is symmetric with respect to the equatorial plane; i.e., $\varphi_{gr} = \varphi_{gr}(r, z^2)$. Therefore, the second condition in (3) requires the product $\bar{M}\bar{\Omega}_p$ to be positive in the northern hemisphere and negative in the southern. The available data on potential-vortex distribution (see review [6]) indicate that, on the whole, the second stability condition in (3) is satisfied. If the quantity $\bar{M}\bar{\Omega}_p$ (or the meridional gradient $\bar{\sigma}$) has a nonzero value on the equator, conditions (3) are violated. However, it is unclear whether this should lead to instability of the steady state or not. This problem deserves special study, but for incompressible fluids [3, 4], this conclusion is quite correct; therefore, we believe that it may be correct for compressible media as well.

Prior to further consideration, some remarks should be made. For axisymmetric motion, there exist more than two Lagrange invariants and, therefore, the poten-

tial vortex Ω_p is a function of M and σ. In [6], the dependence $\Omega_p(M, \sigma)$ is referred to as a functional invariant because, being determined from the initial M_0 and σ_0 values, it remains constant. In what follows, the states with identical functional invariants are called equivalent states.

2. The principle of the energy minimum. A steady state for which stability conditions (3) are satisfied has the energy minimal in the class of equivalent states. For incompressible fluids, this principle was proved in [4, 7] and interpreted in [7].

We represent the difference in the energies of a steady state and a state equivalent to it in the form

$$\begin{aligned} &E(u, w, M, p, \sigma) - E(0, 0, \bar{M}, \bar{p}, \bar{\sigma}) \\ &= \int_V dV\Big[\frac{1}{2}\rho(u^2 + w^2) + \frac{1}{2r^2}\rho N \\ &\quad + \rho\varphi_{gr} + \varepsilon(p, \sigma)\rho - \frac{1}{2r^2}\bar{\rho}\bar{N} \\ &\quad - \bar{\rho}\varphi_{gr} - \bar{\rho}\varepsilon(\bar{p}, \bar{\sigma}) + \rho H(\sigma N) - \bar{\rho}H(\bar{\sigma}, \bar{N})\Big]. \end{aligned} \tag{13}$$

The contributions of the two last terms to the integral compensate each other. To prove this statement, we change variables $(r, \bar{z}) \longrightarrow (M, \sigma)$ and $(r, z) \longrightarrow (\bar{M}, \bar{\sigma})$ and make use of relationship (12), taking into account that the values of Ω_p, being the functions of M and σ, are equal for the equivalent states.

If the stability conditions are satisfied, the integrand in (13), being a function of (u, w, N, p, σ), is convex at each point of the flow domain and, together with its first derivatives, becomes zero at the point $(0, 0, \bar{N}, \bar{p}, \bar{\sigma})$. This implies that if $(u, w, N, p, \sigma) \neq (0, 0, \bar{N}, \bar{p}, \bar{\sigma})$, the integrand is positive, whence follows the above statement.

Of course, this principle is also valid in a rotating coordinate system, which can be readily proved by taking into account the law of energy transformation in the transition to such a coordinate system:

$$E \longrightarrow E - \Omega\int_V \rho\, M dV.$$

3. We now consider the symmetric stability of a state of cyclostrophic balance. For symmetric motion in the f-plane model, the dynamic equations in the Cartesian system take the form

$$\begin{aligned} &\frac{du}{dt} = -\frac{1}{\rho}\frac{\partial p}{\partial x} + fv, \quad \frac{dv}{dt} = -fu, \\ &\frac{dw}{dt} = -\frac{1}{\rho}\frac{\partial p}{\partial z} - g, \\ &\frac{d\sigma}{dt} = 0, \quad \frac{dp}{dt} + \rho c^2\Big(\frac{\partial u}{\partial x} + \frac{\partial w}{\partial z}\Big). \end{aligned} \tag{14}$$

where u, v, and w are the velocity components along the x-, y-, and z-axes, respectively; f is the Coriolis parameter; and the operator $\frac{d}{dt}$ now has the form $\frac{d}{dt} = \frac{\partial}{\partial t} + u\frac{\partial}{\partial x} + w\frac{\partial}{\partial z}$. The second equation can be rewritten in the form of a law of conservation for a geostrophic momentum $m = fx + v$: $\frac{dm}{dt} = 0$. The state of the system is defined by the set of variables (u, w, m, p, σ). We assume that the Jacobian $\frac{\partial(\bar{m}, \bar{\sigma})}{\partial(x, z)}$ has a nonzero value. The steady state of the geostrophic balance satisfies the conditions

$$\bar{u} = \bar{w} = 0, \quad (\bar{m} - fx)f = \frac{1}{\bar{\rho}}\frac{\partial \bar{p}}{\partial x}, \quad g = -\frac{1}{\bar{\rho}}\frac{\partial \bar{p}}{\partial z}. \tag{15}$$

Theorem 2. *If the conditions*

$$\Big(\frac{\partial \bar{\sigma}}{\partial z}\Big)_x > 0, \quad f\bar{\Omega}_p > 0 \tag{16}$$

are satisfied, steady state (15) *is stable in the Lyapunov sense in the class of symmetric perturbances.*

The theorem will be proved as in the previous case. We define a function H by the equality

$$H = -\bar{m}xf + \frac{1}{2}x^2f^2 + gz + h(\bar{p}, \bar{\sigma})$$

satisfying the equation

$$\nabla H = -xf\,\nabla\bar{m} + \bar{T}\nabla\bar{\sigma}, \quad \nabla = \Big(\frac{\partial}{\partial x}, \frac{\partial}{\partial z}\Big). \tag{17}$$

We now denote by $H(\sigma, m)$ the function obtained from H, provided that the coordinates x and z are expressed in terms of m and σ, by solving the equations $m = \bar{m}(x, z)$ and $\sigma = \bar{\sigma}(x, z)$. The desired function satisfies the conditions

$$\Big(\frac{\partial H}{\partial m}\Big)_\sigma = -xf \quad \text{and} \quad \Big(\frac{\partial H}{\partial \sigma}\Big)_m = \bar{T} \quad \text{for } m = \bar{m} \text{ and } \sigma = \bar{\sigma}. \tag{18}$$

The Lyapunov functional is set as

$$\begin{aligned} L = \int_V \partial V\Big[&\frac{1}{2}\rho(u^2 + w^2) + \rho\Big(-mxf + \frac{1}{2}x^2f^2 + gz\Big) \\ &+ \rho h(p, \sigma) - p - \rho H(m, \sigma)\Big]. \end{aligned} \tag{19}$$

The above functional remains constant for the solutions of system (14). Indeed, the last term in the integrand is

the density of a Lagrange invariant, whereas the sum of the remaining terms is the energy density with the subtracted density of the Lagrange invariant $\frac{1}{2}\rho m^2$. The first variation L for a steady state becomes zero, whereas the second one acquires the form identical to (8), provided that N is replaced by m. The condition of $\delta^2 L$ positiveness is similar to (9). The second derivatives entering into this condition are obtained from (18), which is formally equivalent to (7) upon substitution of $\frac{1}{2r^2}$ with $-xf$. As a result, the positiveness condition for $\delta^2 L$ acquires the form

$$f\left(\frac{\partial x}{\partial m}\right)_\sigma > 0, \quad \left(\frac{\partial T}{\partial p}\right)_\sigma f\frac{\partial(x, p)}{\partial(\sigma, N)} > 0. \tag{20}$$

The first inequality shows that, on isentropes, the geostrophic momentum is an increasing function of x. Assuming that $\left(\frac{\partial T}{\partial p}\right)_\sigma > 0$, passing to the independent variables x and z in (20), and performing certain transformations, we see that (20) is actually equivalent to (16). In this case, we also made use of the expression for symmetric motions of a potential vortex:

$$\Omega_p = \frac{1}{\rho}\frac{\partial(m, \sigma)}{\partial(x, z)}.$$

The principle of the energy minimum for stable steady states is formulated and proved in an analogous way. In this case, the role of the functional invariant is played by a potential vortex expressed in terms of the Lagrange invariants m and σ.

REFERENCES

1. R. Fjortoft, Geophys. Publ. **17** (6), 1 (1950).
2. B. J. Hoskins, Q. J. R. Meteorol. Soc. **100**, 480 (1974).
3. H.-R. Cho, T. G. Shepherd, and V. A. Vladimirov, J. Atmos. Sci. **50**, 822 (1993).
4. P. N. Svirkunov, Prikl. Mat. Mekh. **62**, 996 (1998).
5. V. I. Arnol'd, Dokl. Akad. Nauk SSSR **162**, 975 (1965).
6. M. V. Kurganskiĭ and M. S. Tatarskaya, Izv. Akad. Nauk SSSR, Fiz. Atmos. Okeana **23**, 787 (1958).
7. M. V. Kalashnik and P. N. Svirkunov, Meteorol. Gidrol., No. 4, 58 (1998).

Translated by V. Chechin

Doklady Physics, Vol. 46, No. 1, 2001, pp. 4–8. Translated from Doklady Akademii Nauk, Vol. 376, No. 2, 2001, pp. 178–182.

PHYSICS

Effect of Polarized Radiation on Conductivity of Thin Anisotropic Metal Films

M. A. Olevanov

Presented by Academician A.M. Dykhne January 25, 2000

Received February 15, 2000

A change in conductivity of a deformed metal film in an external high-frequency field is theoretically calculated. This effect was recently discovered by V.V. Ragul'skiĭ in experiments with thin aluminum films [1].

In the model considered here, a linearly polarized electromagnetic wave with amplitude $\tilde{\mathbf{E}}$ and frequency ω is normally incident onto the surface of a uniformly deformed metal film. The electric current induced by a constant field $\mathbf{E}_0$ applied along the deformation axis flows along the film. Two cases are considered: (1) an incident wave is polarized along the direction of the current flow and (2) an incident wave is polarized normal to the current flow.

The solution to the problem is based on solution of the Boltzmann equation and determination of the electron distribution function in the presence of an electric field and the field of a light wave. Since a high-frequency field cannot penetrate deeply into a massive metal, the phenomenon under consideration is of a purely subsurface character and therefore can be observed only in very thin samples with a thickness comparable to that of a skin layer. Thus, in our further calculations, the intensity of the light-wave field can be assumed to be independent of the spatial coordinate, and, thus, by solving the kinetic equation, we can assume that the distribution function is independent of the spatial coordinate.

Now, we write out the Boltzmann equation for the distribution function of the electron gas in metal in the following form:

$$\frac{\partial f}{\partial t} - \frac{e}{\hbar}\mathbf{E}\frac{\partial f}{\partial \mathbf{k}} = \left(\frac{\partial f}{\partial t}\right)_{\text{col}}. \tag{1}$$

Here, $\mathbf{k}$ is the wave vector of an electron in the phase space, $\mathbf{E}$ is the total electric field acting on an electron, and the collision integral has the form [2]

$$\left(\frac{\partial f}{\partial t}\right)_{\text{col}} = \int dV_{\mathbf{k}'}\{W(\mathbf{k}', \mathbf{k})(1 - f(\mathbf{k}))f(\mathbf{k}') - W(\boldsymbol{k}, \mathbf{k}')(1 - f(\mathbf{k}'))f(\mathbf{k})\}\rho(\mathbf{k}'). \tag{2}$$

Here, $\rho(\mathbf{k})$ is the density of states and the term $W(\mathbf{k}, \mathbf{k}')$ characterizes the probability of the transition of an electron from the state $\mathbf{k}$ into the state $\mathbf{k}'$ under the condition that the former state is occupied and the latter one is vacant.

We represent the distribution function of electrons as $f = f_0 + \delta f$, where $\delta f \ll f_0$ and f_0 is the equilibrium distribution function, and substitute it into Eq. (1). Upon certain transformations, we have

$$\frac{\partial \delta f}{\partial t} - \frac{e}{\hbar}\mathbf{E}\frac{\partial f_0}{\partial \mathbf{k}} = -\delta f(\mathbf{k}) \oint\limits_{\mathscr{E}(\mathbf{k})} W(\mathbf{k}', \mathbf{k})\left(1 - \frac{\delta f(\mathbf{k}')}{\delta f(\mathbf{k})}\right)\frac{\rho(\mathbf{k}')dS_{\mathscr{E}}}{|\nabla_{\mathbf{k}'}\mathscr{E}|}. \tag{3}$$

Integration in the right-hand side is performed over the surface of the constant energy.

The simplest solution to Eq. (3) is obtained for the model of almost free electrons. In this case, the dispersion relation has a simple form:

$$\mathscr{E}(\mathbf{k}) = \frac{\hbar^2\mathbf{k}^2}{2m_0}. \tag{4}$$

The energy is measured from the bottom of the conduction band. Thus, the isoenergetic surfaces in the phase space have a spherical shape. Under these conditions, it is possible to introduce the relaxation parameter by assuming that the integral in the right-hand side of Eq. (3) does not depend on δf and by obtaining a self-consistent solution to Eq. (3):

$$\delta f = \frac{e\hbar\tau_0}{m_0}\frac{\partial f_0}{\partial \mathscr{E}}(\mathbf{k} \cdot \mathbf{E}^*). \tag{5}$$

Here, τ_0 is the relaxation time and m_0 is the effective mass of an electron in the metal. We also used the fol-

Moscow State University,
Vorob'evy gory, Moscow, 119899 Russia

1028-3358/01/4601-0004$21.00

lowing notation:

$$\mathbf{E}^* = \mathbf{E}_0 + \frac{\tilde{\mathbf{E}}}{\sqrt{1+(\omega\tau_0)^2}}\cos\omega t.$$

In fact, the above formula also includes the phase, but since it is inessential for further consideration of the problem, it is omitted. In addition, we also introduce the following notation:

$$\frac{\tilde{\mathbf{E}}}{\sqrt{1+(\omega\tau_0)^2}} = \mathbf{E}'.$$

Thus, the approximation of almost free electrons leads us to the classical formula for conduction in metals.

If there is a certain deformation, the model would also take into account anisotropy in the shape of isoenergetic surfaces. However, since the film deformation is rather small, its effect on the distribution function of electrons can be considered a small perturbance.

Now, we determine the correction to the solution of Eq. (3). With this aim, we substitute the value of δf for almost free electrons into the collision integral in the right-hand side of Eq. (3),

$$\left(\frac{\partial f(\mathbf{k})}{\partial t}\right)_{\text{col}} = -\delta f(\mathbf{k}) \oint\limits_{\mathscr{E}(\mathbf{k})} W(\mathbf{k}', \mathbf{k})\left(1-\frac{(\mathbf{k}'\cdot\mathbf{E}^*)}{(\mathbf{k}\cdot\mathbf{E}^*)}\right)\frac{\rho(\mathbf{k}')dS_{\mathscr{E}}}{|\nabla_{\mathbf{k}'}\mathscr{E}|}, \quad (6)$$

and consider the case $\mathbf{E}_0 \parallel \tilde{\mathbf{E}}$, i.e., the radiation polarized along the current flow. The axis **x** is taken to be parallel to the field $\mathbf{E}_0$. Then, the field-dependent term in the integrand can be transformed as follows:

$$\frac{(\mathbf{k}'\cdot\mathbf{E}^*)}{(\mathbf{k}\cdot\mathbf{E}^*)} = \frac{k_x'(E_0+E'\cos\omega t)}{k_x(E_0+E'\cos\omega t)} = \frac{k_x'}{k_x}. \quad (7)$$

It is seen that the collision integral for $\mathbf{E}_0 \parallel \tilde{\mathbf{E}}$ and that for the case of unexplored film have the same form. In other words, illumination of the film with the light polarized along the current flow does not affect its conductivity. This conclusion is quite consistent with experimental data [1].

Thus, we can write for τ_0,

$$\frac{1}{\tau_0} = \oint\limits_{\mathscr{E}(\mathbf{k})} W(\mathbf{k}', \mathbf{k})\left(1-\frac{k_x'}{k_x}\right)\frac{\rho(\mathbf{k}')dS_{\mathscr{E}}}{|\nabla_{\mathbf{k}'}\mathscr{E}|}. \quad (8)$$

We now consider the case $\mathbf{E}_0 \perp \tilde{\mathbf{E}}$. Let the constant component of the electric field be directed along the **x**-axis and the variable component be directed along the **y**-axis. The axis normal to the film surface is denoted by **z**. These axes are also the principal axes of the deformation tensor. Then, the field-dependent term in (6) is written as

$$\frac{(\mathbf{k}'\cdot\mathbf{E}^*)}{(\mathbf{k}\cdot\mathbf{E}^*)} = \frac{k_x'E_0 + k_y'E'\cos\omega t}{k_xE_0 + k_yE'\cos\omega t}. \quad (9)$$

It is seen that the collision integral is a rapidly varying periodic function of time. Denoting the field-dependent integral in the right-hand side of Eq. (6) as $g(\omega t)$, we obtain

$$\left(\frac{\partial f}{\partial t}\right)_{\text{col}} = -\delta f g(\omega t). \quad (10)$$

Substituting (10) into the Boltzmann equation, we have

$$\frac{\partial\delta f}{\partial t} - \frac{e}{\hbar}\mathbf{E}\frac{\partial f_0}{\partial\mathbf{k}} = -\delta f(\mathbf{k})g(\omega t). \quad (11)$$

Since all the functions in Eq. (11) are periodic, it can be solved as a sum of harmonics, but, since we must calculate the sample conductivity for the constant current, we restrict ourselves to the zero harmonics δf_c:

$$\delta f_c = \frac{\dfrac{e\hbar}{m_0}\dfrac{\partial f_0}{\partial\mathscr{E}}k_xE_0}{\dfrac{1}{2\pi}\displaystyle\int_{-\pi}^{\pi} g(\omega t)d\omega t}. \quad (12)$$

Comparing (12) and (5), we see that the expression in the denominator of (12) has the meaning of $\frac{1}{\tau}$, where τ is the relaxation time. The integral in the right-hand side of (12) can be readily calculated, and we obtain

$$\frac{1}{\tau} = \oint\limits_{\mathscr{E}(\mathbf{k})} W(\mathbf{k}', \mathbf{k}) \times\left(1-\frac{k_y'}{k_y}-\left(\frac{k_x'}{k_x}-\frac{k_y'}{k_y}\right)\frac{1}{\sqrt{1-\dfrac{E'^2k_y^2}{E_0^2k_x^2}}}\right)\frac{\rho(\mathbf{k}')dS_{\mathscr{E}}}{|\nabla_{\mathbf{k}'}\mathscr{E}|} \quad \text{for } \left|\frac{E'}{E_0}\frac{k_y}{k_x}\right| < 1, \quad (13)$$

$$\frac{1}{\tau} = \oint\limits_{\mathscr{E}(\mathbf{k})} W(\mathbf{k}', \mathbf{k})\left(1-\frac{k_y'}{k_y}\right)\frac{\rho(\mathbf{k}')dS_{\mathscr{E}}}{|\nabla_{\mathbf{k}'}\mathscr{E}|} \quad \text{for } \left|\frac{E'}{E_0}\frac{k_y}{k_x}\right| > 1.$$

Using (8), we can reduce (13) to a more compact form:

$$\frac{1}{\tau} = \frac{1}{\tau_0} + \frac{\Omega}{k_x k_y}\begin{cases} 1 - \dfrac{1}{\sqrt{1 - \dfrac{E'^2 k_y^2}{E_0^2 k_x^2}}} & \text{for } \left|\dfrac{E' k_y}{E_0 k_x}\right| < 1 \\ 1 \quad \text{for } \left|\dfrac{E' k_y}{E_0 k_x}\right| > 1, \end{cases} \tag{14}$$

where τ_0 is the relaxation time in the absence of illumination. We also used the notation

$$\Omega = \oint_{\mathscr{E}(\mathbf{k})} W(\mathbf{k}', \mathbf{k})[\mathbf{k}' \times \mathbf{k}]_z \frac{\rho(\mathbf{k}')dS_{\mathscr{E}}}{|\nabla_{\mathbf{k}'}\mathscr{E}|}. \tag{15}$$

Integration in (15) is performed over the surface of the constant energy. It can be readily shown that in the isotropic case corresponding to dispersion equation (4), this integral tends to zero. In other words, for an undeformed film, the irradiation does not affect film conductivity.

We now consider how the shape of isoenergetic surfaces depends on weak anisotropy. If an ideal lattice is subjected to uniform deformation characterized by strain tensor ξ_{ij}, with the components being less than unity, the energy spectrum of the electrons can be represented in the form

$$\mathscr{E}(\mathbf{k}, \xi) = \frac{\hbar^2 \mathbf{k}^2}{2m_0} + \frac{\hbar^2}{2m'}\xi_{ij}k_i k_j. \tag{16}$$

The coefficients m_0 and m' calculated for a number of metals can be found elsewhere [3]. The calculated effective masses are close to the mass of a free electron. Moreover, the coefficients m' have negative values.

For simplicity, we assume that only one component of the deformation tensor corresponding to extension or compression of the sample along the **x**-axis differs from zero (the ξ-component). Then, the equation for the isoenergetic surface is written as

$$\frac{\hbar^2}{2} m_0^{-1} k^2 (1 - \Delta \cos^2\theta) = \mathscr{E}. \tag{17}$$

Here, θ is the angle between vector **k** and the deformation axis and $\Delta = -\dfrac{m_0}{m'}\xi$, where m_0 is the effective electron mass in the isotropic metal. Taking into account that m_0 and m' are of the same order of magnitude but have opposite signs, we can write within the accuracy to the factor on the order of unity that $\Delta \simeq \xi \ll 1$.

Now, we perform integration in (15) along the surface of the constant energy given by Eq. (17). Then, in the first order of the perturbation theory with respect to Δ within the accuracy to the factor on the order of unity, we find

$$\Omega = -\frac{\Delta}{4} k_x k_y \frac{1}{\tau_0}. \tag{18}$$

Thus, the parameter $\dfrac{1}{\tau}$ can be obtained as

$$\frac{1}{\tau} = \frac{1}{\tau_0} - \frac{\Delta}{4}\frac{1}{\tau_0}\begin{cases} 1 - \dfrac{1}{\sqrt{1 - \dfrac{E'^2 k_y^2}{E_0^2 k_x^2}}} & \text{for } \left|\dfrac{E' k_y}{E_0 k_x}\right| < 1 \\ 1 \quad \text{for } \left|\dfrac{E' k_y}{E_0 k_x}\right| > 1. \end{cases} \tag{19}$$

It is seen from this expression that film anisotropy gives rise to anisotropy of the relaxation time depending not only on the direction in the crystal but also, in a rather complicated way, on the induced fields. We write this dependence as $\tau = \tau_0 \psi(\theta, \alpha)$, where θ is the angle formed by the direction for which the relaxation time should be determined and the **x**-axis, whereas the new parameter α determines the effect of the fields:

$$\alpha = \frac{\tilde{E}^2/E_0^2}{1 + (\omega\tau_0)^2}. \tag{20}$$

The function ψ introduced above has the following form:

$$\psi(\theta, \alpha) = \begin{cases} \dfrac{\sqrt{1 - \alpha\tan^2\theta}}{\left(1 - \dfrac{\Delta}{4}\right)\sqrt{1 - \alpha\tan^2\theta} + \dfrac{\Delta}{4}} & \text{for } \left|\sqrt{\alpha}\tan\theta\right| < 1 \\ \dfrac{1}{1 - \dfrac{\Delta}{4}} \quad \text{for } \left|\sqrt{\alpha}\tan\theta\right| > 1. \end{cases} \tag{21}$$

We now substitute the integral in (12) for the expression found for the relaxation time:

$$\delta f_c = \frac{e\hbar}{m_0}\frac{\partial f_0}{\partial \mathscr{E}} k_x E_0 \tau_0 \psi(\theta, \alpha). \tag{22}$$

Since the distribution function for electrons is known, we can calculate the electric current density in the sample and determine the conductivity. One can readily see from (22) that the change in electrical conductivity of the deformed illuminated film is now determined only by the new angular dependence in the distribution function. Thus, the relative change in conductivity is given by the following integral formula:

$$\frac{\sigma - \sigma_0}{\sigma_0} = \frac{\int_0^{\pi}\int_0^{2\pi} \psi(\alpha, \theta)\cos^2\theta\sin\theta d\theta d\varphi - \int_0^{\pi}\int_0^{2\pi} \cos^2\theta\sin\theta d\theta d\varphi}{\int_0^{\pi}\int_0^{2\pi} \cos^2\theta\sin\theta d\theta d\varphi}, \quad (23)$$

where σ_0 is the conductivity of not illuminated film. Substituting (21) into (23) and performing integration, we obtain

$$\frac{\Delta\sigma}{\sigma_0} = \frac{\Delta}{4}\left(1 - \frac{1+3\alpha}{(1+\alpha)^2}\right). \quad (24)$$

Analyzing the above expression, we see that the relative change in conductivity depends on two parameters: $\Delta \simeq \xi \ll 1$ (where ξ is the strain) and α (proportional to the intensity of the incident radiation). The behavior of the relative change in conductivity at various values of parameter α is shown in the figure in units of Δ.

Now, we consider the behavior of the dependence obtained at high and low values of parameter α. At $\alpha \ll 1$, Eq. (24) yields the following asymptotic dependence:

$$\frac{\Delta\sigma}{\sigma_0} \simeq -\Delta\frac{\alpha}{4}. \quad (25)$$

In other words, in the domain of parameters considered above, the relative change in conductivity should linearly depend on the intensity of the incident radiation.

At $\alpha \gg 1$, Eq. (24) takes the form

$$\frac{\Delta\sigma}{\sigma_0} \simeq \frac{\Delta}{4}\left(1 - \frac{3}{\alpha}\right); \quad (26)$$

i.e., under extremely intense film illumination, the relative change in conductivity, which is inversely proportional to the intensity of the incident radiation, attains saturation.

Thus, the conductivity of a thin uniformly deformed conductor depends on the polarization of the incident radiation. This effect is caused by anisotropy in the shape of the isoenergetic surfaces caused by sample deformation.

We now compare the predictions of the theoretical model with the experimental results obtained in [1].

First, we consider a qualitative behavior of the effect. We have shown that the conductivity of the irradiated sample changes only if the incident wave is polarized normal to the direction of the electric current in the film. If the wave is polarized longitudinally with respect to the current flow, the conductivity is not changed as in the absence of an external field. This conclusion is quite consistent with experimental results.

To analyze the quantitative results, we have to determine the range of the model parameters corresponding to the experimental conditions. As was shown above, the relative change in conductivity depends on two parameters: $\Delta \simeq \xi \ll 1$ (where ξ is the strain) and α [given by formula (20)]. The field intensity and the frequency of the incident wave in the experiments [1] were the following: $\tilde{E} \leq 3.5$ V/cm, $E_0 = 5$ V/cm, $\omega = 2.98 \times 10^{15}$ s^{-1}.

The relaxation time in (20) can be evaluated from the classical formula

$$\tau_0 = \frac{m\sigma}{e^2 n}. \quad (27)$$

The conductivity of aluminum equals $\sigma = 3.5 \times 10^7\ \Omega^{-1}\ \text{m}^{-1} = 3.1 \times 10^{17}\ \text{S}^{-1}$ [4]. The average number of electrons per aluminum atom is 1.31 (see [5], p. 126). The aluminum density is $\rho = 2.7$ g/cm^3, and the molar mass is $\mu = 27$ g/mol. Then, the number of conduction electrons per unit volume can be readily calculated as

$$n = 1.31\frac{\rho}{\mu}N_A = 7.9 \times 10^{22}\ \text{cm}^{-1}. \quad (28)$$

Substituting all the values obtained into (27), we have $\tau_0 = 1.5 \times 10^{-14}$ s. Then, under maximum illumination,

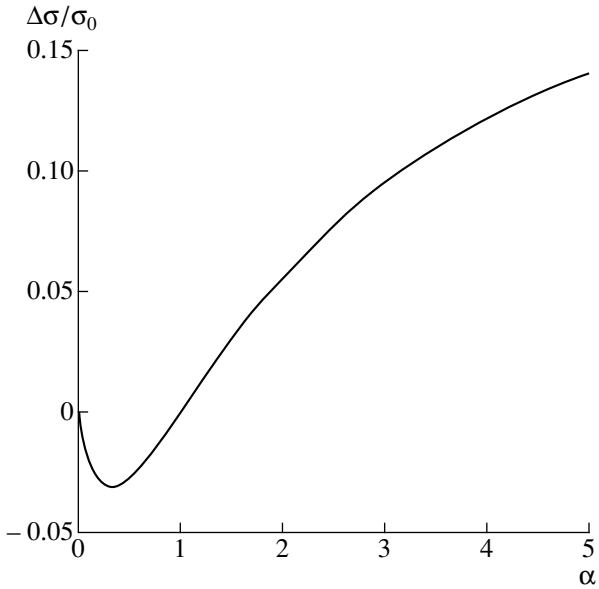

Relative change in conductivity as a function of parameter α. The scale along the ordinate axis is given in units of Δ.

Eq. (20) yields $\alpha = 2.5 \times 10^{-4}$, which corresponds to the range of low parameter values, and, consequently, the relative change in conductivity is described by formula (25). As was shown above, within an accuracy to the factor on the order of 1, the value of Δ equals the strain. In the experiments, the aluminum film was compressed, which corresponds to negative Δ. Then, it follows from (25) that within the parameter range under consideration, the conductivity of the sample will increase proportionally to the intensity of the light radiation, which is confirmed experimentally.

We now determine the relative change in conductivity for the maximum illumination of the film. Substituting the values of parameters $\Delta \simeq 6 \times 10^{-1}$ and $\alpha = 2.5 \times 10^{-4}$ into (25), we obtain $\frac{\Delta\sigma}{\sigma} \simeq 3.8 \times 10^{-7}$. The experimental value is somewhat lower, 2×10^{-7}. The difference between the theoretical estimates and the experimental data (almost two times greater) is associated with the fact that our model takes into account only one mechanism of electron scattering in the bulk, whereas the scattering in the surface film is ignored.

The theory developed above shows that a number of practical applications of the phenomenon are possible.

First, the study of the effect of irradiation on conductivity yields information on the anisotropy of the Fermi surface and on its relation to the sample deformation. As was already indicated, the calculated anisotropy of the isoenergetic surfaces under small deformations is of the same order of magnitude as the strain of the sample. Measuring the relative change in conductivity under various deformations, we can directly determine the dependence $\Delta(\xi)$. The formulas obtained in the present study can be quite useful despite the fact that they were derived for a simplified model.

When designing detectors based on the effect under study, it is expedient to measure α. Using formula (24), one can readily show that at $\alpha = 1$, the relative change in conductivity is zero. Varying the constant field, inducing a current in the film, and maintaining constant film illumination, the ratio $\Delta\sigma/\sigma_0$ can be reduced to zero. Then, the intensity of the incident radiation is simply calculated by (20) as

$$I = \frac{c}{8\pi} E_0^2 (1 + (\omega\tau_0)^2). \quad (29)$$

It should be emphasized that the calculation of the final result does not require knowledge of the anisotropy value.

ACKNOWLEDGMENTS

The author is grateful to A.M. Dykhne for fruitful discussion of the results and V.V. Ragul'skiĭ for useful information and valuable remarks.

REFERENCES

1. V. V. Ragul'skiĭ, Dokl. Akad. Nauk **349**, 38 (1996) [Phys.–Dokl. **41**, 284 (1996)].
2. O. Madelung, *Introduction to Solid State Theory* (Springer-Verlag, Berlin, 1978; Fizmatgiz, Moscow, 1980).
3. S. C. Hunter and F. R. N. Nabarro, Proc. R. Soc. London, Ser. A **220** (1953).
4. *Handbook of Electrical Engineering* (Mosk. Énergetich. Inst., Moscow, 1995), Vol. 1.
5. G. P. Motulevich, Tr. Fiz. Inst. Akad. Nauk **55** (1971).

Translated by T. Galkina

Doklady Physics, Vol. 46, No. 1, 2001, pp. 41–44. Translated from Doklady Akademii Nauk, Vol. 376, No. 1, 2001, pp. 44–47.

MECHANICS

Resonance Domains for the Hill Equation with Allowance for Damping

A. P. Seyranian

Presented by Academician A.Yu. Ishlinskiĭ April 21, 2000

Received April 26, 2000

In this paper, resonance domains for the Hill equation with allowance for damping are found using formulas for derivatives of a monodromy matrix with respect to parameters [1, 2]. The problem is solved by the asymptotic method for small amplitudes of an exciting force and a low damping coefficient. A description of these domains (represented by halves of cones) in a three-dimensional parameter space is given.

1. We consider a system of linear differential equations

$$\dot{x} = Gx, \tag{1}$$

where $G = G(t, p)$ is an m-dimensional real square matrix smoothly depending on the vector of actual parameters $p = (p_1, p_2, \ldots, p_n)$, which is a continuous periodic function of time $G(t, p) = G(t + T, p)$, where T is a period. We denote linear independent solutions to system (1) as $x_1(t), x_2(t), \ldots, x_m(t)$ and use them to form a fundamental matrix $X(t) = [x_1(t), x_2(t), \ldots, x_m(t)]$. This matrix, satisfying the equations

$$\dot{X} = CX, \quad X(0) = I, \tag{2}$$

where I is the m-dimensional identity matrix, is called the matriciant, and the matrix $F = X(T)$ is called the monodromy matrix [3].

Along with Eqs. (2), we consider a conjugate system of equations for the matrix Y:

$$\dot{Y} = -G^{\mathrm{T}}Y, \quad Y(0) = I. \tag{3}$$

The solutions $X(t)$ and $Y(t)$ to Eqs. (2) and (3) are linked by the equation [3]

$$X^{\mathrm{T}}(t)Y(t) = I, \tag{4}$$

which allows us to write out $Y(t) = (X^{\mathrm{T}}(t))^{-1}$.

We now take an increment of the vector of the parameters in the form $p = p_0 + \Delta p$. Hereupon, the matrix G and, therefore, $X(t)$ have increments as well. This correspondingly leads to a change in the monodromy matrix F. The formulas for the first and second derivatives of the monodromy matrix with respect to the parameters were found in [1, 2] in the form of integrals over period T:

$$\frac{\partial F}{\partial p_k} = F_0\int_0^T Y_0^{\mathrm{T}}\frac{\partial G}{\partial p_k}X_0 dt, \quad k = 1, \ldots, n; \tag{5}$$

$$\begin{aligned}\frac{\partial^2 F}{\partial p_i \partial p_j} = F_0\Bigg[&\int_0^T Y_0^{\mathrm{T}}\frac{\partial^2 G}{\partial p_i \partial p_j}X_0 d\tau \\ &+ \int_0^T Y_0^{\mathrm{T}}\frac{\partial G}{\partial p_i}X_0\left(\int_0^\tau Y_0^{\mathrm{T}}\frac{\partial G}{\partial p_j}X_0 d\zeta\right)d\tau \\ &+ \int_0^T Y_0^{\mathrm{T}}\frac{\partial G}{\partial p_j}X_0\left(\int_0^\tau Y_0^{\mathrm{T}}\frac{\partial G}{\partial p_i}X_0 d\zeta\right)d\tau\Bigg],\end{aligned} \tag{6}$$

$$i, j = 1, 2, \ldots, n,$$

where the zero subscript implies that the corresponding value is taken for $p = p_0$. Note that in calculating derivatives (5) and (6), it is necessary to know only the matriciants $X_0(t)$, $Y_0^{\mathrm{T}}(t) = X_0^{-1}(t)$, and the derivatives of the matrix G with respect to the parameters taken at $p = p_0$. Using derivatives (5) and (6), the variation of the monodromy matrix can be written out in the form

$$\begin{aligned}F(p_0 + \Delta p) = F_0 &+ \sum_{k=1}^{n}\frac{\partial F}{\partial p_k}\Delta p_k \\ &+ \frac{1}{2}\sum_{i,j=1}^{n}\frac{\partial^2 F}{\partial p_i \partial p_j}\Delta p_i \Delta p_j + \ldots\end{aligned} \tag{7}$$

With the known derivatives of the monodromy matrix, we can calculate its value in the vicinity of the point p_0 and, thus, estimate the behavior of the multipliers (the eigenvalues of the monodromy matrix) responsible for the stability of system (1) in the case of variation of the problem parameters.

Institute of Mechanics, Moscow State University, Michurinskiĭ pr. 1, Moscow, 117192 Russia

1028-3358/01/4601-0041$21.00

2. We consider the Hill equation with damping [4]

$$\ddot{y} + \beta\dot{y} + [\omega^2 + \varepsilon\varphi(t)]y = 0, \tag{8}$$

where $\varphi(t)$ is a continuous periodic function of time with a period 2π.

We seek instability domains for the trivial solution $y \equiv 0$ (the domains of parametric resonance) in the case of small excitation amplitude ε, low damping coefficient β, and arbitrary eigenfrequency $\omega \neq 0$. For this purpose, we represent Eq. (8) in the form of (1), taking into account that

$$x = \begin{pmatrix} y \\ \dot{y} \end{pmatrix}, \quad G(t, p) = \begin{bmatrix} 0 & 1 \\ -\omega^2 - \varepsilon\varphi(t) & -\beta \end{bmatrix}. \tag{9}$$

This system of equations contains three parameters $p = (\varepsilon, \beta, \omega)$. If we assume in (8) and (9) that $\varepsilon = 0$, $\beta = 0$, then from (2) and (3), it is easy to find the matriciants

$$X_0(t) = \begin{bmatrix} \cos\omega t & \omega^{-1}\sin\omega t \\ -\omega\sin\omega t & \cos\omega t \end{bmatrix},$$
$$Y_0(t) = \begin{bmatrix} \cos\omega t & \omega\sin\omega t \\ -\omega^{-1}\sin\omega t & \cos\omega t \end{bmatrix}. \tag{10}$$

Note that in accordance with (4), $X_0^{\mathrm{T}}(t)Y_0(t) = I$. Thus, for $\varepsilon = 0$, $\beta = 0$ the monodromy matrix takes the form

$$F_0 = X_0(2\pi) = \begin{bmatrix} \cos 2\pi\omega & \omega^{-1}\sin 2\pi\omega \\ -\omega\sin 2\pi\omega & \cos 2\pi\omega \end{bmatrix}. \tag{11}$$

The eigenvalues (multipliers) of this matrix are

$$\rho_{1,2} = \cos 2\pi\omega \pm i\sin 2\pi\omega. \tag{12}$$

For all $\omega \neq k/2$, $k = 1, 2, \ldots$, the multipliers are complex conjugate quantities lying in a unit circle (stability state). For $\beta = 0$, system (8) is Hamiltonian in character. This implies that simple multipliers cannot leave the unit circle when changing parameters ω and ε [3]. It can be shown that introducing damping ($\beta > 0$) results in asymptotic stability of the system.

To do this, we find the approximate value of the monodromy matrix F using relations (5), (7), and (9)–(11). With an accuracy to terms on the order of β, we obtain

$$F = F_0(I + A\beta), \tag{13}$$

where F_0 is defined in (11), I is the identity matrix, and

$$A = \begin{bmatrix} \dfrac{\sin 4\pi\omega}{4\omega} - \pi & \dfrac{\sin^2 2\pi\omega}{2\omega^2} \\ \dfrac{\sin^2 2\pi\omega}{2} & -\dfrac{\sin 4\pi\omega}{4\omega} - \pi \end{bmatrix}. \tag{14}$$

From (13) and (14) we find that

$$\det F = \det F_0 \det(I + A\beta)$$
$$= 1 + \beta\,\mathrm{Tr}A + o(\beta) = 1 - 2\pi\beta + o(\beta). \tag{15}$$

Since the determinant of the monodromy matrix is equal to the product of the pair of the complex conjugate multipliers, then for rather small $\beta > 0$, it follows from (15) that $|\rho_{1,2}| < 1$; this implies asymptotic stability.

Therefore, instability (resonance) can arise only in the vicinity of the points

$$p_0\colon\ \varepsilon = 0, \quad \beta = 0, \quad \omega = \frac{k}{2}, \quad k = 1, 2, \ldots, \tag{16}$$

at which the multipliers are double.

To find the domains of a parametric resonance, we expand the monodromy matrix F into a Taylor series with respect to parameters ε, β, and $\Delta\omega = \varepsilon - k/2$ in the vicinity of the points p_0:

$$F(p) = F(p_0) + \frac{\partial F}{\partial\varepsilon}\varepsilon + \frac{\partial F}{\partial\beta}\beta + \frac{\partial F}{\partial\omega}\Delta\omega + \ldots \tag{17}$$

According to formulas (5) and using (9)–(11), we calculate the derivatives $\dfrac{\partial F}{\partial\varepsilon}$, $\dfrac{\partial F}{\partial\beta}$, and $\dfrac{\partial F}{\partial\omega}$ for $p = p_0$. As a result, with an accuracy to the terms of the first order of smallness, we have

$$F(p) = \cos\pi k$$
$$\times \begin{bmatrix} 1 + 2\pi a_k\varepsilon - \pi\beta & \dfrac{4\pi}{k}(\Delta\omega + (c_k - b_k)\varepsilon) \\ -k\pi(\Delta\omega + (c_k + b_k)\varepsilon) & 1 - 2\pi a_k\varepsilon - \pi\beta \end{bmatrix}. \tag{18}$$

Here, for the coefficients, we introduced the notation

$$a_k = \frac{1}{2\pi k}\int_0^{2\pi}\varphi(t)\sin kt\,dt,$$
$$b_k = \frac{1}{2\pi k}\int_0^{2\pi}\varphi(t)\cos kt\,dt, \quad c_k = \frac{1}{2\pi k}\int_0^{2\pi}\varphi(t)\,dt. \tag{19}$$

Thus, they are directly related to the coefficients of the Fourier series for the periodic function $\varphi(t)$.

The multipliers for the matrix (18) can be found approximately as

$$\rho_{1,2} = (-1)^k(1 - \pi\beta) \pm 2\pi\sqrt{D}, \tag{20}$$

$$D = r_k^2\varepsilon^2 - (\Delta\omega + c_k\varepsilon)^2, \quad r_k = \sqrt{a_k^2 + b_k^2}. \tag{21}$$

The system is unstable if the absolute value, at least for one multiplier, exceeds unity [3]. This condition is fulfilled for $\beta < 0$, and the system becomes unstable. But in the case of $\beta \geq 0$, this condition is satisfied only when

$2\pi\sqrt{D} > \pi\beta$. Hence, using (21), we find that the domain of parametric resonance lies inside the half of the cone,

$$\left(\omega - \frac{k}{2} + c_k\varepsilon\right)^2 + \frac{\beta^2}{4} < r_k^2\varepsilon^2, \quad \beta \geq 0, \tag{22}$$

adjoining the half-space $\beta < 0$, see Fig. 1. Assuming that $\beta = 0$ in (22), we find the domains of parametric resonance in the absence of damping:

$$-c_k - r_k < \frac{\omega - k/2}{\varepsilon} < -c_k + r_k. \tag{23}$$

Intersecting the domain (22) by the plane $\varepsilon = \text{const}$, we deal with the half of an ellipse having semiaxes $|\omega - \omega_0| = r_k\varepsilon$, $\omega_0 = k/2 - c_k\varepsilon$, and $\beta = 2r_k\varepsilon$, the centers of the ellipses lying on the axis $\omega = k/2 - c_k\varepsilon$, see Figs. 1, 2. Note that with increasing damping coefficient β, the width of the resonance domain over the frequency ω decreases and for $\beta > 2r_k\varepsilon$, disappears altogether.

The cross section of the half-cone (22) by the plane $\beta = \text{const}$, $\beta \geq 0$ yields domains of parametric resonance limited by two hyperbolas, see Fig. 3. Their asymptotes are found from inequalities (23). In the case of damping ($\beta > 0$), according to (22), the minimum (in its absolute value) amplitude needed for the excitation of the resonance is $|\varepsilon|_{\min} = \beta/(2r_k)$, and the appropriate resonance frequency is shifted from the value $k/2$ by $-c_k\varepsilon$ (Fig. 3). With an increase in resonance number k, the coefficients r_k and c_k tend to zero. This implies that with increasing k, the cone axis (22) approaches the vertical line and the cone, in itself, narrows. Note that if the average value of the periodic function is zero ($c_k = 0$), the axes of the cones are vertical lines for all k and the resonance domains are symmetric with respect to the planes $\omega = k/2$.

For $\beta = 0$ and $c_k = 0$, we find from (23) the resonance domains for the Hill equation without damping and with a zero average value of the periodic function $\varphi(t)$ [5]. Assuming in (8) that $\beta = 0$, $\varphi(t) = \cos t$, we arrive at the Mathieu equation. In this case, we find from (19), for the domain of the first resonance, that $k = 1$, $a_1 = 0$, $b_1 = r_1 = 1/2$, $c_1 = 0$, and we obtain from (23) the well known relation $1 - \varepsilon < 2\omega < 1 + \varepsilon$ [4, 5].

The above-presented method for analysis of parametric-resonance domains using derivatives of the monodromy matrix is simpler and more evident compared to methods based on searching for periodic solutions at the boundaries of stability domains [4–6].

3. We now consider as an example a pendulum with a suspension point vibrating vertically in accordance with the law

$$z = a\phi(\Omega t), \tag{24}$$

where a is the amplitude, $\phi(\tau)$ is a periodic function with a period 2π, and Ω is the excitation frequency. We investigate the stability of the lower equilibrium posi-

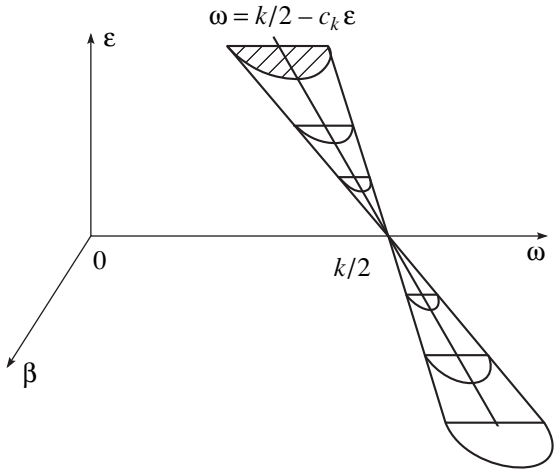

Fig. 1. Parametric-resonance domains.

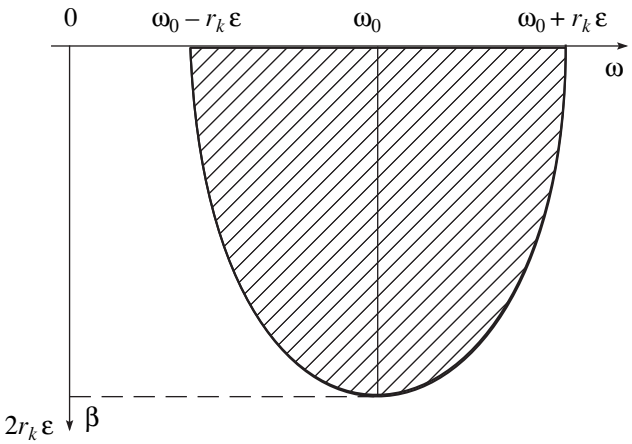

Fig. 2. Cross section of the resonance domain by the plane $\varepsilon = \text{const}$.

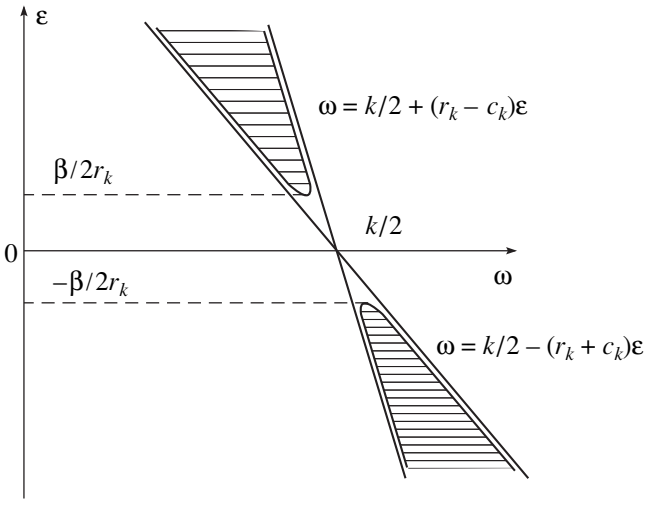

Fig. 3. Cross section of the resonance domain by the plane $\beta = \text{const}$.

tion of the pendulum depending on the frequency Ω and small quantities, such as the amplitude a and the damping coefficient γ.

The linearized equation of motion for the pendulum with allowance for damping has the form [4]

$$ml\ddot{\theta} + \gamma l\dot{\theta} + m(g - \ddot{z})\theta = 0, \quad (25)$$

where θ is the pendulum deviation angle measured from the equilibrium position, m is the pendulum mass, l is the length, and g is the acceleration of gravity. According to (24), we have $\ddot{z} = a\Omega^2\ddot{\phi}(\Omega t)$. Substituting this expression into (25) and introducing notation $\tau = \Omega t$, $\varphi(\tau) = -\ddot{\phi}(\tau)$, we transform Eq. (25) to a form similar to (8):

$$\frac{d^2\theta}{d\tau^2} + \frac{\gamma}{\Omega m}\frac{d\theta}{d\tau} + \left[\frac{g}{\Omega^2 l} + \frac{a}{l}\varphi(\tau)\right]\theta = 0. \quad (26)$$

It follows from the results of Section 2 that for small excitation amplitude a and damping coefficient γ, the lower equilibrium position of the pendulum becomes unstable at excitation frequency Ω close to critical values:

$$\Omega_k = \frac{2}{k}\sqrt{\frac{g}{l}}, \quad k = 1, 2, \ldots \quad (27)$$

In this case, according to (22), the instability domains (domains of the parametric resonance) are determined by the semicone

$$\left[\frac{k}{2}\left(1 - \frac{\Omega}{\Omega_k}\right) + \frac{c_k a}{l}\right]^2 + \frac{\gamma^2}{4\Omega_k^2 m^2} < \frac{r_k^2 a^2}{l^2}, \quad \gamma \geq 0, \quad (28)$$

where Ω_k is defined in (27) and the coefficients c_k and r_k related to the periodic function $\varphi(\tau)$ are found from expressions (19), (21). Formula (28) can be transformed to the form

$$\left(1 - \frac{\Omega}{\Omega_k} + \frac{2c_k a}{kl}\right)^2 + \frac{\gamma^2 l}{4gm^2} < \frac{4r_k^2 a^2}{k^2 l^2}. \quad (29)$$

From this expression, it is easy to see how rapidly the instability cone becomes more narrow and straight with increasing k. Inequality (29) becomes even more simple for the zero mean value of the periodic function ($c_k = 0$).

ACKNOWLEDGMENTS

This work was performed under the financial support of the International Russian–Chinese Research Foundation, project no. 99-01-39129.

REFERENCES

1. A. P. Seyranian, F. Solem, and P. Pedersen, Arch. Appl. Mech. **69**, 160 (1999).
2. A. P. Seyranian, F. Solem, and P. Pedersen, J. Sound Vibr. **229**, 89 (2000).
3. V. A. Yakubovich and V. M. Starzhinskiĭ, *Parametric Resonance in Linear Systems* (Nauka, Moscow, 1987).
4. D. R. Merkin, *Introduction to the Theory of Stable Motion* (Nauka, Moscow, 1987).
5. I. G. Malkin, *Certain Problems of Nonlinear-Vibration Theory* (Gostekhteorizdat, Moscow, 1956).
6. A. H. Nayfeh, *Introduction to Perturbation Techniques* (Wiley, New York, 1981; Mir, Moscow, 1984).

Translated by A. Seyranian

Doklady Physics, Vol. 46, No. 1, 2001, pp. 45–49. Translated from Doklady Akademii Nauk, Vol. 376, No. 1, 2001, pp. 48–52.

MECHANICS

On Supersonic Jet Collision

I. V. Simonov

Presented by Academician A.Yu. Ishlinskiĭ April 27, 2000

Received April 28, 2000

1. We consider the plane and axisymmetric problem of the supersonic symmetric collision of two infinite jets of different condensed materials. Previously, a similar problem of subsonic collision in hydrodynamic approximation was analyzed by M.A. Lavrent'ev [1]. In the problem formulation considered here, both compressibility and thermodynamic phenomena are essential, although, similar to [1], we ignore the effects of the strength, heat conduction, and viscosity. It is worth noting that allowance for these effects in the numerical simulation of the collision of equivalent metal jets [2] did not result in significant corrections to the data obtained in [1]. To describe the jet collision as a steady-state flow of a compressible inhomogeneous fluid with its temperature taken into account, we use the so-called incomplete equations of state for solids and liquids under high pressures (the Mie–Grüneisen-type and Tillotson-type equations [3–6]), which describe the dependence of the specific internal energy E on pressure P and specific volume V [or $P = P(E, V)$].

A flow configuration is shown in the figure, where L_1, L_2, and L are the free surfaces of jets 1 and 2 and the interface, respectively. In addition, A'AA" and B'BB" are the fronts of detached shock waves and the points $x = 0$, x_A, and x_B are the positions of the contact discontinuity and the wave fronts on the symmetry axis x. The relative collision velocity is U_0. The flow ahead of the wave fronts is unperturbed: the jet radii (half-thicknesses) r_i, the mass-velocity magnitudes along the flow axis D_i (or, which is the same, the wave-front velocities in the corresponding laboratory coordinate systems), the specific volumes V_i, and the temperatures T_i are constant, the constant pressure being $P_i = 0$ ($i = 1, 2$).

Following [1] and omitting the details of the flow description, we consider flow principal characteristics, namely, the maximum values of the thermodynamic functions at the wave fronts and at the stagnation point $x = 0$, the relative penetration velocity, etc.

The conventional laws of conservation and continuity are also valid at shocks and the interface. In contrast to gas dynamics [7], the shock fronts in dense media are formed at relatively long distances from the interface, and, therefore, the Newtonian approximation of a thin shock layer becomes invalid. Thus, assuming an isentropic nature for the additional loading behind the wave fronts, we can use the Bernoulli integral for a compressible fluid to link the thermodynamic functions at the points A and B of the wave fronts with their values to the left and to the right of the stagnation point $x = \pm 0$ to arrive at the following closed system of eleven algebraic and "integro-algebraic" equations with respect to eleven unknowns [P and V at the singular points x_A, x_B, and $x = \pm 0$; and also wave-front (D_i) and mass (U_{+i}) velocities behind the fronts ($i = 1, 2$)]:

$$U = D_i, \quad P = E = 0, \quad V = V_i, \quad T = T_i, \quad x < x_A \cup x < x_B, \quad U_0 = D_1 + D_2, \tag{1}$$

$$P_+ = \frac{D(D - U_+)}{V_0} = \frac{U_+(D - U_+)}{V_+} = P_H(V_+), \quad E_+ = \frac{P_+}{2}(V_0 - V_+), \tag{2}$$

$$P_{*1} = P_{*2} \equiv P_* = P_{Si}(V_{*i}, V_{i+}), \quad U_{*1} = U_{*2} = 0, \tag{3}$$

$$P_* V_* - P_+ V_+ - \frac{U_+^2}{2} + J(V_*, V_+) = 0, \tag{4}$$

$$J(V_*, V_+) = \int_{V_*}^{V_+} P_S(V, V_+)dV = E_S(V_*, V_+) - E_S(V_+, V_+), \tag{5}$$

$$E = E(P, V), \quad P_S = -\left(\frac{dE}{dV}\right)_S, \quad P_H(V): \ (V - V_0)P_H = E(P_H, V). \tag{6}$$

The subscripts + and * indicate the function values immediately behind the wave fronts and at the point $x = 0$ at the interface, respectively; subscripts 1 and 2 indicate the material parameters of the jets to the left

Institute for Problems in Mechanics,
Russian Academy of Sciences,
pr. Vernadskogo 101, Moscow, 117526 Russia

1028-3358/01/4601-0045$21.00

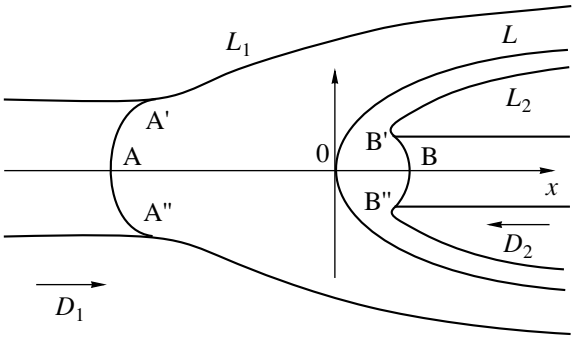

Diagram of steady flow for supersound-jet collision.

and to the right of the interface, respectively (these subscripts are omitted in the cases where it does not lead to any ambiguities); $P_H(V)$ and $P_S(V, V_+)$ are the Hugoniot curves and the isentropes originated at the points $V_0 = V_i$ and V_+, respectively; and the magnitudes of the mass velocities U are calculated in a stationary coordinate system, where the discontinuity surfaces are immobile. Isentropes are calculated with the invocation of thermodynamic relationships.

Once the system (1)–(6) is solved, the maximum temperatures attained on both sides of the stagnation point 0 are determined by summing the T_+ value at the shock front and an increment along the corresponding isentrope behind the front using the thermodynamic relation

$$\frac{dT}{T} = \frac{dS}{c_V} - \Gamma\frac{dV}{V}. \tag{7}$$

Under the assumption that T_i have low values (close to room temperature), the above equation together with the equation for entropy S at the adiabat (see [3]) yields the following equation for T_+:

$$\frac{dT}{dV} + \frac{\Gamma}{V}T = \frac{1}{2}\frac{V_0 - V}{c_V}\frac{dP_H}{dV} + \frac{1}{2}P_H, \tag{8}$$
$$V_+ \le V < V_0; \quad T = T_0, \quad V = V_0.$$

Here, c_V is the specific heat at a constant volume, $\Gamma = \Gamma(V, T)$ is the Grüneisen function [3–5], and $T_0 = T_i$; it is also assumed that T_i are on the order of room temperature. Both temperature distribution behind the fronts, $T = T(V)$, and its maximum values, T_{*i}, are determined by integrating (7) under the condition that $dS \equiv 0$ and the initial conditions $T = T_{+i}$ and $V = V_{+i}$.

2. We now analyze the semi-inverse method of solving the problem. Instead of the collision velocity U_0, we set one of the wave-front velocities D. The corresponding value U_0 is determined *a posteriori*. Then, coupled equations (1)–(8) are split and its solution is reduced to calculations using formulas (1) and (2), determination of the roots of nonlinear equations (3)–(6) with only one unknown, and the solution of ordinary differential equations (7) and (8).

Connecting the states at the points $x = \pm 0$ with the corresponding states at infinity, we can write out the Bernoulli integral at each side of the contact discontinuity. Transforming this integral with due regard for the shock conditions and determining integral (4), we arrive at the following expression for velocities along L at infinity:

$$U_\infty = D - 2\{E_H(V_+, V_0) - E_S(V_+, V_0)\},$$
$$E_S(V_+, V_0) = \int_{V_+}^{V_0} P_S(V, V_0)dV,$$

where $E_S(V_+, V_0)$ is the increment in the specific internal energy along the isentrope originating at point V_0 within the interval $V_+ < V < V_0$. Since the difference between the increments in the specific energies calculated along the Hugoniot curve and the isentrope in braces is positive at the same compressibilities, the velocities of the particles at infinity along the interface are lower than along the free surfaces, L_i, where they are equal to D_i. This is one of the differences of our model from that described in [1].

Assuming that in (1)–(8) $P_{+i} = 0$, $V_{+i} = V_i$, $U_{+i} = -D_i$, and $T_{+i} = T_i$ ($i = 1$, $i = 2$, or $i = 1, 2$), we can also study the subsonic regimes (the point $x = x_A$, $x = x_B$, or both these points move away to infinity). This method can also be extended to the case of jumpwise phase transitions in material 1 or material 2 or in both materials simultaneously upon the introduction of additional discontinuity surfaces and setting the conditions for such transitions at these surfaces and conventional relations at the discontinuities. However, if the medium undergoes such phase transitions only at the wave front without wave decomposition, calculation can still be performed by (1)–(8). At $r_1 = \infty$, we arrive at the pattern of an unbounded flow of material 1 around jet 2. If the materials are equivalent, the thermodynamic functions along the x-axis are symmetric with respect to the stagnation point within the accuracy of similarity transformation of one of the x-semiaxis. In other words, these functions attain the same values at the wave fronts and at the stagnation point. The distributions of these values as a function of any of them chosen to be an independent variable (for example, of V) are also identical. In this case, the penetration rate of one jet (i) into another (j) equals D_i; i.e., the stagnation-point velocity in the coordinate system, where the other jet is immobile at infinity, equals half the collision velocity U_0. Moreover, similar to the Lavrent'ev model, the depth of the jet penetration, H, equals the decrease in its length L. If, in addition, the jet configurations are identical, the interface is a plane and the problem becomes equivalent to the problem of a jet impinging onto a smooth flat wall.

3. Under moderately high pressures and temperatures, the Mie–Grüneisen equation [3–5] with the temperature-independent Grüneisen function satisfactorily describes the state of the medium. Often, the dependence of this function on the specific volume is written in the approximation $\frac{\Gamma}{V} = \frac{\Gamma_0}{V_0} = \frac{\Gamma_-}{V_-}$, where $V_0 = V_i$ and $\Gamma_0 = \Gamma_i$, which correspond to the V and Γ values under the normal conditions. They are assumed to be satisfied in the unperturbed flow regions. We also consider $T_0 = T_i$. Assuming, in addition, that the Hugoniot curve $P_\mathrm{H} = P_\mathrm{H}(\Theta)$ $\left(\Theta = 1 - \frac{V}{V_0}\right)$ is experimentally determined, the equation of state and the general solution to the differential equation of an isentrope (the equation is derived in [3]) can be written out as

$$\begin{gathered} E = E_\mathrm{H}(\Theta) + \frac{V_0(P - P_\mathrm{H})}{\Gamma_0}, \\ E_\mathrm{H}(\Theta) = \frac{1}{2}\Theta V_0 P_\mathrm{H}(\Theta), \\ P_S(\Theta, \Theta^\circ) = P_\mathrm{H}(\Theta) - \frac{1}{2}\Gamma_0 \int_{\Theta^\circ}^{\Theta} \exp[\Gamma_0(\Theta - z)] \\ \times\left(z\frac{d}{dz} - 1\right)P_\mathrm{H}(z)dz. \end{gathered} \tag{9}$$

Usually, the experimental Hugoniot curves are approximated by a linear dependence of the wave-front velocity D on the jump in the mass velocity at the wave front:

$$D = C + \lambda(D - U_+). \tag{10}$$

The constants C and λ in (10) are taken to be the values C_i and λ_i related to the material i. It is convenient to introduce the following dimensionless quantities [5]:

$$\begin{gathered} p = \frac{\lambda V_0 P}{C^2}, \quad \theta = \lambda\Theta, \quad u = \frac{\lambda U}{C}, \\ t = t_0\frac{T}{T_0}, \quad t_0 = \frac{\lambda^2 c_\mathrm{V} T_0}{C^2}, \quad \gamma = \frac{\Gamma_0}{\lambda}, \end{gathered} \tag{11}$$

where c_V is constant, because the temperatures considered below exceed the corresponding Debye temperatures [3]. Initially, using Eq. (9) with due regard for Eqs. (10) and (11), we derive the expressions for dimensionless thermodynamic functions behind the front in the case of loading along the isentrope. Then, system (1)–(8) can be reduced to a simpler form,

$$\begin{gathered} p_+ \equiv p_\mathrm{H}(\theta_+) = \frac{\theta_+}{(1 - \theta_+)^2} = \mathrm{M}(\mathrm{M} - 1), \\ \theta_+ = \frac{\mathrm{M} - 1}{\mathrm{M}}, \quad \mathrm{M} = \frac{D}{C}, \end{gathered} \tag{12}$$

$$\begin{gathered} u_+ = (\lambda - 1)\mathrm{M} + 1, \quad t_+ = t_0 e^{\gamma\theta_+} + I(\theta_+, 0), \\ I(\theta, \theta_+) = \int_{\theta_+}^{\theta} \frac{z^2 dz}{(1 - z)^3} e^{\gamma(\theta - z)}; \\ \theta_*(2\lambda - \theta_*)(1 - \theta_*)^{-2} \\ - 2[1 + \gamma(\lambda - \theta_*)]I(\theta_*, \theta_+) = \lambda^2\mathrm{M}^2; \end{gathered} \tag{13}$$

$$p_* = p_\mathrm{H}(\theta_*) - \gamma I(\theta_*, \theta_+); \tag{14}$$

$$\begin{gathered} p_{*i} = \zeta_i p_{*j} \Leftrightarrow \frac{\theta_{*i}(2\gamma_i^{-1} - \theta_{*i})}{(1 - \theta_{*i})^2} \\ - 2\zeta_i(\gamma_i^{-1} + \lambda_i - \theta_{*i})p_{*j} + \lambda_i^2\mathrm{M}_i^2 = 0; \end{gathered} \tag{15}$$

$$t_* = t_+ \exp\{\gamma(\theta_* - \theta_+)\}, \quad \zeta_i = \frac{\lambda_i V_i C_j^2}{\lambda_j V_j C_i^2}, \tag{16}$$

$$i \neq j = 1, 2.$$

We now consider the algorithm for solving system of equations (12)–(16) by the above semi-inverse method for the case of two shock waves. Setting one of the values (e.g., $\mathrm{M}_2 > 1$) and using (12), we determine the corresponding values p_{+2} and θ_{+2}. Then, using Eq. (13), we determine the physically meaningful root θ_{*2} and, then, also the pressure p_{*2} by formula (14). Solving Eq. (15) ($i = 1$) with respect to M_1, we obtain the explicit form of the function $\mathrm{M}_1 = \mathrm{M}_1(\theta_{*1})$ and, with allowance for the dependence $\theta_{+1} = \frac{\mathrm{M}_1 - 1}{\mathrm{M}_1}$, also the direct relation between θ_{+1} and θ_{*1}. Substituting the functions $\theta_{+1} = \theta_{+1}(\theta_{*1})$ and $\mathrm{M}_1 = \mathrm{M}_1(\theta_{*1})$ into Eq. (13) or Eq. (14) and assuming now $i = 1$, we arrive at the equation for the dilatation θ_{*1}. Solving this equation, we determine the Mach number M_1. Then solving Eq. (12), we obtain the values of all the remaining quantities at the shockwave front A'AA". Finally, the temperature is determined from Eqs. (12) and (16), whereas the collision velocity is determined by the sum $U_0 = C_1\mathrm{M}_1 + C_2\mathrm{M}_2$. As a result, all the quantities desired are determined as functions of U_0.

If the determined value of M_1 is smaller than unity, the jet flow 1 is subsonic, the calculation of corresponding parameters should be changed by using $\mathrm{M}_1 = 1$ in Eqs. (12). Accordingly, in the subsonic flow mode, we should assume that $\mathrm{M}_1 = \mathrm{M}_2 = 1$ in the above equations. This automatically leads to the relations $p_+ = \theta_+ = 0$ and $u_+ = -\lambda$ equivalent to the conditions at infinity, which follow from (1) for infinitely remote fronts.

Table

Material	P, GPa	T, K
Fe + Fe	548	11 933
W + Fe	836	23 570
W + sand	305	62 612
Sand + sand	132	20 936
Water + water	61.8	890
Water + ice	69.3	544

Since the contact discontinuity can be replaced by a smooth wall without changing the flow outside this wall, the first part of the calculation of the flow parameters on one side of this wall is similar to the calculations in [8] of the supersonic flow around a blunt perfectly rigid body. However, in this case, the applicability of the physical model is bounded from above with respect to velocity by the actual body strength. In our formulation of the problem, the validity range of the defining relationships should be taken into account. Thus, if the temperature exceeds several tens of thousands of degrees, the Mie–Grüneisen description of the pressure and the energy should be complemented with the terms responsible for thermal excitation of electrons [4]. In turn, this can change the linear relation between the velocities at the shock (10). Since there is no experimental data for this range of pressures and temperatures, it is expedient to use theoretical intermediate defining relationships such as, e.g., the Tillotson equation [6] continuously relating the space of states where the approximation of the Hugoniot curve (10) is valid with the Thomas–Fermi model for electron gas at superhigh pressures and temperatures [4].

4. For velocities up to $U_0 \approx 20$ km/s, system (12)–(16) has been solved numerically for different combinations of the following materials: iron (Fe), $\rho_0 = \frac{1}{V_0} = 7.68$ g/cm^3, $C = 3.8$ km/s, $\lambda = 1.58$; tungsten (W), $\rho_0 = 19$ g/cm^3, $C = 4.029$ km/s, $\lambda = 1.237$; dry sand, $\rho_0 = 1.6$ g/cm^3, $C = 1.7$ km/s, $\lambda = 1.31$; water, $C = 1.48$ km/s, $\lambda = 1.60$, $T_0 = 273$ K; and the high-pressure phase of ice, $\rho_0 = 1.293$ g/cm^3, $C = 1.28$ km/s, $\lambda = 1.56$, $T_0 = 263$ K. The above parameters were averaged throughout the pressure range observed in the experiments on shock compression, the possible phase transitions being ignored. The data for tungsten and other materials were taken from [9] and [6], respectively. The temperature T_0 was taken to be 300 K for all the materials except ice and water.

For different pairs of the materials, the maximum pressures and temperatures obtained at $U_0 = 20$ km/s are presented in the table. It is seen that the temperatures are such that no extrapolation of the defining relationships to higher velocities is any longer possible.

The shape of the curves describing the maximum pressures and temperatures at the wave fronts and at the interface as functions of the collision velocity is typical of all the pairs of materials under consideration.

At the point of the transition to the supersonic mode, the curves of the maximum pressures and temperatures at the wave fronts and the interface as functions of the collision velocity have no discontinuities. The jumps are observed only for the derivatives of the functions corresponding to the wave fronts. The curve shapes are characteristic of all the pairs of the materials. However, the curves also exhibit certain differences. In metals, the values of P and T, which are calculated behind the front and at the stagnation point, become closer at a higher collision velocity. For example, for the pair Fe + Fe at $U_0 \approx 20$ km/s, we have $\frac{P_+}{P_*} > \frac{1}{2}$ and $\frac{T_+}{T_*} \approx 0.87$. The situations for water being in different states are quite different: in this case, the additional loading behind the front continues to be the main factor of the pressure at the stagnation point in the calculated range of velocities. The presented data show that the temperature increase in both water and ice is much weaker than in metals.

Surprisingly, the penetration velocities and, therefore, also the ratio between the depth H of penetration of one jet into the other and its length L are in rather good agreement with the calculations by the Lavrent'ev formulas for incompressible fluids with different densities ρ_1 and ρ_2 [1]. According to these formulas, $\frac{H}{L} = \eta$ and $\eta = \sqrt{\frac{\rho_2}{\rho_1}}$, where it was assumed that a thin jet penetrates into a thick one (see the figure). For the ice–water pair, the $\frac{H}{L}$ ratio first increases with the velocity and attains maximum value at $U_0 = 4.24$ km/s, which only differs from η by 3.5%, and, then, slowly decreases, always being, however, higher than this nominal value. For pairs of materials characterized by more contrasting properties, this difference, of course, increases. Thus, the relative penetration depth of a tungsten rod into sand, first, noticeably decreases to a minimum at $U_0 = 8.28$ km/s, with the latter being lower by ~17.7% than the value obtained from the Lavrent'ev formula. Upon passing by the minimum, the penetration depth slowly increases, remaining lower by ~12% than this value calculated at $U_0 = 20$ km/s.

The effect of different compressibilities of the materials is seen from the estimate of the $\frac{H}{L}$ ratio, which

was calculated by substituting $p_H(\theta_*) = p_{S*}(\theta_*) + O(\theta_*^3)$ into Eqs. (13) ($i = 1, 2$) at $\theta_* \ll 1$:

$$\frac{H}{L} = \frac{D_2}{D_1} \approx \left\{\frac{1 + \rho_1/\rho_{*1}}{1 + \rho_2/\rho_{*2}}\frac{\rho_2}{\rho_1}\right\}^{1/2}, \quad \theta_{*i} \ll 1.$$

It should be emphasized that the stagnation pressure is always higher than that predicted by the Lavrent'ev formula. For the tungsten + sand pair, where this effect is the most pronounced, the relative excess in pressure ranges from 31 to 37% in the velocity range from $10 \le U_0 \le 20$ km/s.

It can be shown that the contribution of the heat-induced pressure is rather low despite the attained high temperatures ($T_* \sim 10^4$ K). The compressibility $\frac{\rho_*}{\rho_0}$ at $U_0 = 20$ km/s attains the values 1.89 for Fe + Fe, 1.32 for water + water, and 3.00 for sand + sand. The overly high compressibility for sand is associated with a drastic increase in its density in the quartz–stishovite-type phase transitions [6].

ACKNOWLEDGMENTS

This study was supported by the Russian Foundation for Basic Research, project no. 99-01-01265.

REFERENCES

1. M. A. Lavrent'ev, Usp. Mat. Nauk **12** (4), 41 (1957).
2. F. H. Harlow and F. E. Pracht, Phys. Fluids **9**, 1951 (1966).
3. R. Killer and E. Rois, in *Physics of High Energy Densities*, Ed. by P. Caldirola and H. Knoepfel (Academic, New York, 1971; Mir, Moscow, 1974).
4. Ya. B. Zel'dovich and Yu. P. Raizer, *Elements of Gas Dynamics and Classical Theory of Shock Waves* (Nauka, Moscow, 1966; Academic, New York, 1968).
5. F. E. Prieto and C. Renero, J. Phys. Chem. Solids **37**, 151 (1976).
6. H. J. Melosh, *Collision Cratering: A Geologic Process* (Clarendon Press, New York, 1989; Mir, Moscow, 1994).
7. A. Ya. Sagomonyan, Vestn. Mosk. Univ., Ser. 1: Mat. Mekh., No. 4, 99 (1967).
8. I. V. Simonov, Int. J. Impact Eng. **20** (6/10), 743 (1997).
9. *High Velocity Collision Phenomena*, Ed. by R. Kinslow (Academic, New York, 1971; Mir, Moscow, 1973).

Translated by Yu. Verevochkin

Doklady Physics, Vol. 46, No. 1, 2001, pp. 50–51. Translated from Doklady Akademii Nauk, Vol. 376, No. 1, 2001, pp. 53–54.

MECHANICS

A Model for Fragmentation of a Meteoroid in the Atmosphere

V. P. Stulov and L. Yu. Titova

Presented by Academician V.V. Rumyantsev April 7, 2000

Received April 10, 2000

Researchers' attention to the problems of motion of small celestial bodies entering into the atmosphere have recently promoted a certain progress in this field of science. Thus, several models for body fragmentation caused by aerodynamic drag were proposed [1–4]. In most cases, calculation of the trajectories for fragments of a body was performed by numerical integration. The model proposed in [4] allows for the effect of body size on the disintegration process. In this case, the properties of a swarm of particles along a body's trajectory is calculated with the help of the step-by-step method for each two subsequent acts of disintegration whose number attains several tens.

In this paper, we present a simple modification of the model [4] in which the description of the disintegration process is based on a variable corresponding to the midsection area for a certain effective body. In the framework of this modification, the motion, under the assumptions suggested in [4], is described by a differential equation with separable variables. The model of stepwise calculation, in fact, is a specific difference approximation for this differential equation. Moreover, a simple generalization taking into account the body's ablation is admissible: the mass transfer equation must contain the same variable corresponding to the midsection area.

According to [4], the characteristic size of a fragment after a kth disintegration is expressed by the formula

$$R_k = \frac{R_e}{2^{k/3}}, \tag{1}$$

where R_e is the characteristic size of a parent body. The condition for the kth disintegration is written out in [4] as

$$\rho_a^2 V_k^4 = \frac{3\gamma_* E}{R_e} \times 2^{(k-1)/3}. \tag{2}$$

Here, $2\gamma_*$ is the specific (i.e., per unit area) fracture energy [4], E is the Young's modulus, ρ_a is the atmospheric density, and V_k is the body's velocity at the moment of the kth disintegration.

Finally, the total midsection area under the condition of independent motion of the fragments is expressed by the formula

$$A_k = \pi R_e^2 \times 2^{k/3}. \tag{3}$$

Excluding k from expressions (2) and (3) and omitting subscript k, we obtain the following expression for the midsection area variable:

$$a = \frac{A}{A_e} = 2^{1/3} \rho_a^2 V^4 \frac{R_e}{3\gamma_* E}. \tag{4}$$

For brevity, we use the notation $\sigma_*^2 = \dfrac{3\gamma_* E}{R_e}$.

We now write out the dimensionless equations for deceleration and carrying out of the mass in the form

$$m\frac{dv}{dy} = \alpha\rho v a, \quad \frac{dm}{dy} = 2\alpha\beta\rho v^2 a,$$
$$\alpha = \frac{1}{2} c_d \frac{\rho_0 h_0 A_e}{M_e \sin\gamma}, \quad \beta = \frac{1}{2}\frac{c_h V_e^2}{c_d H^*}. \tag{5}$$

Here, the trajectory angle γ, drag coefficient c_d, and mass transfer coefficient c_h, as well as the evaporation enthalpy H^*, are constant quantities. The values of the velocity V, body mass M, and midsection area A are normalized to values corresponding to their entry into the atmosphere, which are denoted by the subscript "e." The altitude h and the density ρ_a are normalized to altitude h_0 of the uniform atmosphere and density ρ_0 at $h = 0$, respectively; i.e., $v = \dfrac{V}{V_e}$, $m = \dfrac{M}{M_e}$, $a = \dfrac{A}{A_e}$, $y = \dfrac{h}{h_0}$, and $\rho = \dfrac{\rho_a}{\rho_0}$. The first disintegration of the body is assumed to occur prior to the onset of its ablation and

Institute of Mechanics, Moscow State University, Michurinskiĭ pr. 1, Moscow, 117192 Russia

1028-3358/01/4601-0050$21.00

drag. Therefore, the initial conditions are taken in the form

$$m = 1, \quad v = 1, \text{ for } y = y_* = \ln\frac{\rho_0 V_e^2}{\sigma_*}. \tag{6}$$

The solution to the problem (4)–(6) for the exponential atmosphere $\rho = \exp(-y)$ at $\alpha = \text{const}$ and $\beta = \text{const}$ has the form

$$\begin{aligned} m &= \exp[-\beta(1-v^2)], \\ 2^{7/3}\frac{\alpha}{3}e^{2y_*}(e^{-3y} - e^{-3y_*}) &= -(\beta+1) \\ &+ \frac{\exp[-\beta(1-v^2)]}{v^4}(\beta v^2 + 1) + \beta^2 e^{-\beta}\Delta, \\ \Delta = \overline{\mathrm{Ei}}(\beta) - \overline{\mathrm{Ei}}(\beta v^2), &\quad \overline{\mathrm{Ei}}(x) = \int_{-\infty}^{x}\frac{e^t dt}{t}. \end{aligned} \tag{7}$$

For limited values of parameter β ($\beta < 2$), we can employ the approximate expression from [5]:

$$\beta - \ln\frac{\Delta}{2} = -\ln(-\ln v) + 0.83\beta(1-v).$$

This makes it possible to reduce all calculations to elementary functions. The solution depends on the three dimensionless defining parameters α, β, and y_*.

As the calculations show, the results based on formula (7) for $\beta = 0$ are consistent to a high accuracy with the calculations [4] performed according to the difference scheme.

Needless to say, the disintegration model (2) is adequate only in the region of increase of aerodynamic load $\rho_a V^2$ and the disintegration ceases to occur upon attaining the maximum value of this parameter in the trajectory.

Solution (7) allows us to calculate the altitude $h_{\max}$ for which the value $(\rho_a V^2)_{\max}$ is attained in the framework of the model under consideration in simple terms. We perform these calculations for the case of $\beta = 0$ and compare the results obtained with those of [4]. We find from (7) for $\beta = 0$ that

$$\begin{aligned} \rho v^2 &= e^{-y}\left[1 + \frac{4}{3}\alpha_s(e^{-3y} - e^{-3y_*})\right]^{-1/2}, \\ \alpha_s &= 2^{1/3}\alpha e^{2y_*}. \end{aligned} \tag{8}$$

Determining the point of the maximum for function (8), we obtain

$$e^{-3y_{\max}} = \frac{3 - 4\alpha_s e^{-3y_*}}{2\alpha_s}. \tag{9}$$

Table 1

Variant index [4]	h_*, km	z_1, km	$h_{\max}$, km	z_n, km
L4	80.7	78.9	48.4	44.7
P3	76.3	74.3	45.6	43.9
G1	24.4	21.7	7.0	7.9

The values of altitude h_* (6) of the fracture onset and altitude $h_{\max}$ (9) of the maximum aerodynamic load for fragments of the disintegrating body for three variants of those calculated in [4] are given in the table. There, the values z_1 of the altitude for the first disintegration and z_n for the last nth disintegration, which were taken from Table 1 of [4] for the same variants, are also given for comparison.

As follows from the table, the calculations performed in [4] and the data corresponding to analytical model (7), as a whole, are close to one another. However, there is a certain discrepancy between the altitudes of disintegration onset h_* and z_1. This is difficult to explain, since, as follows from Fig. 1 of [4] (see the second summand in the left-hand side of Eq. (9) of [4]), the body drag prior to disintegration onset is negligible and cannot affect the value of z_1. It is possible that this initial divergence also affects the values $h_{\max}$ and z_n, at least for the first two calculation variants.

ACKNOWLEDGMENTS

This work was carried out under the financial support of the Russian Foundation for Basic Research, project no. 99-01-00385.

REFERENCES

1. B. Baldwin and Y. Sheaffer, J. Geophys. Res. **76**, 4653 (1971).
2. S. S. Grigoryan, Kosm. Issled. **17**, 875 (1979).
3. V. P. Korobeĭnikov, V. I. Vlasov, and D. B. Volkov, Mat. Model. **6** (8), 61 (1994).
4. A. G. Ivanov and V. A. Ryzhanskiĭ, Dokl. Akad. Nauk **353**, 334 (1997) [Phys.–Dokl. **42**, 139 (1997)].
5. V. P. Stulov, V. N. Mirskiĭ, and A. I. Vislyĭ, *Aerodynamics of Bolides* (Nauka, Moscow, 1995).

Translated by G. Merzon

Doklady Physics, Vol. 46, No. 1, 2001, pp. 52–55. Translated from Doklady Akademii Nauk, Vol. 376, No. 2, 2001, pp. 195–199.

MECHANICS

Numerical Simulation of a Twisted Turbulent Wake beyond a Self-Propelled Body

Academician O. F. Vasil'ev*, A. G. Demenkov, V. A. Kostomakha***, and G. G. Chernykh****

Received September 4, 2000

Spatial turbulent flows are objects of elevated complexity for mathematical simulation. Examples of these flows can be fluid motion in various kinds of power facilities and chemical-engineering facilities of complicated configuration, flows around three-dimensional bodies, the case of twisting, etc. In this paper, we consider an axisymmetric turbulent wake beyond a self-propelled body. We study a particular case of motion of a body with a propelling device whose thrust compensates hydrodynamic drag. In this case, the body moves uniformly and rectilinearly in an unbounded homogeneous incompressible fluid, so that the longitudinal component of the excess momentum in the wake is zero. The propelling device can also twist the fluid; therefore, in order to prevent body rotation about its axis, the twisting must also be compensated in a certain manner. In this case, the moment of momentum in the wake with respect to its axis also equals zero.

A review of previous studies devoted to numerical investigation of twisted turbulent wakes is given in [1]. There, the results of calculations according to a simplified *e*-model of turbulence are described and, at the same time, attempts at using Reynolds-stress algebraic models and more general second-order mathematical models were criticized. These unsuccessful attempts were apparently caused by the incompleteness or the absence of experimental data for the wake near-field region, which are necessary for using these models. Asymptotic and numerical analysis of twisted wakes, which are based on the classical $(e-\varepsilon)$ model of turbulence, are given in [2–4]. These studies presented a qualitatively adequate description of principal flow features, but failed to describe completely the structure of turbulence in the wake.

A numerical simulation based on using the hierarchy of second-order semiempirical models of turbulence was performed in [5, 6] for a twisted momentum-free turbulent wake with a nonzero moment of momentum. It was shown that satisfactory agreement with experimental data [7] can be obtained on the basis of a mathematical model involving differential transport equations for the normal Reynolds stress and a model of tangential Reynolds stresses, as well as nonequilibrium algebraic relationships for the remaining tangential stresses.

Below, we present our original numerical model constructed for a twisted turbulent flow with a zero moment of momentum, which makes it possible to adequately describe the wake beyond a self-propelled body. The calculations based on this model are compared with experimental data obtained in a wind tunnel in the wake beyond an ellipsoid of revolution whose drag was balanced by the momentum of a twisted jet ejected from its rear part, whereas the twisting introduced by the jet was compensated by the rotation of a part of the body surface in the opposite direction. In these experiments, the following quantities were measured at various distances from the body: all the components of both the average-velocity vector and the Reynolds-stress tensor, as well as the rate of the turbulent-energy dissipation [8].

To describe the flow, we use the set of averaged equations of motion, incompressibility, transfer of normal Reynolds stresses, and rate of turbulent-energy dissipation:

$$U\frac{\partial U}{\partial x} + V\frac{\partial U}{\partial r} = -\frac{1}{r}\frac{\partial}{\partial r}r\langle u'v'\rangle + \frac{\partial}{\partial x}\int_r^\infty \frac{[W^2 + \langle w'^2\rangle - \langle v'^2\rangle]}{r}dr - \frac{\partial(\langle u'^2\rangle - \langle v'^2\rangle)}{\partial x}, \quad (1)$$

* *Institute of Water and Ecological Problems, Siberian Division, Russian Academy of Sciences, pr. Akademika Lavrent'eva 6, Novosibirsk, 630090 Russia*

** *Institute of Computing Technologies, Russian Academy of Sciences, pr. Akademika Lavrent'eva 6, Novosibirsk, 630090 Russia*

*** *Lavrent'ev Institute of Hydrodynamics, Siberian Division, Russian Academy of Sciences, pr. Akademika Lavrent'eva 15, Novosibirsk, 630090 Russia*

1028-3358/01/4601-0052$21.00

$$U\frac{\partial W}{\partial x} + V\frac{\partial W}{\partial r} + \frac{VW}{r} = -\frac{1}{r}\frac{\partial}{\partial r}r\langle v'w'\rangle - \frac{\langle v'w'\rangle}{r} - \frac{\partial\langle u'w'\rangle}{\partial x}, \quad (2)$$

$$\frac{\partial U}{\partial x} + \frac{\partial V}{\partial r} + \frac{V}{r} = 0, \quad (3)$$

$$U\frac{\partial\langle u'^2\rangle}{\partial x} + V\frac{\partial\langle u'^2\rangle}{\partial r} = -2(1-\alpha)\langle u'v'\rangle\frac{\partial U}{\partial r} - \frac{2}{3}\varepsilon - C_1\frac{\varepsilon}{e}\left(\langle u'^2\rangle - \frac{2}{3}e\right) + \frac{2}{3}\alpha P + \frac{C_s}{r}\frac{\partial}{\partial r}\left(\frac{re\langle v'^2\rangle}{\varepsilon}\frac{\partial\langle u'^2\rangle}{\partial r}\right), \quad (4)$$

$$U\frac{\partial\langle v'^2\rangle}{\partial x} + V\frac{\partial\langle v'^2\rangle}{\partial r} - 2\frac{W}{r}\langle v'w'\rangle = 2(1-\alpha)\langle v'w'\rangle\frac{W}{r} - \frac{2}{3}\varepsilon - C_1\frac{\varepsilon}{e}\left(\langle v'^2\rangle - \frac{2}{3}e\right) + \frac{C_s}{r}\frac{\partial}{\partial r}\left[\frac{re}{\varepsilon}\left(\langle v'^2\rangle\frac{\partial\langle v'^2\rangle}{\partial r} - \frac{2\langle v'w'\rangle^2}{r}\right)\right] - 2\frac{C_s e}{r\varepsilon}\left[\langle v'w'\rangle\frac{\partial\langle v'w'\rangle}{\partial r} + \langle w'^2\rangle\frac{\langle v'^2\rangle - \langle w'^2\rangle}{r}\right] + \frac{2}{3}\alpha P, \quad (5)$$

$$U\frac{\partial\langle w'^2\rangle}{\partial x} + V\frac{\partial\langle w'^2\rangle}{\partial r} + 2\frac{W}{r}\langle v'w'\rangle = -2(1-\alpha)\langle v'w'\rangle\frac{\partial W}{\partial r} - \frac{2}{3}\varepsilon - C_1\frac{\varepsilon}{e}\left(\langle w'^2\rangle - \frac{2}{3}e\right) + \frac{C_s}{r}\frac{\partial}{\partial r}\left[\frac{re}{\varepsilon}\left(\langle v'^2\rangle\frac{\partial\langle w'^2\rangle}{\partial r} + \frac{2\langle v'w'\rangle^2}{r}\right)\right] + \frac{2C_s e}{r\varepsilon}\left[\langle v'w'\rangle\frac{\partial\langle v'w'\rangle}{\partial r} + \langle w'^2\rangle\frac{\langle v'^2\rangle - (w'^2)}{r}\right] + \frac{2}{3}\alpha P, \quad (6)$$

$$U\frac{\partial\varepsilon}{\partial x} + V\frac{\partial\varepsilon}{\partial r} = \frac{C_\varepsilon}{r}\frac{\partial}{\partial r}\left(\frac{re\langle v'^2\rangle}{\varepsilon}\frac{\partial\varepsilon}{\partial r}\right) + \frac{\varepsilon}{e}(C_{\varepsilon 1}P - C_{\varepsilon 2}\varepsilon). \quad (7)$$

Here, (x, r, φ) is the cylindrical system of coordinates with the origin at the body's rear edge; the x-axis is directed oppositely to the body motion; U, V, W, u', v' and w' are the components of the velocity for the averaged and pulsation motion; $\langle u'^2\rangle$, $\langle v'^2\rangle$, $\langle w'^2\rangle$, $\langle u'v'\rangle$, $\langle u'w'\rangle$, and $\langle v'w'\rangle$ are the Reynolds stresses; $e = \frac{1}{2}(\langle u'^2\rangle + \langle v'^2\rangle + \langle w'^2\rangle)$ is the turbulence energy; and the angular brackets imply averaging. In the right-hand side of Eqs. (1), (2), (4)–(7), the terms corresponding to molecular viscosity were assumed to be small and, therefore, could be discarded.

Tangential turbulent stresses are determined from nonequilibrium algebraic relations [9]:

$$\langle u'v'\rangle = \alpha_1\langle v'^2\rangle\frac{\partial U}{\partial r}, \quad (8)$$

$$\langle u'w'\rangle = \alpha_1\left(\langle u'v'\rangle\frac{\partial W}{\partial r} + \langle v'w'\rangle\frac{\partial U}{\partial r}\right), \quad (9)$$

$$\langle v'w'\rangle = \alpha_1\left(\langle v'^2\rangle r\frac{\partial(W/r)}{\partial r} + \frac{W}{r}(\langle v'^2\rangle - \langle w'^2\rangle)\right), \quad (10)$$

where $\alpha_1 = -\frac{\lambda_1 e}{\varepsilon}$ and $\lambda_1 = \frac{1-C_2}{C_1 + P/\varepsilon - 1}$. In Eqs. (4)–(7) and relationships (8)–(10), the quantity P is determined by the turbulence energy of the averaged motion:

$$P = -\left(\langle u'v'\rangle\frac{\partial U}{\partial r} + \langle v'w'\rangle r\frac{\partial(W/r)}{\partial r} + \langle u'w'\rangle\frac{\partial W}{\partial x} + \langle u'^2\rangle\frac{\partial U}{\partial x} + \langle v'^2\rangle\frac{\partial V}{\partial r} + \langle w'^2\rangle\frac{V}{r}\right).$$

We cast the model proposed in [10] on the basis of the above-mentioned mathematical model. The empirical constants of the model were taken to be $C_s = 0.22$, $C_\varepsilon = 0.17$, $\alpha = 0.93$, $C_1 = 0.6$, $C_2 = 2.2$, $C_{\varepsilon 1} = 1.45$, and $C_{\varepsilon 2} = 1.92$.

As the initial conditions at $x = 10D$, we set the experimental transverse distributions for U, W, ε, and $\langle u_i'u_i'\rangle$, $i = 1, 2, 3$. Our experiments corresponded to the Reynolds number $\mathrm{Re} = \frac{U_0 D}{\nu} = 50000$, where ν is the kinematic viscosity, U_0 is the velocity of the unperturbed fluid, and D is the body diameter.

In the case of $r \longrightarrow \infty$, the conditions for an unperturbed flow were posed; and in the case of $r = 0$, the conditions of symmetry for U, $\langle u_i'u_i'\rangle$, and ε and of asymmetry for V and W were required to be valid:

$$\frac{\partial U}{\partial r} = \frac{\partial\langle u_i'u_i'\rangle}{\partial r} = \frac{\partial\varepsilon}{\partial r} = V = W = 0.$$

From Eqs. (1)–(3) and the indicated initial and boundary conditions for the flow under consideration, the following laws of conservation for the excess momentum and the moment of momentum can be formulated:

$$J(x) = 2\pi\rho_0\int_0^\infty\left[UU_1 - \int_r^\infty\frac{[W^2 + \langle w'^2\rangle - \langle v'^2\rangle]}{r'}dr' + \langle u'^2\rangle - \langle v'^2\rangle\right]rdr = 0, \quad (11)$$

$$M(x) = 2\pi\rho_0\int_0^\infty(UW + \langle u'w'\rangle)r^2dr = 0. \quad (12)$$

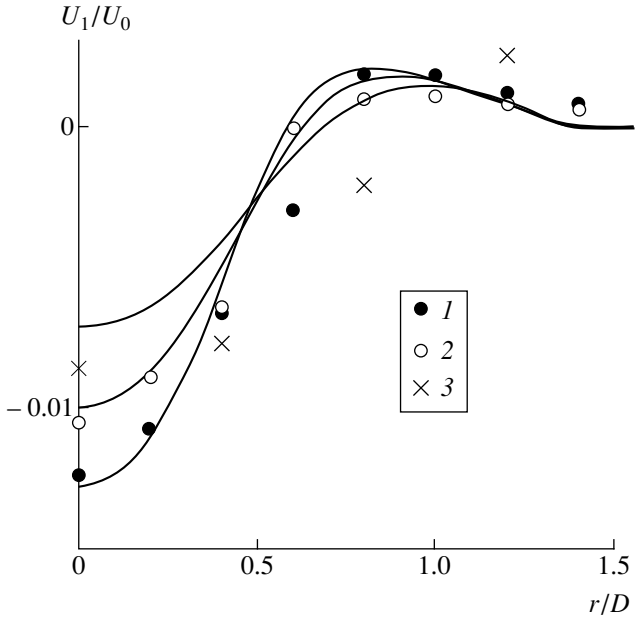

Fig. 1. Comparison of the dimensionless profiles for the defect of the velocity longitudinal component with experimental data.

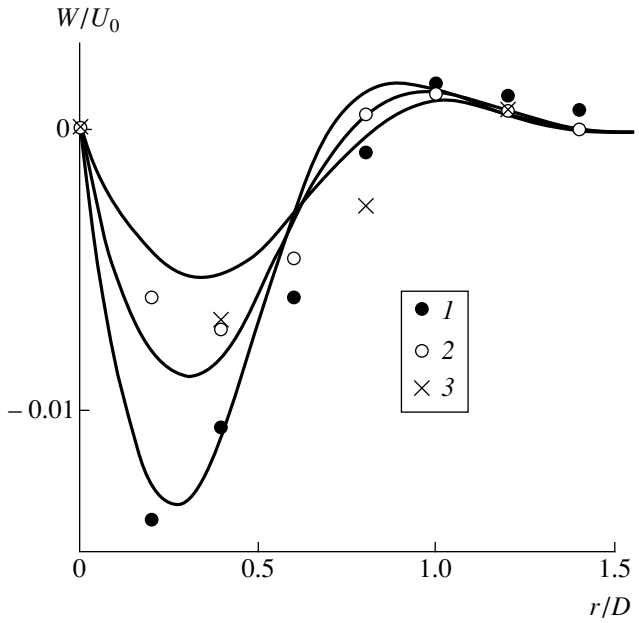

Fig. 2. Comparison of the dimensionless profiles for the velocity circular component with experimental data.

Here, $U_1 = U - U_0$ is the defect of the velocity longitudinal component and $\rho_0 = \text{const}$ is the fluid density.

The numerical realization of this model is based on the application of the finite-difference algorithm of the first-order approximation at mobile nets. As compared to [5, 6], this algorithm is modified with the goal to guarantee the laws of conservation (11) and (12) hold.

In the process of calculation, the boundary conditions for U_1, W, e, ε, and $\langle u_i'^2 \rangle$ were transported from infinity to the line $r = r_* = 4D$ (the quantity r_* was determined in the process of numerical experiments).

The calculated distributions for the defect of the longitudinal $U_1(r, x)$ and circular $W(r, x)$ components of the average-velocity vector, as well as the distribution of the intensities of various components ($\sigma_u = \langle u'^2 \rangle^{1/2}$, $\sigma_v = \langle v'^2 \rangle^{1/2}$, $\sigma_w = \langle w'^2 \rangle^{1/2}$) of the velocity pulsation, are compared with the experimental data in Figs. 1, 2, 3, respectively. The solid curves in these figures show the results of calculations; the dots correspond to the experimental data $\left(\frac{x}{D} = (1)\ 20, (2)\ 30, (3)\ 46\right)$. As is seen, the calculated results agree quite satisfactorily with the experimental data.

Figure 4 illustrates the change in the calculated and measured characteristic scales of turbulence as a function of the distance from the body. Here, U_{10}/U_0 is the axial value of the defect for the velocity longitudinal component (solid line and dots *1* are, respectively, the calculated and experimental data); $\frac{|W|_{\max}}{U_0}$ (dashed line and dots *2*) is the maximum value of the velocity circular component in a given cross section of the wake; $\frac{e_0}{U_0^2}$ (dashed–dotted line and dots *3*) is the turbulence energy at the wake axis; and $\frac{r_{1/2}}{D}$ (dashed line and dots *4*) is the characteristic scale of a wake width, which is determined from the condition

$$\langle u'^2 \rangle^{1/2}(r_{1/2}, x) = 0.5 \langle u'^2 \rangle^{1/2}(0, x),$$

where $\langle u'^2 \rangle^{1/2}(0, x)$ is the root-mean-square value for fluctuations of the velocity longitudinal component at the wake axis.

As can be seen, the results of calculations agree with the experimental data, virtually coinciding for the scaling functions $U_{10}(x)$, $W_{\max}(x)$, $e_0(x) = e(0, x)$, and $r_{1/2}(x)$ within the entire range of the values of $\frac{x}{D}$ under consideration.

At large distances from the body, the behavior of all the scaling functions exhibits an exponential dependence on x (in the logarithmic coordinates, these are the dashed straight lines in Fig. 4). In the framework of the mathematical model used, this fact is a necessary indication of attaining self-similarity of the turbulent motion in the wake. In particular, it is seen that the circular velocity component decreases for large $\frac{x}{D}$ as

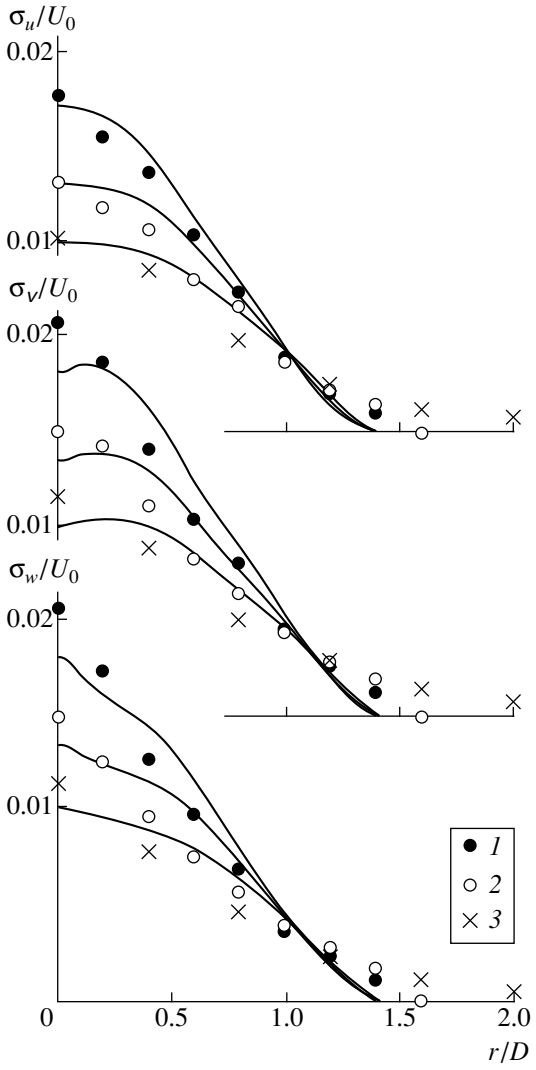

Fig. 3. Transverse distributions for three components of turbulence intensities in the wake at various distances from the body.

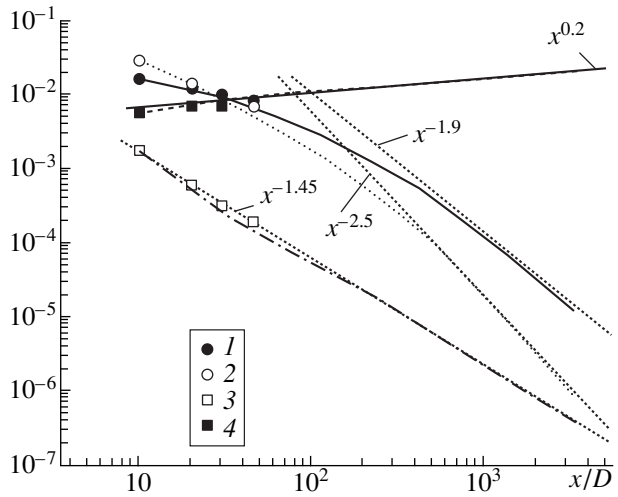

Fig. 4. Change in the characteristic scales of the turbulent flow in the wake as a function of distance from the body.

$W_{\max}(x) \sim x^{-2.5}$, i.e., more rapidly than the axial defect of the velocity $U_{10}(x) \sim x^{-1.9}$, so that the twisting can be ignored beginning from a certain distance from the body.

Another necessary indication of attaining self-similarity is the affine similarity of transverse profiles for various characteristics of the turbulence in the wake, which are normalized to the corresponding scales. Based on analysis of the calculated results, we have determined that the similarity of distributions is also attained in the wake for $\frac{x}{D} > 1000$ in exact correspondence with attaining asymptotic degeneracy (Fig. 4).

Thus, in this paper, we have constructed the numerical model of a twisted turbulent wake beyond a self-propelled body. This model is based on the second-order semiempirical model of turbulence. The results of the calculations are well consistent with the experimental data. The numerical analysis is also carried out for the self-similarity of the turbulent-wake degeneracy in the far-field region.

ACKNOWLEDGMENTS

This work was supported by the Russian Foundation for Basic Research, project no. 98-01-00736 and by the Siberian Division of the RAS, integration project no. 2000-1.

REFERENCES

1. J. A. Schetz, in *Progress in Astronautics and Aeronautics*, Ed. by M. Summerfield (New York Univ. Press, New York, 1980; Mir, Moscow, 1984), Vol. 68.
2. A. G. Gumilevskiĭ, Izv. Akad. Nauk, Mekh. Zhidk. Gaza, No. 3, 35 (1992).
3. A. G. Gumilevskiĭ, Izv. Akad. Nauk, Mekh. Zhidk. Gaza, No. 1, 41 (1993).
4. A. G. Gumilevskiĭ, Izv. Akad. Nauk, Mekh. Zhidk. Gaza, No. 5, 35 (1993).
5. A. G. Demenkov, V. A. Kostomakha, and G. G. Chernykh, Vychisl. Tekhnol. **2** (5), 26 (1997).
6. G. G. Chernykh, A. G. Demenkov, and V. A. Kostomakha, Russ. J. Numer. Anal. Math. Model. **13** (4), 279 (1998).
7. V. A. Kostomakha and N. V. Lesnova, Prikl. Mekh. Tekh. Fiz. **36** (2), 88 (1995).
8. V. A. Kostomakha and N. V. Gavrilov, in *Proceedings of the IV Siberian Workshop on Flow Stability of Homogeneous and Heterogeneous Liquids, Novosibirsk, 1997*, p. 31.
9. W. Rodi, Z. Angew. Math. Mech. **56**, 219 (1976).
10. B. E. Launder and A. Morse, in *Turbulent Shear Flows 1*, Ed. by F. Durst, B. E. Launder, F. W. Schmidt, and J. H. Whitelaw (Springer-Verlag, Berlin, 1979; Mashinostroenie, Moscow, 1982), pp. 279–294.

Translated by V. Bukhanov

Doklady Physics, Vol. 46, No. 1, 2001, pp. 56–59. Translated from Doklady Akademii Nauk, Vol. 376, No. 3, 2001, pp. 331–334.

MECHANICS

On the Similarity of Acoustic and Seismic Regimes in Fracture Processes

L. R. Botvina and T. B. Petersen

Presented by Academician V.I. Keĭlis-Borok February 25, 2000

Received June 7, 2000

It is well known [1, 2] that the regularities in processes of fracturing laboratory samples made of rocks and the preparation of an earthquake are quite similar. There is a sufficient number of grounds to assume that the same similarity can also be observed in analyzing metallic-sample fractures. The suggestion we verify in this study is based on the fact that the processes of crack accumulation and crack growth under different forms of loading have common features in various materials. They are associated with a similar sequence of stages which are retained on many typical scales and testify to the self-similarity of the fracture process [3–6].

One of these common regularities is the similarity in the distribution function of basic fracture parameters. For example, it was established in [5] that the size distribution of fatigue microcracks in carbon-steel samples obeys the relation

$$\log N = C_S - b_S \log l,$$

where N is the number of microcracks with size equal to or larger than l and C_S is a constant. The merging of microcracks and the onset of localized sample fracturing, which implies a change in its mechanism, result in an almost two-fold reduction in the tangent b_S of the slope angle for the distribution curve.

A similar change in the mechanism of accumulating discontinuities must affect the physical characteristics of the fracture process. Indeed, it was established in a number of studies (see, e.g., [7, 8]) that the amplitude distribution of acoustic signals under the development of vulnerability to damage in rock samples is consistent with the relation

$$\log N = C_{AE} - b_{AE} \log E,$$

where N is the number of acoustic pulses with acoustic energy equal to or lower than E, C_{AE} is a constant, and the parameter b_{AE} in the last relation is also lowered in its absolute value prior to fracturing.

The Gutenberg–Richter relation, well known in seismology, has a similar form. This relation associates the number of seismic events with the fracture energy [9]:

$$\log N = C_S - b_S \log E = C_S - b_S M. \quad (1)$$

Here, N is the number of seismic events with energy not exceeding E, M is the event magnitude, and C_S is a constant. Prior to the earthquake, the lowering of the exponent b_S often takes place [10].

The similarity observed in the above power relations is important from different standpoints. First, it allows us to use the lowering of the exponents (b_C, b_{AE}, and b_S) in the above power relations as forerunners of fracture. In addition, it allows us to associate the reduction in parameter b_S prior to the earthquake with the merging of breaks which appear in the process of the earthquake's preparation. And, finally, an analogy based on the similar sequence of the fracture preparation processes in a solid body makes it possible to employ metallic samples along with rock samples for studying and modeling seismic processes.

Keeping this analogy in mind, we consider the behavior of parameter b_{AE} under the fracturing of metallic samples held previously in a corrosive medium.

To perform this analysis, the tests in [11] for the tension of samples made of low-doped 30G2 steel with a ferrite-pearlite structure were carried out with an ultimate strength and yield stress of 655 MPa and 380 MPa, respectively, in the initial state. The samples contained an induced fatigue crack and were held for different periods of time (360 and 2160 h) in a medium containing hydrogen sulfide, which induces the embrittlement of steel.

In the process of mechanical testing, the acoustic emission was registered in the form of a sequence of signals digitized with a discretization frequency of 2 MHz. The recording of each signal was accompanied by information on both its arrival time at a piezoelectric sensor and load magnitude. For discrimination of useful signals against the noise background, the informa-

Baĭkov Institute of Metallurgy and Materials Science, Russian Academy of Sciences, Leninskiĭ pr. 49, Moscow, 117334 Russia

1028-3358/01/4601-0056$21.00

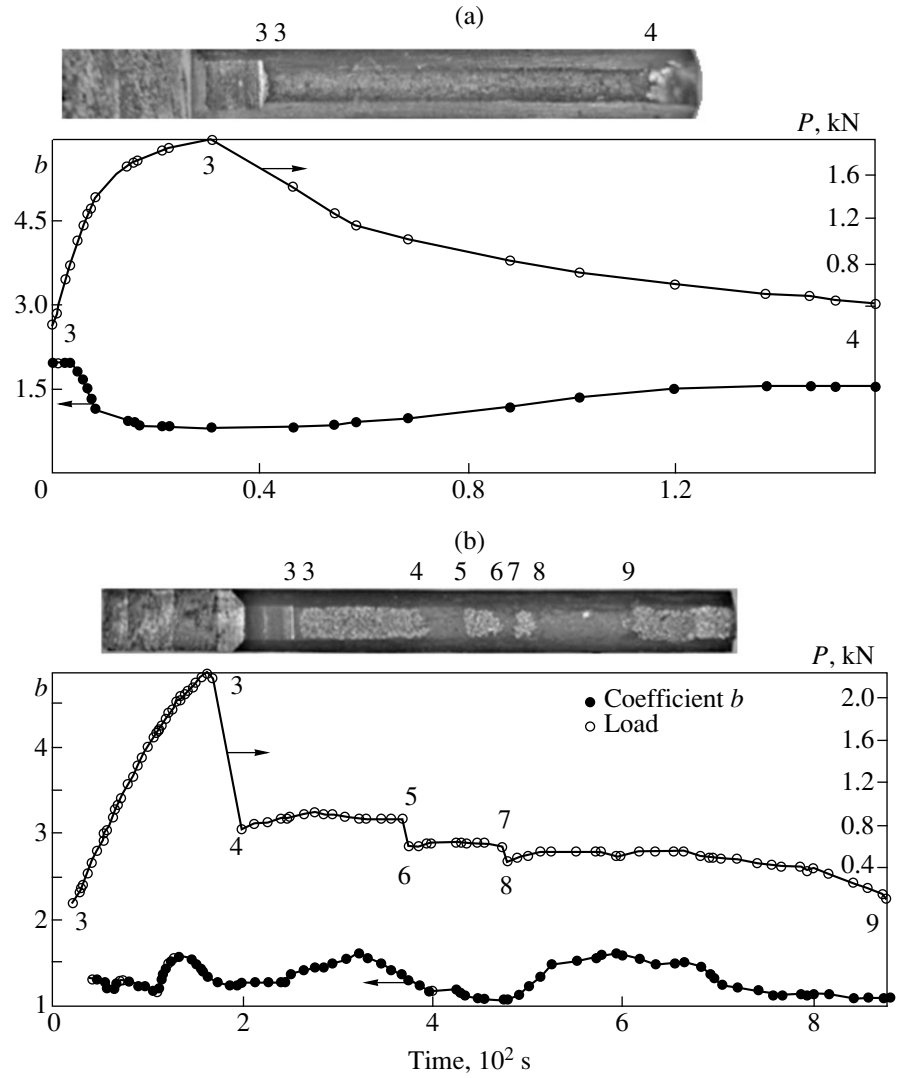

Fig. 1. Changes in the load and in parameter b_{AE} with time for the case of crack development in samples of 30G2 steel: (a) in the initial state and (b) after three-month holding in a corrosive medium.

tive attributes of the signal shape and spectrum were used. The basic method of information processing consisted in calculating parameter b_{AE}, which characterizes the slope angle for the cumulative amplitude-distribution curve under fracturing [12].

The value of parameter b_{AE} was determined as the modulus of the slope-angle tangent for the line obtained by the linear approximation (using the least-square technique) of the curve for the amplitude distribution of the acoustic-emission signals:

$$\log N = C_{AE} - b_{AE}\log E = C_{AE} - b_{AE}M. \qquad (2)$$

Here, N is the number of acoustic-emission signals registered with an energy larger than $E \sim A_0^2$; A is the signal amplitude; M is the signal magnitude measured in decibels and equal to $M = 20\log\frac{A}{A_0}$; A_0 is the threshold signal amplitude taken equal to 1 μV; and C_{AE} is an acoustic parameter characterizing the constant component of dependence (2).

To construct the time dependence for parameter b_{AE}, each of its values was determined according to formula (2) in a moving window involving 50 experimental points. The neighboring points of the curve were obtained when shifting the window stepwise (3–5 points). For reducing the irregularity of the plot, linear smoothing was performed.

Furthermore, the logarithmic dependence of the accumulated number of events as a function of magnitude for all sampling points was plotted. Parameter b_{AE} was also estimated according to the curve slope angle.

The results of estimates for the time dependence of parameter b_{AE} for samples of the initial material embrittled as a result of being held in a corrosive medium are shown in Fig. 1 together with the loading curves. As

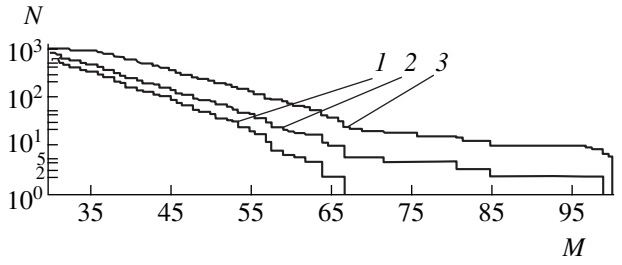

Fig. 2. Cumulative distributions for the number of acoustic-emission events as functions of their magnitude for 30G2-steel samples at various stages of loading.

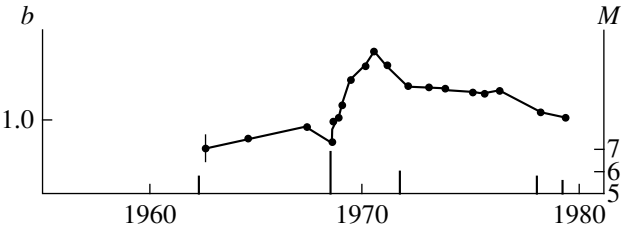

Fig. 3. Changes in parameter b_S characterizing the process of earthquake preparation in the central region of New Zealand from 1955 through 1979. The earthquakes with magnitudes $M > 5$ are indicated in the abscissa axis by vertical lines.

follows from Fig. 1, holding in the corrosive medium abruptly changes the shape of the stress-strain curve. After holding in this medium, in contrast to the smooth tensile-test diagram characteristic for steel in the initial state (Fig. 1a), a number of abrupt load drops appear on the curve (Fig. 1b) which correspond to crack jumps. It follows from Fig. 1 that immediately before the load drop, i.e., prior to the jump of the crack, a decrease in parameter b_{AE} is observed.

The data presented in [5, 10, 12] allow us to suggest that the high magnitudes of acoustic-emission events and, correspondingly, the low values of parameter b_{AE} are caused by the interaction of defects at the stage of plastic deformation of the metallic sample and by the merging of microcracks in the plastic zone prior to the formation of the main crack. Consequently, the decrease in parameter b_{AE} can be considered a criterion for fracture localization.

Studies of breaks in tested samples after holding in a corrosive medium have revealed a periodic relief associated with a jump-type crack development (Fig. 1b). It follows from Fig. 1 that the crack-jump length is proportional to the load-drop magnitude. While testing samples made of the initial material (Fig. 1a), crack jumps and a periodic relief were absent. Studies of breaks with a scanning electron microscope have shown that, obeying the mechanism of intergrain cleavage, the fracture in the region of the crack jump is brittle. At the same time, in the regions of slow stable crack growth, the fracture mechanism changes and attributes of viscous fracture (dimples) are observed in the breaks. The same dimple microrelief is also characteristic for a sample made of the initial material.

Analysis of the acoustic-emission signal shapes has shown that signals with relatively low amplitudes, mean frequencies, and a long signal-front time (time for attaining the signal-amplitude peak) correspond to a fracture mechanism of the viscous type. In contrast, the brittle fracture is characterized by high amplitudes and frequencies and a relatively short time of signal increase. Signals of the viscous type dominated at the initial stage of loading, which was associated with plastic deformation, as well as at the stage of viscous fracture. Prior to the jump of a brittle crack, the fraction of brittle-type signals increased.

Magnitude analysis of the distribution curves for the accumulated number of acoustic signals (analysis of recurrence curves) has revealed the following regularities. The recurrence curves plotted for the initial period of sample deformation were linear in their logarithmic coordinates (i.e., M was a linear function of $\log N$), Fig. 2, curve *1*, with slope angle b_{AE} equal to 1.5. The curves plotted for the subsequent periods of time in which crack jumps were found had a discontinuity in the high-amplitude region of acoustic emission signals (Fig. 2, curve *2*). With an increase in the number of crack jumps, the values of parameter b_{AE} corresponding to the linear portion of the curves decreased (Fig. 2, curve *3*) from 1.15 (curve *2*) to 0.9. The values of b_{AE} obtained as a result of testing all the samples were 1.37 and 1.01 for the embrittled and the initial materials, respectively.

The results of the studies carried out allowed us to reveal certain common features of the acoustic and seismic regimes preceding the basic event (fracture or earthquake).

First, the periodic character of the time dependence for parameter b_{AE}, while testing metallic samples (Fig. 1), is similar to the character of the change in parameter b_S entering into the Gutenberg–Richter relation (1), which occurs in the period of earthquake preparation. As is seen from Fig. 3, in which the time dependence of parameter b_{AE} is shown for one of the central regions of New Zealand [10], an increase in this parameter for several years prior to the basic event is replaced by a decrease for several months or weeks prior to an earthquake. A similar lowering of parameter b_S in the region of fore-shock activity is also noted in many other papers.

Second, the values of parameters b_{AE} and b_S are close to one another and vary in similar ranges. In this case, parameter b_S is associated with the change in the stressed state [2], the inhomogeneity of the geological structure [1], and the degree of the rock brittleness depending, in particular, on the depth of the earthquake

center: the closer the earthquake center to the crust surface, the higher the rock brittleness. Systematic studies of these factors are apparently absent; however, it is noted in [2] that the higher the rock brittleness, the higher parameter b_S. Similar conclusions can be drawn based on the results of the tests carried out in the present study.

Third, a common feature of the acoustic and seismic regimes is the existence of a linear part of the distribution curves and a discontinuity in the regions of mean and large magnitudes, respectively.

Thus, our studies have confirmed the suggestion that there exists a similarity in the basic regularities for the development of acoustic activity under the fracturing of metallic samples and for the seismic activity in the period of earthquake preparation. The similarity indicated is, probably, based on the common regularities of nucleation and development of discontinuities in various materials at different-scale levels. Therefore, the difference in the properties of metallic samples and rocks is of no decisive importance and can only affect the values of exponents in relations obeying the power law which describe the kinetics of the basic-event preparation. Making use of metallic samples as models for studying the global processes occurring in the Earth's crust allows us to expand the possibilities for analysis of the basic characteristics of these processes and the factors affecting them.

ACKNOWLEDGMENTS

This work was supported by the Russian Foundation for Basic Research, projects nos. 0001-00160 and 0015-99073.

REFERENCES

1. K. Mogi, Bull. Earthquake Res. Inst. Univ. Tokyo **4**, 831 (1962).
2. C. H. Scholz, Bull. Seismol. Soc. Am. **58**, 399 (1968).
3. L. R. Botvina and G. I. Barenblatt, Probl. Prochn., No. 12, 17 (1985).
4. V. I. Keilis-Borok, Rev. Geophys. Res. **28**, 9 (1990).
5. L. R. Botvina, I. M. Rotvaĭn, V. I. Keĭlis-Borok, and I. B. Oparina, Dokl. Akad. Nauk **345**, 809 (1995).
6. L. R. Botvina and I. B. Oparina, Dokl. Akad. Nauk **362**, 762 (1998) [Dokl. Phys. **43**, 644 (1998)].
7. J. Weeks, D. Lockner, and J. Byerlee, Bull. Seismol. Soc. Am. **68**, 333 (1978).
8. V. B. Smirnov, A. V. Ponomarev, and A. D. Zav'yalov, Fiz. Zemli, No. 1, 38 (1995).
9. B. Gutenberg and C. F. Richter, *Seismicity of the Earth* (Princeton Univ. Press, Princeton, 1949).
10. W. D. Smith, Nature **289**, 333 (1981).
11. L. R. Botvina, T. V. Tetyueva, and A. V. Ioffe, Metalloved. Term. Obrab. Met., No. 2, 14 (1998).
12. EWGAE Codes for Acoustic Emission Examination, European Group on Acoustic Emission, NDT Int. **18** (4) (1985).

Translated by T. Galkina

Doklady Physics, Vol. 46, No. 1, 2001, pp. 60–62. Translated from Doklady Akademii Nauk, Vol. 376, No. 3, 2001, pp. 335–337.

MECHANICS

Three-Dimensional Flow of an Ideally Plastic Layer Compressed by Rough Plates

M. V. Mikhaĭlova

Presented by Academician A.Yu. Ishlinskiĭ May 10, 2000

Received May 18, 2000

An asymptotic solution to the problem of compressing a plane strip by rough plates was found by Prandtl [1]. The compression of an ideally plastic three-dimensional layer was considered in [2]. Below, we deal with three-dimensional flows of an ideally plastic material in the case of plasticity condition depending on stress-deviator components. We prove that the linearity of compressing stresses is not related to the form of the plasticity condition. In particular, we analyze the Mises plasticity condition.

1. We consider the equilibrium equations

$$\begin{aligned}\frac{\partial\sigma_x}{\partial x}+\frac{\partial\tau_{xy}}{\partial y}+\frac{\partial\tau_{xz}}{\partial z}&=0,\\ \frac{\partial\tau_{xy}}{\partial x}+\frac{\partial\sigma_y}{\partial y}+\frac{\partial\tau_{yz}}{\partial z}&=0,\\ \frac{\partial\tau_{xz}}{\partial x}+\frac{\partial\tau_{yz}}{\partial y}+\frac{\partial\sigma_z}{\partial z}&=0\end{aligned}\qquad(1.1)$$

and the plasticity condition

$$f(\sigma'_{ij})=f(\sigma'_x,\sigma'_y,\sigma'_z,\tau_{xy},\tau_{xz},\tau_{yz})=0,\qquad(1.2)$$

where σ_{ij} are the stress-tensor components and σ'_{ij} are the stress-deviator components:

$$\sigma'_{ij}=\sigma_{ij}-\delta_{ij}\sigma,\quad \sigma=\frac{1}{3}\sigma_{ii}.\qquad(1.3)$$

From (1.2), in accordance with the associated flow rule, we have

$$\begin{aligned}\varepsilon_x&=\lambda\frac{\partial f}{\partial\sigma_x},\quad 2\varepsilon_{xy}=\lambda\frac{\partial f}{\partial\tau_{xy}},\\ \varepsilon_y&=\lambda\frac{\partial f}{\partial\sigma_x},\quad 2\varepsilon_{xz}=\lambda\frac{\partial f}{\partial\tau_{xz}},\quad \lambda\ge 0,\\ \varepsilon_z&=\lambda\frac{\partial f}{\partial\sigma_x},\quad 2\varepsilon_{yz}=\lambda\frac{\partial f}{\partial\tau_{yz}},\end{aligned}\qquad(1.4)$$

where ε_{ij} are the strain-rate components.

Chuvash State Pedagogical University, Cheboksary, 428015 Russia

From (1.2)–(1.4), we have

$$\varepsilon_x+\varepsilon_y+\varepsilon_z=0\qquad(1.5)$$

and then

$$\frac{\varepsilon_x}{\dfrac{\partial f}{\partial\sigma_x}}=\frac{\varepsilon_y}{\dfrac{\partial f}{\partial\sigma_y}}=\frac{2\varepsilon_{xy}}{\dfrac{\partial f}{\partial\tau_{xy}}}=\frac{2\varepsilon_{xz}}{\dfrac{\partial f}{\partial\tau_{xz}}}=\frac{2\varepsilon_{yz}}{\dfrac{\partial f}{\partial\tau_{yz}}}.\qquad(1.6)$$

Let a layer be compressed along the z-axis by rigid parallel rough plates (see the figure). We seek the solution under the assumption that all deviator components are functions of only variable z:

$$\sigma'_{ij}=\sigma'_{ij}(z).\qquad(1.7)$$

Furthermore, we set that

$$\tau_{xz}=az+c_1,\quad \tau_{yz}=bz+c_2,\quad a,b,c_1,c_2=\text{const}.\qquad(1.8)$$

It follows from (1.1), (1.7), and (1.8) that

$$\begin{aligned}\sigma_x&=-ax-by+c_3+\varphi_1(z),\\ \sigma_y&=-ax-by+c_3+\varphi_2(z),\\ \sigma_z&=-ax-by+c_3,\quad c_3=\text{const}.\end{aligned}\qquad(1.9)$$

We seek the displacement-velocity components in the form

$$\begin{aligned}u&=p_1x+q_1y+\psi_1(z),\\ v&=p_2x+q_2y+\psi_2(z),\\ w&=cz,\quad p_i,q_i,c=\text{const},\end{aligned}\qquad(1.10)$$

where

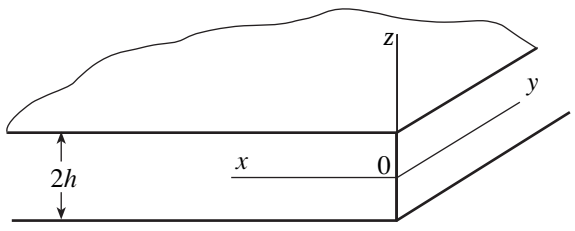

Figure.

1028-3358/01/4601-0060$21.00

$$\varepsilon_x = \frac{\partial u}{\partial x}, \quad \varepsilon_y = \frac{\partial v}{\partial y}, \quad \varepsilon_z = \frac{\partial w}{\partial z},$$

$$\varepsilon_{xy} = \frac{1}{2}\left(\frac{\partial u}{\partial y} + \frac{\partial v}{\partial x}\right), \quad \varepsilon_{xz} = \frac{1}{2}\left(\frac{\partial u}{\partial z} + \frac{\partial w}{\partial x}\right), \qquad (1.11)$$

$$\varepsilon_{yz} = \frac{1}{2}\left(\frac{\partial v}{\partial z} + \frac{\partial w}{\partial y}\right).$$

According to (1.10) and (1.11),

$$\varepsilon_x = p_1, \quad \varepsilon_y = q_2, \quad \varepsilon_z = c, \quad \varepsilon_{xy} = \frac{1}{2}(q_1 + p_2), \qquad (1.12)$$

$$\varepsilon_{xz} = \frac{1}{2}\frac{d\psi_1}{dz}, \quad \varepsilon_{yz} = \frac{1}{2}\frac{d\psi_2}{dz}.$$

From (1.12) and (1.5), we arrive at the equality

$$p_1 + q_2 + c = 0. \qquad (1.13)$$

With regard to (1.12), expressions (1.6) take the form

$$\frac{p_1}{\partial f/\partial \sigma_x} = \frac{q_2}{\partial f/\partial \sigma_y} = \frac{q_1 + p_2}{\partial f/\partial \tau_{xy}} = \frac{\psi_1'}{\partial f/\partial \tau_{xz}} = \frac{\psi_2'}{\partial f/\partial \tau_{yz}}. \qquad (1.14)$$

According to (1.2), (1.3), and (1.7), functions $\frac{\partial f}{\partial \sigma_{ij}}$ depend on variable z. It follows from (1.2) and (1.9) that

$$\frac{\partial f}{\partial \sigma_{ij}} = \frac{\partial f}{\partial \sigma_{ij}}(\varphi_1(z), \varphi_2(z), \tau_{xz}, \tau_{yz}),$$
$$\tau_{xy} = \tau_{xy}(\varphi_1(z), \varphi_2(z), \tau_{xz}, \tau_{yz}). \qquad (1.15)$$

According to (1.15), functions $\varphi_1(z)$ and $\varphi_2(z)$ are determined from the relationships

$$\frac{p_1}{\partial f/\partial \sigma_x} = \frac{q_2}{\partial f/\partial \sigma_y} = \frac{q_1 + p_2}{\partial f/\partial \tau_{xy}}.$$

From (1.14), we have

$$\psi_1 = p_1 \int \left(\frac{\partial f}{\partial \sigma_x} \Big/ \frac{\partial f}{\partial \tau_{xz}}\right) dz + c_4,$$

$$\psi_1 = p_1 \int \left(\frac{\partial f}{\partial \sigma_x} \Big/ \frac{\partial f}{\partial \tau_{yz}}\right) dz + c_5, \quad c_4, c_5 = \text{const}.$$

According to (1.9), the linearity of the compressing stresses σ_z does not depend on the form of plasticity condition (1.2).

2. We assume that both incompressibility condition (1.5) and the following relations of the plasticity theory are valid [3]:

$$f_1(\sigma_{ij}') = 0, \quad f_2(\sigma_{ij}') = 0, \qquad (2.1)$$

$$\sigma_x'\varepsilon_{xy} + \tau_{xy}\varepsilon_y + \tau_{xz}\varepsilon_{yz} = \tau_{xy}\varepsilon_x + \sigma_y'\varepsilon_{xy} + \tau_{yz}\varepsilon_{xz},$$
$$\tau_{xy}\varepsilon_{xz} + \sigma_y'\varepsilon_{yz} + \tau_{yz}\varepsilon_z = \tau_{xz}\varepsilon_{xy} + \tau_{yz}\varepsilon_y + \sigma_z'\varepsilon_{yz}, \qquad (2.2)$$
$$\tau_{xz}\varepsilon_x + \tau_{yz}\varepsilon_{xy} + \sigma_z'\varepsilon_{xz} = \sigma_x'\varepsilon_{xz} + \tau_{xy}\varepsilon_{yz} + \tau_{xz}\varepsilon_z.$$

We seek the solution under the assumption that expressions (1.7)–(1.10) hold. In this case, relations (2.2) take the form

$$(q_1 + p_2)(\varphi_1 - \varphi_2) + 2\tau_{xy}(q_2 - p_1) + (az + c_1)\psi_2' - (bz + c_2)\psi_1' = 0, \qquad (2.3)$$

$$\tau_{xy}\psi_1' + \varphi_2\psi_2' = F_1(z), \qquad (2.4)$$

$$\varphi_1\psi_1' + \tau_{xy}\psi_2' = F_2(z), \qquad (2.5)$$

where

$$F_1(z) = (q_1 + p_2)(az + c_1) - 2(c - q_2)(bz + c_2),$$
$$F_2(z) = (q_1 + p_2)(bz + c_2) - 2(c - p_1)(az + c_1).$$

The set of equations (2.4) and (2.5) is linear with respect to ψ_1' and ψ_2'. From (2.4) and (2.5), we find

$$\psi_1' = \frac{F_1\tau_{xy} - F_2\varphi_2}{\tau_{xz}^2 - \varphi_1\varphi_2}, \quad \psi_2' = \frac{F_2\tau_{xy} - F_1\varphi_1}{\tau_{xy}^2 - \varphi_1\varphi_2}. \qquad (2.6)$$

Equations (2.6) govern functions ψ_1 and ψ_2, with functions τ_{xy}, φ_1, and φ_2 determined from (2.1), (2.3), and (2.5).

3. We now consider the Mises plasticity condition:

$$(\sigma_x - \sigma_y)^2 + (\sigma_y - \sigma_z)^2 + (\sigma_z - \sigma_x)^2 + 6(\tau_{xy}^2 + \tau_{yz}^2 + \tau_{xz}^2) = 6k^2. \qquad (3.1)$$

From the associated plastic-flow rule, we have

$$\varepsilon_x = 6\lambda(\sigma_x - \sigma), \quad \varepsilon_{xy} = 6\lambda\tau_{xy},$$
$$\varepsilon_y = 6\lambda(\sigma_y - \sigma), \quad \varepsilon_{xz} = 6\lambda\tau_{xz},$$
$$\varepsilon_z = 6\lambda(\sigma_z - \sigma), \quad \varepsilon_{yz} = 6\lambda\tau_{yz}.$$

From these relations, it follows that relationship (1.5) and the equalities

$$\frac{\varepsilon_x}{\sigma_x - \sigma} = \frac{\varepsilon_y}{\sigma_y - \sigma} = \frac{\varepsilon_{xy}}{\tau_{xy}} = \frac{\varepsilon_{xz}}{\tau_{xz}} = \frac{\varepsilon_{yz}}{\tau_{yz}} \qquad (3.2)$$

are valid.

We seek the solution under the assumptions of (1.7)–(1.10). From (1.9), we have

$$\sigma_x - \sigma = \frac{1}{3}(2\varphi_1 - \varphi_2), \quad \sigma_y - \sigma = \frac{1}{3}(2\varphi_2 - \varphi_1),$$
$$\sigma_z - \sigma = -\frac{1}{3}(\varphi_1 + \varphi_2). \qquad (3.3)$$

Taking into account (3.1) and (3.3), we obtain

$$\tau_{xy}^2 = F^2(z) - \frac{1}{3}[\varphi_1^2 + \varphi_2^2 - \varphi_1\varphi_2], \qquad F^2(z) = k^2 - \tau_{xz}^2 - \tau_{yz}^2, \tag{3.4}$$

where τ_{xz} and τ_{yx} are determined by relations (1.8).

According to (1.12) and (3.3), Eqs. (3.2) take the form

$$\frac{3p_1}{2\varphi_1 - \varphi_2} = \frac{3q_2}{2\varphi_2 - \varphi_1} = \frac{q_1 + p_2}{2\tau_{xy}} = \frac{\psi_1'}{2\tau_{xz}} = \frac{\psi_2'}{2\tau_{yz}}. \tag{3.5}$$

From (3.5), we find

$$\varphi_2 = m\varphi_1, \quad m = \frac{2q_2 + p_1}{2p_1 + q_2}. \tag{3.6}$$

Using (3.4), (3.6), and the equality

$$\frac{3p_1}{2\varphi_1 - \varphi_2} = \frac{q_1 + p_2}{2\tau_{xy}},$$

we obtain the equations

$$\varphi_1 = MF(z),$$

$$M = \frac{\pm\sqrt{3}}{1 + m^2 - m + \frac{3}{4}\left(\frac{q_1 + p_2}{2p_1 + q_2}\right)^2}, \tag{3.7}$$

$$\varphi_2 = NF(z), \quad N = mM.$$

With regard to expressions (3.5)–(3.7), we arrive at the equation

$$\frac{3p_1}{(2N - M)F(z)} = \frac{\psi_1'}{2\tau_{xz}} = \frac{\psi_2'}{2\tau_{yz}}$$

and, finally,

$$\psi_1(z) = aLJ_1(z) + c_1LJ_2(z) + d_1,$$
$$\psi_2(z) = bLJ_1(z) + c_2LJ_2(z) + d_2,$$

$$d_1, d_2 = \text{const}, \quad L = \frac{6p_1}{2N - M},$$

$$J_1(z) = -\frac{1}{a^2 + b^2}F(z) - \frac{ac_1 + bc_2}{2\sqrt{a^2 + b^2}}J_2(z),$$

$$J_2(z) = \frac{1}{\sqrt{a^2 + b^2}}\arcsin\frac{\sqrt{a^2 + b^2}z + \frac{ac_1 + bc_2}{2\sqrt{a^2 + b^2}}}{k^2 + \frac{(ac_1 + bc_2)^2}{4(a^2 + b^2)} - c_1^2 - c_2^2}.$$

Thus, in accordance with (1.9) and (1.10), we have determined the stress components and the strain-rate components in the problem of three-dimensional flow of an ideally plastic layer compressed by rough plates.

REFERENCES

1. L. Prandtl, Z. Angew. Math. Mech. **3**, 401 (1923).
2. D. D. Ivlev, Izv. Akad. Nauk, Mekh. Tverd. Tela, No. 1, 5 (1998).
3. A. Yu. Ishlinskiĭ, Uch. Zap. Mosk. Gos. Univ., Mekh. **117**, 90 (1946).

Translated by V. Chechin

Doklady Physics, Vol. 46, No. 1, 2001, pp. 63–67. Translated from Doklady Akademii Nauk, Vol. 376, No. 3, 2001, pp. 338–342.

MECHANICS

R-Function Theory in Unsteady Problems of Elastic-Wave Diffraction

V. F. Kravchenko*, Corresponding Member of the RAS V. I. Pustovoĭt, V. L. Rvachev***, and N. D. Sizova*****

Received August 1, 2000

INTRODUCTION

The stressed-strained state of an elastic cavity weakened by a hole of nonclassic shape in the case when an acting load varies in time in an arbitrary manner is difficult to investigate, first of all, because of the impossibility of separating the time variable. In this connection, in order to solve unsteady problems, we often have to use integral transformations over the time variable, the execution of an inverse integral transformation being one of the points in this case.

FORMULATION OF THE PROBLEM

Many issues associated with studying elastic-wave diffraction reduce to solution of unsteady problems for potentials of longitudinal and transverse waves Φ and Ψ [1–4]:

$$\frac{\partial^2\Phi}{\partial x_1^2} + \frac{\partial^2\Phi}{\partial x_2^2} = \frac{\partial^2\Phi}{\partial t^2}, \quad \frac{\partial^2\Psi}{\partial x_1^2} + \frac{\partial^2\Psi}{\partial x_2^2} = \gamma^2\frac{\partial^2\Psi}{\partial t^2}. \qquad (1)$$

Here, $x = (x_1, x_2)$, $t = c_1 t_1$, $\gamma = \dfrac{c_1}{c_2}$, and c_1, c_2 are the propagation velocities for longitudinal and transverse waves. We assume that the boundary conditions caused by the action of a wave of arbitrary profile on an elastic medium weakened by a complex-shaped hole Ω with a boundary contour Γ are of the form

$$\sigma_n|_\Gamma = f_1(x_1, x_2, t), \quad \tau_n|_\Gamma = f_2(x_1, x_2, t), \qquad (2)$$

where n and τ are the normal and the tangent to the boundary contour Γ, respectively. The initial conditions are written as

$$\Phi|_{t=0} = 0, \quad \left.\frac{\partial\Phi}{\partial t}\right|_{t=0} = 0,$$
$$\Psi|_{t=0} = 0, \quad \left.\frac{\partial\Phi}{\partial t}\right|_{t=0} = 0. \qquad (3)$$

For solving problems of such type, methods of the dynamic elasticity theory are mainly employed [4]. However, they make it possible to obtain exact analytic solutions, as a rule, only for a limited number of problems.

METHOD OF SOLUTION

We will solve problem (1), (2) using approaches based on the combined employment of the Laplace transform [5] and the R-function method (RFM) [6–11]. The algorithm for application of the Laplace transform implies the following stages:

(a) A passage from the desired original $F(x_1, x_2, t)$ to the transform function $\bar{F}(p, x_1, x_2)$ is performed.

(b) In accordance with the operational-calculus theorems, the initial system of equations (1), (2) is transformed to a simpler system of equations in terms of the transform-function $\bar{F}(p, x_1, x_2)$.

(c) A solution to the transformed system in terms of the transform-function $\bar{F}(p, x_1, x_2)$ is found.

(d) A passage from the solution obtained for the transform-function $\bar{F}(p, x_1, x_2)$ to the original $F(x_1, x_2, t)$ is realized.

We apply the Laplace transform in t-variable to system (1)–(3):

$$\bar{F}(p, x_1, x_2) = \int_0^\infty F(x_1, x_2, t)e^{-pt}dt. \qquad (4)$$

Here, p is the transformation parameter, $\mathrm{Re}\,p > 0$; and the functions Φ and Ψ are implied by function $F(x_1, x_2, t)$. Then, in the transform domain, we obtain the system of

* *Institute of Radio Engineering and Electronics, Russian Academy of Sciences, ul. Mokhovaya 18, Moscow, 103907 Russia*

** *Central Design Bureau of Unique Instrumentation, Russian Academy of Sciences, ul. Butlerova 15, Moscow, 117342 Russia*

*** *Institute of Machine-Building Problems, National Academy of Sciences, Kharkov, Ukraine*

1028-3358/01/4601-0063$21.00

Helmholtz equations [2, 3] for the functions $\bar{\Phi}$ and $\bar{\Psi}$:

$$\frac{\partial^2\bar{\Phi}}{\partial x_1^2}+\frac{\partial^2\bar{\Phi}}{\partial x_2^2}=p^2\bar{\Phi},\quad \frac{\partial^2\bar{\Psi}}{\partial x_1^2}+\frac{\partial^2\bar{\Psi}}{\partial x_2^2}=\gamma^2p^2\bar{\Psi} \qquad (5)$$

with boundary conditions

$$\sigma_n\big|_\Gamma=\bar{f}_1(x_1,x_2,p),\quad \tau_n\big|_\Gamma=\bar{f}_2(x_1,x_2,p). \qquad (6)$$

We solve problem (5), (6) by employing approaches based on the R-function theory [6–11]. We represent the analytic solutions for the potentials $\bar{\Phi}$ and $\bar{\Psi}$ as [7]

$$\begin{aligned}\bar{\Phi}&=\frac{\partial}{\partial x_1}[\Phi_1+\Psi_2]-\frac{\partial}{\partial x_2}[\Phi_2+\Psi_1]+\Phi_0,\\ \bar{\Psi}&=\frac{\partial}{\partial x_2}[\Phi_1-\Psi_2]-\frac{\partial}{\partial x_1}[\Phi_2-\Psi_1]+\Psi_0,\end{aligned} \qquad (7)$$

where

$$\Phi_1=\Phi_{i1}+\omega D_1\Phi_{i1}+\omega T_1\Phi_{i1}\frac{\partial\omega}{\partial x_1}\frac{\partial\omega}{\partial x_2}\frac{2(\lambda+\mu)}{\lambda+2\mu},$$

$$\Psi_i=\omega T_1\Phi_{i1}\left[\frac{\lambda}{\lambda+2\mu}\left[\frac{\partial\omega}{\partial x_1}\right]^2+\left[\frac{\partial\omega}{\partial x_2}\right]^2\right],\quad i=1,2;$$

$$\Phi_0=\frac{\partial}{\partial x_1}\tilde{\Phi}_0+\frac{\partial}{\partial x_2}\tilde{\Psi}_0,\quad \Psi_0=\frac{\partial}{\partial x_2}\tilde{\Phi}_0-\frac{\partial}{\partial x_1}\tilde{\Psi}_0,$$

$$\tilde{\Phi}_0=\frac{1}{\lambda+\mu}\omega\frac{\partial\omega}{\partial x_1}\bar{f}_1(x)+\frac{1}{\mu}\omega\frac{\partial\omega}{\partial x_2}\bar{f}_2(x),$$

$$\tilde{\Psi}_0=\frac{1}{\lambda+\mu}\omega\frac{\partial\omega}{\partial x_2}\bar{f}_1(x)-\frac{1}{\mu}\omega\frac{\partial\omega}{\partial x_1}\bar{f}_2(x).$$

Here, $\omega=\omega(x)$ are functions describing the equation of the boundary Γ; T_1, D_1 are special differential operators defined in [6]; Φ_{i1} are special functions, classic polynomials, or polynomials with local supports, which can be represented as expansions with coefficients determined from the variation principle corresponding to problem (5), (6); and λ, μ are the Lamé coefficients for the elastic medium. Solutions (7) have the form of functional relations involving elementary functions or superposition of elementary and special functions. In this case, boundary conditions (2) and the geometry of the domain under investigation for problem (1), (2) are taken into account analytically. Moreover, the arbitrariness in choosing functions Φ_{i1} ($i=1, 2$) makes it possible to take into consideration information available *a priori* (if it exists) on the exact solutions and to approach them in the metric of corresponding functional space. The conditions at infinity are taken into account by introducing the pseudodifferential operators

$$S_1(\Phi)=\frac{\partial\Phi}{\partial n},\quad S_2(\Psi)=\frac{\partial\Psi}{\partial n}.$$

These operators are considered in a certain bounded domain $\Omega_0\in\Omega$ with a boundary Γ_0. We choose the function $\omega(x)$ in the form

$$\omega=\frac{\omega_0 r}{\omega_0+r},\quad r=(x_1^2+x_2^2)^{1/2},$$

where ω_0 is the equation for boundary Γ_0 in domain Ω_0. We provide a required quality for structural formula (7) when studying wave processes in various zones for incident and reflected waves. To find the potentials Φ and Ψ of initial problem (1), (2), the inverse Laplace transform L^{-1} needs to be performed [5]. This stage is the most difficult in the application of the Laplace transform. Various approaches for finding an original exist, e.g., tables of correspondence between originals and their transforms. However, the tables do not always cover the cases relevant to actual practice. Moreover, an original function is often expressed in terms of sophisticated functions which are difficult to calculate [5]. We demonstrate one of the approaches for approximate inversion of the Laplace transform. It allows the original to be found from its transform in the real axis [12] and reduces to summation of convergent infinite series. In particular, this method for the inversion of the Laplace transform allows the original $F(x_1, x_2, t)$ to be found using the Mellin–Bromwich inversion formula [5]:

$$F(x_1,x_2,t)=e^{\gamma t}F^*(x_1,x_2,t), \qquad (8)$$

where

$$F^*(x_1,x_2,t)=\frac{1}{2\pi i}\int_{c-i\infty}^{c+i\infty}\bar{F}^*(p,x_1,x_2)e^{pt}dp;$$

$\bar{F}^*(p, x_1, x_2)=\tilde{F}(p+\gamma)$ is the function regular in the region $\mathrm{Re}\,p>0$; c is the abscissa in the absolute-convergence half-plane for the Laplace integral; p is the parameter of the Laplace transform ($\mathrm{Re}\,p>\gamma$); and γ is the abscissa of the absolute convergence for the Laplace transform, which is not necessarily zero. The algorithm for this method of employing the inverse Laplace transform [12, 13] implies that the exponent in formula (8) can be approximated by the expression

$$e^x\approx e_a^x=\frac{1}{2}\left(\frac{\varphi_1(x,a)}{\sinh(x-a)}+\frac{\varphi_2(x,a)}{\cosh(x-a)}\right), \qquad (9)$$

where a is an arbitrary positive number; the functions $\varphi_1(x, a)$ and $\varphi_2(x, a)$ are chosen in such a manner that the condition $\lim\limits_{a\to\infty}e_a^x=e^x$ is fulfilled.

With the expansion of functions $\sinh x$ and $\cosh x$ in terms of partial fractions and assuming that $\varphi_1(p, a)\tilde{F}^*\longrightarrow 0$, $\varphi_2(p, a)\tilde{F}^*(p)\longrightarrow 0$ as $|p|\longrightarrow\infty$,

the following expression can be written out:

$$F^*(t, a) = \frac{1}{2t}\left\{\varphi_1(a, a)\tilde{F}^*\left(\frac{a}{t}\right) + S_1(\varphi_1) + S_2(\varphi_2)\right\}. \quad (10)$$

Here, expression (8), with substitution (9) taken into account, is implied as $F^*(t, a)$:

$$S_1(\varphi_1) = \sum_{n=1}^{\infty}(-1)^n\left\{\varphi_1(a + n\pi i, a) \times\left(\tilde{F}^*\left[\frac{1}{t}(a + n\pi i)\right] + \tilde{F}^*\left[\frac{1}{t}(a - n\pi i)\right]\right)\right\},$$

$$S_2(\varphi_2) = \sum_{n=1}^{\infty}(-1)^n\left\{\varphi_2\left(a - \left(n - \frac{1}{2}\right)\pi i, a\right) \times\tilde{F}^*\left[\frac{1}{t}\left(a - \left(n - \frac{1}{2}\right)\pi i\right)\right] + \varphi_2\left(a + \left(n - \frac{1}{2}\right)\pi i, a\right)\tilde{F}\left[\frac{1}{t}\left(a + \left(n - \frac{1}{2}\right)\pi i\right)\right]\right\}.$$

Substituting expression (10) into (8), we obtain the inverse Laplace transform in the form of a series:

$$F(x_1, x_2, t) = e^{\gamma t}F^*(x_1, x_2, t, a) = \frac{1}{2t}e^{\gamma t}\left\{\varphi_1(a, a)\tilde{F}^*\left(\frac{a}{t}\right) + S_1(\varphi_1) + S_2(\varphi_2)\right\}. \quad (11)$$

Relation (11) is simplified provided that functions $\varphi_1(x, a)$ and $\varphi_2(x, a)$ are independent of x or that they can be approximated, e.g., by the following functions:

$$\varphi_1(x, a) = \sinh a, \quad \varphi_2(x, a) = \cosh a. \quad (12)$$

In the latter case, we have

$$F^*(t, a) = \frac{1}{2a}\left\{\sinh a\left[R_0 + 2\sum_{n=1}^{\infty}R_n\right] + 2\cosh a\sum_{n=1}^{\infty}I_n\right\}, \quad (13)$$

where

$$R_n = (-1)^n\mathrm{Re}\tilde{F}^*\left(\frac{a}{t} + i\frac{\pi}{t}n\right),$$

$$I_n = (-1)^n\mathrm{Im}\tilde{F}^*\left(\frac{a}{t} + i\frac{\pi}{t}\left(n - \frac{1}{2}\right)\right).$$

In our case, $\tilde{F}^*$ implies the potentials of the longitudinal and transverse waves $\bar{\Phi}$ and $\bar{\Psi}$ considered as transform functions for which the solution is represented in form (7). If approximation (12) is fulfilled, we can apply inverse integral transformation (8) to solutions (7) and arrive at the expressions for the potentials of longitudinal and transverse waves Φ and Ψ in the form of the following series:

$$\Phi = \frac{1}{2a}\left\{\frac{\partial}{\partial x_1}[\Phi_1 + \Psi_2] - \frac{\partial}{\partial x_2}[\Phi_2 + \Psi_1] + \Phi_0\right\} \times\left\{\sinh a\left[R_0 + 2\sum_{n=1}^{\infty}R_n\right] + 2\cosh a\sum_{n=1}^{\infty}I_n\right\},$$

$$\Psi = \frac{1}{2a}\left\{\frac{\partial}{\partial x_2}[\Phi_1 - \Psi_2] - \frac{\partial}{\partial x_1}[\Phi_2 - \Psi_1] + \Psi_0\right\} \times\left\{\sinh a\left[R_0 + 2\sum_{n=1}^{\infty}R_n\right] + 2\cosh a\sum_{n=1}^{\infty}I_n\right\}. \quad (14)$$

The parameter a is chosen in such a manner that the upper and lower limits containing the desired original could be indicated. It is also easy to write out the general expression for potentials Φ and Ψ with general relation (11) taken into account. Thus, with known solution (7) in the transform domain and the values of these functions at points $\left(\frac{a}{t} + i\frac{\pi}{t}n\right), \left(\frac{a}{t} + i\frac{\pi}{t}\left(n - \frac{1}{2}\right)\right)$ of the real axis, the solution to problem (1), (2) can be found and analyzed. Using the formulas obtained for potentials Φ and Ψ, the components of the strain- and stress tensors can be determined from the following expressions [1]:

$$2\varepsilon = \nabla\mathbf{U} + (\nabla\mathbf{U})^*, \quad \sigma = \lambda\varepsilon E + 2\mu\varepsilon.$$

Here, the asterisk implies transposition; E is the unit matrix; c_1 is the propagation velocity for longitudinal waves; c_2 is the propagation velocity for transverse waves; and $\mathbf{U}$ is the displacement vector that can be represented in the form

$$\mathbf{U} = \mathbf{U}_\mathrm{p} + \mathbf{U}_\mathrm{s}.$$

Here, vectors $\mathbf{U}_\mathrm{p}$ and $\mathbf{U}_\mathrm{s}$ describe, respectively, the potential field and solenoidal field:

$$\mathbf{U}_\mathrm{p} = \nabla\Phi, \quad \mathbf{U} = \nabla\Psi, \quad \nabla\Psi = 0.$$

NUMERICAL RESULTS

We consider the interaction of a plane unsteady dilatational wave with a circular cylindrical cavity of radius r_1 having a circular groove of radius r_2. The interaction occurs in an unbounded elastic medium under the con-

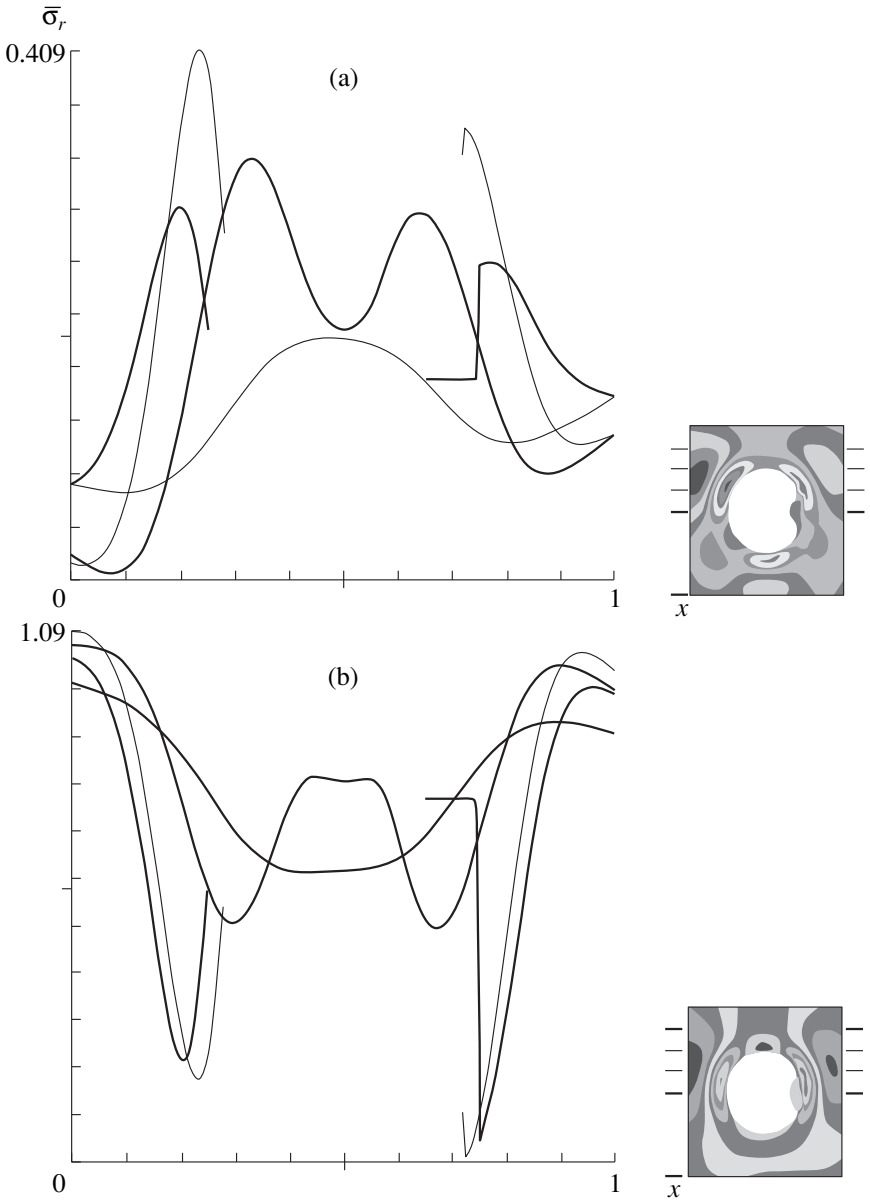

Fig. 1. Diagram for stresses $\bar{\sigma}_r$ in an elastic medium in the vicinity of a region weakened by a hole for the case of (a) $t = 2$ and (b) 4 (short waves).

ditions of plane deformation. At the cavity surface, the following boundary conditions hold true:

$$\sigma_n|_\Gamma = f(t, x_1, x_2), \quad \tau|_\Gamma = 0. \tag{15}$$

Here, Γ is the cavity boundary, $f(t, x_1, x_2) = \sigma_0\sigma(t)$, and $\sigma_0 = \text{const}$. We consider the results of calculations carried out according to the foregoing algorithm. In Fig. 1, the stress distribution $\bar{\sigma}_r = \dfrac{\sigma_r}{\sigma_0}$ is shown in the vicinity of the cavity for dimensionless time moments $\left(t = \dfrac{c_1\tau}{r_1} = 2, 4\right)$. The value of a in relations (14) was determined from the intervals (0.713, 0.789) and (1.111, 1.156) for the short and long waves, respectively. It is worth noting that the solution to this problem in the limiting case of the cylindrical cavity without a groove ($r_2 = 0$) has demonstrated reasonable agreement with the results of paper [1].

Thus, in the present study, the method for solving boundary value problems of unsteady elastic-wave diffraction on complex-shaped objects, based on the R-function theory, is proposed and substantiated. The algorithms found, as well as the physical analysis of the results obtained and their comparison with traditional methods, allow it to be concluded that the method proposed is quite highly efficient.

The results of this study were reported at the Second International Conference on Modern Trends in Computational Physics, July 24–29, 2000. Dubna, Russia [14].

REFERENCES

1. A. N. Gruz', V. D. Kubenko, and M. A. Cherevko, *Diffraction of Elastic Waves* (Naukova Dumka, Kiev, 1978).
2. M. Sh. Israilov, *Dynamic Theory of Elasticity and Diffraction of Waves* (Mosk. Gos. Univ., Moscow, 1992).
3. I. G. Filippov and O. A. Egorychev, *Unsteady Oscillations and Diffraction of Waves in Acoustic and Elastic Media* (Mashinostroenie, Moscow, 1977).
4. V. B. Poruchikov, *Methods of Dynamic Theory of Elasticity* (Nauka, Moscow, 1986).
5. V. A. Ditkin and A. P. Prudnikov, *Integral Transforms and Operational Calculus* (Nauka, Moscow, 1974, 2nd ed.; Pergamon, Oxford, 1966).
6. V. L. Rvachev, *Theory of R-Functions and Its Certain Applications* (Naukova Dumka, Kiev, 1982).
7. Yu. V. Gulyaev, V. F. Kravchenko, V. L. Rvachev, and N. D. Sizova, Dokl. Akad. Nauk **343**, 163 (1995).
8. Yu. V. Gulyaev, V. F. Kravchenko, V. L. Rvachev, and N. D. Sizova, Dokl. Akad. Nauk **344**, 315 (1995).
9. Yu. V. Gulyaev, V. F. Kravchenko, V. L. Rvachev, and N. D. Sizova, Dokl. Akad. Nauk **344**, 457 (1995).
10. Yu. V. Gulyaev, V. F. Kravchenko, V. L. Rvachev, and N. D. Sizova, Dokl. Akad. Nauk **346**, 455 (1996).
11. V. F. Kravchenko, V. I. Pustovoĭt, V. L. Rvachev, and N. D. Sizova, Dokl. Akad. Nauk **372**, 487 (2000) [Dokl. Phys. **45**, 288 (2000)].
12. T. Hosono, Radio Sci. **16**, 1015 (1981).
13. G. S. Kit and O. V. Poberezhnyĭ, *Unsteady Processes in Solids with Crack-Type Defects* (Naukova Dumka, Kiev, 1992).
14. N. D. Sizova, in *2nd Int. Conf. on Modern Trends in Computational Physics, July 24–29, 2000* (Dubna, Russia). Book of Abstracts, p. 153.

Translated by V. Tsarev

Doklady Physics, Vol. 46, No. 1, 2001, pp. 9–11. Translated from Doklady Akademii Nauk, Vol. 376, No. 2, 2001, pp. 183–185.

PHYSICS

Generation of Strong Fields in Plasma

A. G. Oreshko

Presented by Academician Yu.A. Ryzhov February 25, 2000

Received April 21, 2000

Available experimental data testify to the existence of regimes in plasmas in which strong electric and magnetic self-fields can appear. According to the Gauss theorem, electric-field intensity is determined by the space charge. As a result of charge separation in plasma, electric domains are formed [1]. These domains and the domain instability observed in semiconductor plasma were also detected afterwards in gas-discharge plasma [2], in explosive-emission cathode plasma [3], and in extraterrestrial-space plasma. Collapsing the domains near plasma-chamber walls results in formation of plasma channels [3]. These channels were also observed in [4].

We consider the grounds leading to the formation of domains in plasma. Voltage drop is determined by finite plasma conductivity. In a number of cases, the output voltage of a power source maintains an electric-field intensity $\mathbf{E}$ in plasma exceeding the critical Dreicer field $\mathbf{E}_c$. At $\mathbf{E} > \mathbf{E}_c$, there occurs a transition of electrons into the collisionless runaway state. At a certain field intensity, their directed velocity exceeds the thermal velocity. In the presence of a magnetic field, at $\mathbf{E} > \mathbf{B}$, plasma particles are also captured into the acceleration regime. In inhomogeneous plasmas, there exist concentration (pressure) gradients. The action of electric and magnetic fields and concentration gradients results in the formation of directed-drift flows of electrons and ions. In general form, these flows can be written out as the relations

$$\mathbf{\Gamma}_e = -n_e\mathbf{u}_e(\mathbf{E}, \mathbf{B}) - D_e\nabla n_e, \quad (1)$$

$$\mathbf{\Gamma}_i = n_i\mathbf{u}_i(\mathbf{E}, \mathbf{B}) - D_i\nabla n_i, \quad (2)$$

where n is the concentration, $\mathbf{u}$ is the velocity, and D is diffusivity. The subscripts e and i denote an electron and an ion, respectively. In the region of charge separation, the condition of inequality for flows of directed particle drift takes place, i.e., $\mathbf{\Gamma}_e \neq \mathbf{\Gamma}_i$. In a strong longitudinal electrical field, $\mathbf{\Gamma}_e > \mathbf{\Gamma}_i$. In plasmas placed into a longitudinal magnetic field, the transverse flows of the directed drift are determined by the particle diffusion. In a weak magnetic field, when the cyclotron frequency ω_c is much lower than the collision frequency between electrons and neutral atoms ν_m, the transverse flows satisfy the inequality $\mathbf{\Gamma}_{e,\perp} > \mathbf{\Gamma}_{i,\perp}$. Conversely, in a strong magnetic field, i.e., when $\omega_c \gg \nu_m$, the reverse inequality, $\mathbf{\Gamma}_{e,\perp} < \mathbf{\Gamma}_{i,\perp}$, is valid. Ignoring the processes of ionization, recombination, and collisions, we can write out continuity equations for ions and electrons in the form

$$\frac{\partial n_e}{\partial t} = -\nabla \cdot \mathbf{\Gamma}_e, \quad (3)$$

$$\frac{\partial n_i}{\partial t} = -\nabla \cdot \mathbf{\Gamma}_i. \quad (4)$$

The distribution of the electric-field intensity in plasmas with a dielectric permittivity ε is given by the Poisson equation

$$\nabla \cdot (\varepsilon\mathbf{E}) = 4\pi e(n_i - n_e). \quad (5)$$

The electron and ion densities standing in the right-hand side of equation (5) are excessive. Upon differentiating (5) with respect to time and taking into account (3) and (4), we obtain

$$\frac{\partial \mathbf{E}_{\text{ind}}}{\partial t} = \left(\frac{4\pi e}{\varepsilon}\right)(\mathbf{\Gamma}_e - \mathbf{\Gamma}_i). \quad (6)$$

It follows from (6) that the intensity $\mathbf{E}_{\text{ind}}$ of the electric-field induced in the process of charge separation is proportional to the difference in the directed drift flows for electrons and ions. Since plasma is an element of an electric circuit (its load), then the density fluctuations for particles of a certain kind, arising in the region of domain nucleation, have no time to disappear because of the finite plasma conductivity. Therefore, the density fluctuation will grow until the resulting force of all the forces responsible for the fluctuation and leading to charge separation will be balanced by the force of the Coulomb attraction between the oppositely charged layers of the domain. At this moment, a stable electric domain of a strong field is formed in the plasma. The generation of the domain occurs for a time t_f exceeding the Maxwellian relaxation time τ_M for the space charge. In semiconductor physics, it is assumed that $t_f = 3\tau_M$.

Moscow State Institute of Aviation,
Volokolamskoe sh. 4, Moscow, 125080 Russia

1028-3358/01/4601-0009$21.00

The relaxation time is given by the relationship $\tau_M = \frac{\varepsilon}{4\pi e n_e \mu_e}$ [5], where μ_e is the electron mobility.

The formation of electric domains in plasma is equivalent to introducing an element with a capacitive component into a medium having an ohmic component of its impedance. Using the Ohm's law $\mathbf{j} = \sigma\mathbf{E}$ and the relations $I = \frac{dQ}{dt}$ and $Q = CU$, we can determine that the charge in a domain layer varies as $Q = Q_0 \exp\left(\frac{t}{\tau_M}\right)$. The displacement or escape of a group of charged particles of the first kind with a larger velocity from a certain region in the plasma to the distance L exceeding the Debye screening length λ_D and their separation from a group of particles of the second kind give rise to both an induced electric field $\mathbf{E}_{ind}$ and a space charge associated with this field. In the process of formation or decomposition of a domain, a displacement current appears between its layers. Since the electric circuit must be closed, it is evident that the role of the conductor or reverse-current conductor connecting the domain layers is played by the plasma contacting them through the periphery. The transition of a part of plasma electrons from the current-conducting (free) state into the bound state, i.e., into the layers of the excess negative charge of electrical domains, is responsible for the anomalous plasma resistance.

The current flowing between the layers of a domain during its generation or collapse is related to change in the electric charge. In accordance with the Maxwell theory, the time-alternating electric field produces the magnetic field. The left-hand side of Eq. (6), containing the factor $\frac{1}{c}$, corresponds to the displacement-current density entering into the Maxwell equation:

$$\nabla \times \mathbf{B} = \frac{1}{c}\frac{\partial \mathbf{E}}{\partial t} + \frac{4\pi}{c}\mathbf{J}. \quad (7)$$

In the process of formation, the conduction current in the region of a domain drops to zero. We now estimate the electric-field intensity using the data obtained in [3]. The peak voltage across a domain was U_{dl} = 50 kV. The distance between layers can be evaluated with the help of the formula $L = u_e t_f$. In a strong field, at $\mathbf{E} > \mathbf{E}_c$, the velocity of the electron motion is $u_e \approx 10^8$ cm/s. For plasma with $n_e = 10^{14}$ cm^{-3}, the domain time formation attains $t_f = 3 \times 10^{-10}$ s. Hence, we have $L = 3 \times 10^{-2}$ cm. The field intensity $E_{ind} = \frac{U_{dl}}{L}$ induced on a domain is $E_{ind} \approx 1.7 \times 10^6$ V/cm. The variation rate for the field intensity induced on a domain is $\frac{dE_{ind}}{dt} \approx 10^{15}$ V/(cm s). The estimates based on the data obtained in [3] show that, when the electric current in the region of a domain attains I = 200 A, the magnetic induction at a distance of 0.1 cm from the domain center is 4 kGs. The magnetic fields induced in the process of charge separation are responsible for the formation of magnetic cavities, i.e., regions in which the resulting magnetic field in both its magnitude and direction considerably differs from the induction of the longitudinal magnetic field imposed on the plasma. These cavities promote anomalous plasma diffusion. The spontaneous magnetic fields arising in plasma of a Z-pinch, which is caused by the explosion of wires, exist owing to electric domains. Formations propagating with a velocity characteristic of domains were detected in such plasma [6].

When forming a domain, the velocity of a group of particles escaping a volume element decreases because of the Coulomb interaction between the domain layers. The reduction in the kinetic energy for this group of particles is accompanied by a rise in their potential energy on the domain. The charge separation in plasma, which occurs for a very short time, is accompanied by the appearance of transverse electromagnetic waves. The equations of motion for particles in the presence of a strong electric field in weakly ionized plasmas can be written out in the form

$$m_e\left(\frac{\partial}{\partial t} + \mathbf{u}_e \cdot \nabla\right)\mathbf{u}_e = -e\mathbf{E} - m_e \nu_{ea}(\mathbf{E})\mathbf{u}_e, \quad (8)$$

$$m_i\left(\frac{\partial}{\partial t} + \mathbf{u}_i \cdot \nabla\right)\mathbf{u}_i = e\mathbf{E}. \quad (9)$$

Since the directed-drift velocity of electrons in the strong electric field is commensurable with the thermal velocity or even higher, we can write out the energy-dependent collision frequency in the form $\nu_{ea}(\mathbf{E}) = \frac{e}{m_e}\mu_d^{-1}$. Solution of a system consisting of equations of motion, a continuity equation and Maxwell equations makes it possible to obtain expressions for the frequency of space-charge waves,

$$\omega_{wsc} = \omega_{pe} - \frac{\omega_{pe}^2}{24\pi i \sigma_d}, \quad (10)$$

and the frequency of transverse electromagnetic waves,

$$\omega_{shf} = kc + \omega_{wsc}, \quad (11)$$

generated in the process of charge separation. The following notation is used in (10) and (11): ω_{pe} is the plasma (Langmuir) electron frequency, σ_d is the differential plasma conductivity ($\sigma_d = 4\pi e n_e \mu_d$), k is the wave vector, and c is the speed of light. It follows from (10) that the charge separation time $\tau = \omega_{wsc}^{-1}$ and the constants for the rise (decay) time of fluctuation amplitudes are determined by the differential plasma conductivity. Charged particles existing inside a domain and

electrons and ions produced due to ionization of the neutral atoms in the domain region accumulate the energy corresponding to the voltage on the domain. This energy is sufficient to satisfy the phase-matching condition and subsequent acceleration with the help of electromagnetic waves generated in the process of charge separation. The energy of fast electrons and ions in a number of experiments exceeds by several times the value corresponding to the voltage applied. The high voltages in plasmas are attained due to interaction of the generated electromagnetic waves with both plasma and the plasma-containing chamber. In a number of cases, the latter plays the role of a hollow resonator. Application of a resonator insulated from electrodes in spark-discharge experiments results in a significant decrease in the breakdown voltage [7].

It is also evident that the magnetic storms in the Sun's chromosphere and fast particle flows detected in periods of elevated solar activity are caused by the generation of domains in the solar plasma.

REFERENCES

1. J. B. Gunn, Solid State Commun. **1**, 88 (1963).
2. G. D. Myl'nikov and A. P. Napartovich, Fiz. Plazmy **1**, 892 (1975) [Sov. J. Plasma Phys. **1**, 486 (1975)].
3. A. G. Oreshko, Fiz. Plazmy **17**, 679 (1991) [Sov. J. Plasma Phys. **17**, 398 (1991)].
4. V. D. Korolev, V. P. Smirnov, M. V. Tulupov, *et al.*, Dokl. Akad. Nauk SSSR **270**, 1109 (1983) [Sov. Phys.–Dokl. **28**, 488 (1983)].
5. M. E. Levinshteĭn, Yu. K. Pozhela, and M. S. Shur, *Gunn Effect* (Sov. Radio, Moscow, 1975).
6. V. I. Afonin and V. M. Murugov, Fiz. Plazmy **24**, 363 (1998) [Plasma Phys. Rep. **24**, 332 (1998)].
7. A. G. Oreshko, in *Proc. I Int. Congr. on Radiation Physics, High-Current Electronics and Modification of Materials. Tomsk, Sept. 24–29, 2000* (Tomsk, 2000), vol. 1, pp. 358–360.

Translated by Yu. Vishnyakov